

UNIVERSITY OF CALIFORNIA  
RIVERSIDE

PROBING THE SPIN STRUCTURE OF THE PROTON USING POLARIZED  
PROTON-PROTON COLLISIONS AND THE PRODUCTION OF W-BOSONS

A Dissertation submitted in partial satisfaction  
of the requirements for the degree of

Doctor of Philosophy

in

Physics

by

Michael J. Beaumier

August 2016

Dissertation Committee:

Professor Kenneth Barish , Chairperson  
Professor Rich Seto  
Professor John Ellison

Copyright by  
Michael J. Beaumier  
2016

The Dissertation of Michael J. Beaumier is approved:

---

---

---

Committee Chairperson

University of California, Riverside

## Acknowledgments

Advisors and Mentors are some of the most important people any scientist will encounter in their professional career. Time and again, I have heard colleagues speak of "that one inspirational" person that drove them to be their best, and knew how to "grow" a researcher.

I am very greatful to my advisor, Ken Barish, whose calm, stoic and unabated support helped guide me through my research. Ken involved me in many aspects of the research group at UCR, beyond the scientific work. He insured that I was exposed to all aspects of research in particle physics, including writing grants, reviewing literature, mentoring younger students, building detectors, running a particle accelelrator detector, and of course, data analysis. Ken has always had the uncanny ability to know "who to talk to" for nearly any problem I might have. Ken connected me with other excellent physicists, who helped me grow as a researcher, and he gave me the freedom I needed to pursue my interests, and move in the scientific directions I felt most fruitful, while helping to provide an overall direction for my academic career and research.

Beyond all this, the single most important thing Ken has done for me, is to give me a second chance in graduate school. When he accepted me into his group, I was an undoubtedly risky choice. I struggled mightily my first year in grad school. I earned poor grades, and even had to re-take a class. In fact, my performance was so poor, that my teaching responsibilities were reduced, and eventually, I lost my graduate division fellowship, which ultimately meant that I had no income, or means of supporting myself; I was effectively dismissed from graduate school. However, I was interested in the research carried out by Ken and Rich Seto's heavy ion group, so I talked to Ken, who graciously accepted me into the group, provided me with academic and financial support, and even flew me out to Brookhaven National Lab my first summer of graduate school. I finally got to dive into 'real' physics research. I think it was this vote of confidence from Ken, as well as the awesome physics happening at the PHENIX experiment which gave me the confidence to wholeheartedly devote myself to my studies and research. Without Ken's vote of confidence, I fear that my graduate career would have been over in short order.

While at Brookhaven National Lab, I encountered graduate students, post docs, research staff, and other amazing physicists who taught me an incredible amount, and showed both patience, kindness, friendship and mentorship to me. Richard Hollis was one of the first people I encountered in my research group at UCR - I have never met a more

patient person. Richard helped me get my bearings, and set me straight, during my early (and later) years of graduate school. Oleg Eyser was with our group at that time as well - although I recall that he was less than thrilled to have yet another green graduate student constantly asking questions, taking time away from his work. He still made time to teach me, and introduced me to the very complicated PHENIX software system. Oleg challenged me, and expected me to find answers for myself, and was unrelenting in that regard, which I am certain made me a better researcher.

Josh Perry gave me a crash course on the PHENIX data acquisition system, boiling down this incredibly complicated system into understandable pieces, and helped me learn that ultimately, persistence pays off when tackling difficult problems. Martin Leitgab took me under his wing while I worked days and nights to learn PHENIX's fast data production systems. Martin's systematic, calm, and patient approach to problem solving has been something I have tried to emulate since my work with him - I could not have asked for a better mentor for that project. On that same project was my first introduction to Chris Pinkenburg and Martin Purschke - somewhat of the yin and yang of the PHENIX online data acquisition. I benefited enormously from conversations with both about PHENIX software, and online systems. Martin Purschke's kindness and sense of humor always spurred me on, while Chris' dogged dedication to doing things 'the right way' kept me honest. I have returned to Martin with various questions many times over the years, and he has always been cheerful, supportive and wise with his answers. Probably nobody other than Ed Desmond has been woken up so many times with emergencies at the PHENIX counting house in the middle of the night, yet even when I woke him at 3 am on many occasions, would simply state, in an exceptionally dry, well practiced line: 'Martin Speaking, please state the nature of your emergency'. I don't know of many who can manage to be coy and good natured under such circumstances.

I have to acknowledge Joe Seele as well, in this regard, as he probably more than anyone else, set me on the path to learning to program well, and using a computer effectively - these skills, so often neglected in Particle Physics, have paid off for me, many, many times over.

#### W Analysis Crew

Ralf Seidl, Francesca Giordano, Sangwha Park, Daniel Jumper, Abraham Meles, Chong Kim,

#### Friends and Family

DRAFT

---

DRAFT

DRAFT

Bob Beaumier, Marian Beaumier, Joe Beaumier, David Beaumier, Emily Vance, Jackie Hubbard, Alexander Anderson-Natalie, Corey Kownacki, Chris Heidt, Pat Odenthal, Behnam Darvish Sarvestani, Oleg Martynov,

Some say that it takes a village to raise a child. The same can be said of raising a graduate student up to earning a PhD. This thesis is dedicated to the multitude who have helped me become the man I am today, and to students who struggle, and their mentors who do not give up on them.

## ABSTRACT OF THE DISSERTATION

### PROBING THE SPIN STRUCTURE OF THE PROTON USING POLARIZED PROTON-PROTON COLLISIONS AND THE PRODUCTION OF W-BOSONS

by

Michael J. Beaumier

Doctor of Philosophy, Graduate Program in Physics  
University of California, Riverside, August 2016  
Professor Kenneth Barish , Chairperson

This thesis discusses the process of extracting information about the spin structure of protons, specifically, spin contributions from the sea of quarks and anti-quarks, which are kinematically distinct from the 'valence quarks'. We have known since the 'proton-spin crisis' [1] of the late 1980s that proton spin does not entirely reside in the valence quarks, so the thrust of experimental efforts since then have been designed to determine both how to probe the proton spin structure, and how to validate models for proton spin structure. Here, I discuss one particular approach to understanding the sea-quark spin contribution, which utilizes the production of real  $W$ -bosons, and the  $W$  coupling with polarized spin structure in the proton sea, as produced from polarized proton-proton collisions. Only one of the colliding protons is longitudinally spin polarized, in this analysis, and they are collided at an energy of  $500GeV$ . The experimental observable used is referred to as " $A_L$ " which is expressed mathematically as a ratio of sums and differences of various helicity combinations of singly polarized interactions between two protons, i.e.  $p + p^\Rightarrow \rightarrow W \rightarrow \mu + \nu$ . Once  $A_L$  has been experimentally measured, it can then be used to determine appropriate polarizations of proton sea-quarks, within a given uncertainty, if we write the cross-sections used in the calculation of  $A_L$  in terms of polarized parton distribution functions. Finally, this thesis will also include a discussion of my work experimentally determining the absolute luminosity of collisions at RHIC, which is needed as a normalization on any cross section used in the analysis. In particular, studying the cross section of the  $W$  interaction can help to validate our models for assigning a signal-to-background ratio to the  $W \rightarrow \mu$  events.



# Contents

<b>List of Figures</b>	<b>xiii</b>
<b>List of Tables</b>	<b>xxii</b>
<b>1 Introduction</b>	<b>1</b>
1.1 A Brief History of the Proton . . . . .	1
1.2 Scope and Objectives of This Work . . . . .	2
<b>2 Historic Perspective on the Structure of Matter and Spin</b>	<b>4</b>
2.1 The Phenomena of Spin . . . . .	4
2.2 A Brief History of Relevant Physics . . . . .	6
2.2.1 Ancient Foundations . . . . .	6
2.2.2 The Scientific Revolution . . . . .	8
2.2.3 Atomic Theory . . . . .	10
2.2.4 Early Quantum Theory . . . . .	14
2.2.5 Early Particle Physics and The Eightfold Way . . . . .	17
2.2.6 Deep Inelastic Scattering and The Parton Model . . . . .	21
2.3 World Experiments in Deep Inelastic Scattering . . . . .	26
2.3.1 CERN - European Muon Collaboration: 1979-1997 . . . . .	26
2.3.2 SLAC - E142: 1993-1994 . . . . .	27
2.3.3 SLAC - E143: 1992-1999 . . . . .	27
2.3.4 DESY - ZEUS: 1992-Present . . . . .	28
2.3.5 CERN - Spin Muon Collaboration: 1993-1998 . . . . .	28
2.3.6 SLAC - E154: 1994-1997 . . . . .	28
2.3.7 DESY - HERMES: 1995-2007 . . . . .	28
2.3.8 SLAC - E155: 1997-2003 . . . . .	28
2.3.9 CERN - COMPASS: 2005-Present . . . . .	28
2.3.10 DESY - H1: 1992-Present . . . . .	28
<b>3 Models and Associated Probes For Proton Spin Structure</b>	<b>29</b>
3.1 Modeling the Proton Structure . . . . .	29
3.2 Structure Functions . . . . .	30
3.2.1 Parton Distribution Functions . . . . .	30
3.2.2 Polarized Parton Distribution Functions . . . . .	30

3.2.3	Proton Spin Decomposition with the Ellis-Jeffe Sum Rule . . . . .	30
3.2.4	The Spin Asymmetry: An Experimental Probe . . . . .	31
3.3	that sweet table from Delia hasch . . . . .	31
3.4	Experimental Probes for Proton Spin Structure . . . . .	31
3.4.1	Physics Probes for the Proton Spin . . . . .	31
3.4.2	W Production . . . . .	31
3.5	Cross Sections and Luminosity . . . . .	36
<b>4</b>	<b>The Relativistic Heavy Ion Collider</b>	<b>37</b>
4.1	Overview . . . . .	37
4.1.1	Experimental Apparatus . . . . .	43
4.2	Production of Polarized Proton Beams . . . . .	46
4.2.1	Polarized Injection . . . . .	46
4.2.2	AGS to RHIC Transfer Line . . . . .	48
4.3	Maintaining Beam Polarization . . . . .	51
4.3.1	Siberian Snakes and Spin Rotators . . . . .	51
4.3.2	Measuring Beam Polarization . . . . .	51
4.4	The Pioneering High Energy Nuclear Interaction Experiment . . . . .	55
4.4.1	Overview . . . . .	55
4.4.2	The Spin Program . . . . .	59
4.4.3	Subsystems . . . . .	59
4.5	The Forward Upgrade . . . . .	66
4.5.1	The Muon Tracker . . . . .	67
4.5.2	The Resistive Plate Chambers . . . . .	69
4.5.3	Triggering and Data Acquisition . . . . .	80
<b>5</b>	<b>Data Wrangling</b>	<b>85</b>
5.1	Overview . . . . .	85
5.2	Raw Data to Reconstructed Parameters . . . . .	86
5.3	Choosing Analysis Variables . . . . .	87
<b>6</b>	<b>Feature Engineering</b>	<b>95</b>
6.1	The Basic Cut . . . . .	98
6.2	Simulations . . . . .	99
6.3	$W_{ness}$ : Likelihood Event Tagging . . . . .	105
6.3.1	Naive Bayes Classification . . . . .	105
6.4	Extended Unbinned Maximum Likelihood Selection: The Signal to Background Ratio . . . . .	115
6.4.1	Hadronic Background PDFs . . . . .	116
6.4.2	Muon Background and W-Signal PDFs . . . . .	126
6.5	Systematic Tests . . . . .	134

<b>7 Spin Analysis</b>	<b>136</b>
7.1 Overview . . . . .	136
7.2 Measured Beam Polarization . . . . .	138
7.3 Spin Patterns . . . . .	139
7.4 Muon Yields . . . . .	145
7.5 Calculation of $\epsilon_L$ and $A_L$ for $W \rightarrow \mu$ . . . . .	149
7.5.1 Asymmetry Calculation . . . . .	149
7.5.2 Discussion of Work Done By Analysis Team . . . . .	149
7.6 Data Validation . . . . .	149
7.6.1 Simulations and The Signal to Background Ratio . . . . .	149
7.6.2 Gaussian Process Regression . . . . .	149
7.6.3 Four Way Cross Validation . . . . .	149
7.6.4 Asymmetry Consistency Check . . . . .	149
7.6.5 Beam Polarization . . . . .	149
7.6.6 Beam Luminosity . . . . .	149
7.6.7 Code Cross Validation . . . . .	149
<b>8 The Vernier Analysis</b>	<b>150</b>
8.1 Overview . . . . .	150
8.2 Analysis Note Here . . . . .	150
8.3 W Cross Section . . . . .	150
<b>9 Discussion and Conclusion</b>	<b>151</b>
<b>Bibliography</b>	<b>152</b>
1 First Thingie . . . . .	161
2 Second Thingie . . . . .	161

# List of Figures

2.1	Two Greek philosophers, who made important philosophical contributions our understanding of matter. Empedocles (left), postulated the precursor to the elemental theory of matter[2] and Democritus (right), postulated the precursor to the atomic theory of matter. . . . .	7
2.2	Giants in the age of Empiricism, Newton (left) and Galileo (right) both made foundational contributions to Physics. Galileo lived in Italy, born in 1564 and dying in 1642. Newton lived in England from 1642 until his death in 1727 . . . . .	8
2.3	As we journey down further in scale, matter begins to look quite different. In fact, the models we use are scale dependent. Thomson 2.8, and Rutherford 2.5 began to see matter as collections of atoms (left) [3] (though not in terms of the orbital structure pictured), though it would not be until 20th century quantum mechanics that electron orbitals were discovered. Soon, nuclei were discovered to be divisible into protons an neutrons [4] (center), which in turn were discovered to be composed of a sea of quarks and gluons (right). (Right image drawn by the talented Astrid Morreale, PhD, [5]) . . . . .	10
2.4	Left: J.J. Thomson, who showed that cathode ray tubes were in fact producing the first observed subatomic particle: the electron. Right: A cartoon of Thomson's cathode ray tube setup. Electrons would be deflected by a magnetic field, sent from cathode to anode. . . . .	11
2.5	Ernest Rutherford, in his lab. [6] . . . . .	12
2.6	Ernest Rutherford's historic experiment, showing (top right) that atoms were composed of a small dense nucleus, in contrast to Thomson's 'pudding model' of homogeneous charge (top left). The experiment, (bottom left and right) contrast the expected results (bottom left) against the observed results (bottom right) [7]. . . . .	13
2.7	The attendees of the Solvay Conference in Brussels, 1927 [8]. . . . .	14
2.8	Paul Dirac, next to his original formulation of the Dirac Equation, describing the wave function for an electron with rest-mass $m$ , in terms of its spacetime coordinates. . . . .	15
2.9	Hideki Yukawa, the first Japanese Nobel Laureate and publisher of influential research on the theory of mesons, and other elementary particles [9]. . . . .	18
2.10	An old bubble chamber, once used at Fermilab, [10] . . . . .	19

---

2.11 An example of the photographs taken with a Bubble Chamber, in 1973. In this picture, we see a 300 $GeV$ proton producing particles as it travels through a hydrogen-filled bubble chamber at fermilab [11]. . . . .	20
2.12 A schematic of deep inelastic scattering, where the incoming electron inelastically scatters off the proton, producing results $X$ , via virtual photon exchange, $\gamma^*$ [12] . . . . .	23
2.13 "This diagram displays the structure of the standard model (in a way that displays the key relationships and patterns more completely, and less misleadingly, than in the more familiar image based on a 4x4 square of particles). In particular, this diagram depicts all of the particles in the standard model (including their letter names, masses, spins, handedness, charges, and interactions with the gauge bosons – i.e. with the strong and electroweak forces). It also depicts the role of the Higgs boson, and the structure of electroweak symmetry breaking, indicating how the Higgs vacuum expectation value breaks electroweak symmetry, and how the properties of the remaining particles change as a consequence." [13]. . . . .	25
2.14 <b>[FIGURE NEEDED] [CAPTION NEEDED]</b> . Results of EMC experiment showing that the structure function $g_1$ , tells us a thing about proton spin. . . . .	27
3.1 Figure from [14]. . . . .	29
3.2 Figure from [14]. . . . .	30
3.3 Shown: quark kinematics <b>[CAPTION NEEDED]</b> . . . . .	31
3.4 A summary of the various probes for longitudinally polarized protons. The " <b>Reaction</b> " column summarizes the reaction observed experimentally. The " <b>Dom. partonic process</b> " column describes the dominant process at the partonic level. The " <b>probes</b> " column shows which proton spin structure can be measured with the reaction. Finally, the leading order Feynman diagram for the partonic process is drawn. Figure is reproduced from: [15]. . . . .	34
3.5 Real $W^+$ production as produced at PHENIX. The helicity of the initial state fixes the helicity of the partonic participants due to the relativistic final state of the neutrino + the handedness of the $W$ boson. $x_1$ and $x_2$ are the momentum fractions of the quarks participating from the participant partons [15]. . . . .	35
4.1 A diagram of the acceleration process of RHIC is shown in the top panel, and aerial view is on bottom. RHIC is nearly four miles in circumference and collides a variety of ions at center-of-mass energies between $62GeV$ and $510GeV$ . . . . .	39
4.2 Runs 1 - 3 at RHIC focused on commissioning work for experiments measuring collisions at RHIC. Work was mostly characterized by heavy-ion measurements related to understanding Quark-Gluon Plasma. The spin program began with Run 5. Table produced from data posted at the RHIC run page [16]. . . . .	40

4.3	Though RHIC is currently still running (as of May 9, 2016), I include runs here up to and including the run producing my data set (Run 13). An unprecedented 13.3 cryo-weeks of running was awarded to the W-Physics group. Table produced from data posted at the RHIC run page [16]. . . . .	41
4.4	Upgrades to RHIC's electron lens have enabled massive improvements to luminosity - seen in the year 2013. The high luminosity was taken advantage of with an extra long proton+proton run. Figure obtained from [16] . . . . .	42
4.5	STAR (a) and PHENIX (b) with cutaways showing the event display for a heavy-ion collision as reconstructed by the detectors' electromagnetic calorimeters [17]. . . . .	43
4.6	Plot courtesy of Angelika Drees, of RHIC's Collider-Accelerator department. The blue beam (blue) and yellow beam (yellow) are overlaid over a 40 nanosecond time period. Even with bunches crossing a fixed point over 40 nanoseconds, this still corresponds to an overall bunch length of about 12 meters. Conversely, the bunch width is quite narrow - with Gaussian geometry, it is between 150 millimeters and 300 millimeters depending on the beam energy. Understanding the beam bunch geometry is a crucial component to understanding total the total luminosity delivered by RHIC to PHENIX. . . . .	45
4.7	RHIC's optically pumped polarized ion source. Produces 0.5-1.0 mA current of polarized $H^-$ ions. The optical pumping is pulsed at 400 $\mu s$ , [18] . . . . .	47
4.8	A view of the RHIC polarized injection system. We see a zoomed in technical view of the OPPIS to the booster (a), below, we see a zoomed out cartoon of the next step in the polarization injection system, including the AGS, and the feeder line to RHIC. . . . .	49
4.9	A schematic of the geometry of the AGS-to-RHIC transfer line [19]. . . . .	50
4.10	As beams are longitudinally rotated into position for collision, it is crucial to keep careful track of the magnet currents rotating the beams, as well as the overall polarization pattern. Shown is a carton of one potential polarization pattern. . . . .	52
4.11	The shift-crew display output for the Spin Monitor. The upper panel shows the polarization of the blue and yellow beams, and other panels summarize information including magnet currents (needed to understand the spin orientation), issues with data packet loss, the recognized spin-pattern, as well as a large boxed area on the lower left where errors could be shown to the shift crew along with the proper response. . . . .	53
4.12	Shown: The two main halves of the PHENIX Spectrometer. The central arms are shown via the beam-on view of PHENIX (left) and Forward Muon Arms are shown via the 90-degree rotated view. In both cases, the 2013 configuration is shown. The beams are brought into intersection at the geometric center of each figure (immediately between the BBCs) . . . . .	56

4.13 A flow chart summarizing the PHENIX DAQ [20]. From left to right, we can get a feel for the data flow at PHENIX. Shown is an event, the red splat on the far left. Particles from this event are transduced by a detector ('A Sub System'). The transduced signals are serialized into a detector specific data stream, such that the state of the detector's excitation can be recorded and reproduced later. This information is stored on the front-end-electronics modules (FEMs), and synchronized with timing information from the clock (ticks once every time there is a bunch crossing) and a Global Trigger decision, i.e. whether or not the right parts of the detector lit up to make this particular event worth keeping. After this, if the event is deigned by the heuristics to be worthy of keeping, the uncompressed serialized information is sent to the DCMs, where it is assembled into a packet, and then sent to the event builder (EvB), where all packets sharing a common collision are assembled into an event. The event is compressed into a proprietary PRDF format, and sent to the Buffer Boxes, which are a cache of high density local storage, which is later sent off to cold storage on magnetic tape drives. . . . .	57
4.14 Shown: a photograph of the BBC hugging the beryllium beam pipe near the center of PHENIX (top left), a schematic showing the relative size and location of the BBCs as compared to the rest of PHENIX (top right), and a schematic of the exact proportions of the detector as viewed alongside the beam pipe (bottom), along with the rapidity and azimuthal coverage [21] . . . . .	61
4.15 A diagram outlining the strategy for reconstructing the event z-vertex of a collision. Top: a cartoon of the North and South BBCs getting some particle penetration after an event. Bottom Right: a characteristic distribution of measured z-vertices for a short run taken in 2002 [21]. . . . .	62
4.16 A schematic of the Forward Vertex Detector, showing the silicon chip layers (light blue wedges), and readout electronics (green). They are mounted directly onto the Silicon Vertex Detector, which was not used in this analysis. The FVTX and SVD together are used in heavy ion analyses [22]. . . . .	64
4.17 Observing the simulated production of muon as a function of $p_T$ , we can see that in the kinematic region of $W$ production that the dominant sources of muons come from other processes. The new PHENIX muon trigger threshold is sensitive at $10 \text{ GeV}/c$ and above. The threshold is still high enough that with other methods, we can record all events which come from the $W$ boson, with triggering, whereas with the old threshold, this was impossible. . . . .	67
4.18 In 2013 with the final commissioning of the RPCs and the Forward Upgrade complete, we saw a drastic increase in rejection power, as planned. . . . .	69
4.19 As a muon passes through the layers of the RPC (left), the gas in the bakelite gap is ionized. This charge migrates and collects near the highly resistive graphite coating. An image distribution is induced on the overlapping read-out strip (right), which is passed along its own channel to the front-end electronics. . . . .	70

---

4.20 We can see the various layers that go into the construction of a typical RPC segment installed at PHENIX. A High Voltage bias is applied to the graphite coating on either side of bakelite gas-filled gaps. Readout strips are positioned between the two bakelite gaps. Finally, the entire double-gap structure is surrounded by a copper grounding cage, and wrapped in insulating mylar [23].	71
4.21 Two special tents inside building 912 at Brookhaven National Laboratory, built to house completed RPC octants and the laboratory used to construct and test the octants. . . . .	73
4.22 The North RPC Station 1 is installed on the muon tracker nosecone (left). Similarly we see the installation of the south RPC Station 1 (right). The metal tube in the center is the beryllium beam pipe. . . . .	74
4.23 Here, we see one of the many hard-working physicists who tirelessly worked in building 911: a dusty, and irradiated construct built along the AGS beamline. The physicist sits in the center of the RPC1 North chassis, for scale. More information can be found in [24]. . . . .	75
4.24 The chassis is prepared with insulating Kapton tape and mylar sheeting. The grooves along the bottom of the chassis are for routing cabling from the readout strips (shown later). The channels along the side of the chassis is for routing gas flow lines. . . . .	75
4.25 Foam shock insulation is added to the RPC 1 chassis. . . . .	76
4.26 The assembled Bakelite gas gap, ready for leak/pop testing, followed by burn in. . . . .	77
4.27 The egress port of the gas gap is carefully shielded with tape to prevent friction from causing tears, and routed out of the ports machined into the bottom of the chassis (right), with the final position of the first gap shown on the left. . . . .	78
4.28 The copper readout strips are mounted to the chassis. Each readout strip is soldered to a copper wire, which in turn are gathered into readout chips. . .	78
4.29 The final Bakelite gas gaps are installed on top of the copper readout strips. Gas lines are routed similarly to 4.27 . . . . .	79
4.30 A completed RPC 1 octant, interior assembly complete, left, and the outer assembly completed on the right. . . . .	79
4.31 Left: the cosmic test stand setup. RPC octants were sandwiched between scintillators to run performance and efficiency tests. An example of the clustering due to a cosmic ray is shown on the right, with a particle (red) activating one or two strips per octant (activation shown in green). . . . .	80
4.32 A schematic of the new muon trigger for recording W-Bosons [23] . . . . .	81
4.33 The position of the Front-End Electronics upgrades and new RPCs + Absorber are shown. Muon tracker stations are shown in blue (along with the front-end electronics). The RPCs sandwich the muon tracking stations and the MuID. The absorber material sits just inside of the muon arms, before the Forward Vertex Detectors and inner tracking stations of the muon tracker [23]	82
5.1 A schematic representation of the matching variables, DG0 and DDG0 at the intersection between the Muon Tracker and Muon Identifier [25] . . . . .	89

5.2	The PHENIX coordinate system is shown (RGB arrows) at the center of the nominal interaction point within PHENIX, the origin, in this quarter-cutaway drawing. The small black figures are actually miniaturized human beings, the PHENIX detector is very small - this is a full scale drawing of PHENIX. Shown: the x, y, and z coordinates, as well as the azimuthal coordinate, $\theta$ and polar coordinate $\phi$ [26] . . . . .	91
5.3	A nice summary of discriminating kinematic variables reproduced with permission from Dr. Chong Kim. We see the MuTR tracking planes in green, and a muon track penetrating the planes in red, and reference coordinates in the lower right-hand corner. The geometric relationship between the roads, reconstructed track are shown in the annotations. . . . .	92
6.1	A cartoon of the dataset composition. The data, even after the Forward Upgrade, is mostly composed of hadronic background, which has tricked our Muon Tracker. . . . .	96
6.2	Here, we see the stacked cross-sections of all simulated processes as a function of $p_T$ . All data shown has been created from the PISA+PYTHIA framework. Top Left: South $\mu-$ , Top Right: South $\mu+$ , Bottom Left: North $\mu+$ , Bottom Right: North $\mu-$ . Figure reproduced from my analysis note. Dr. Ralf Seidl produced the original [27] . . . . .	104
6.3	Low correlations between the signal variable distributions (from simulation), and the background variable distributions make this data set a good candidate for classification using Naive Bayes . . . . .	106
6.4	A cartoon of the decision tree to determine the PDF cocktail to use for quantifying the $W_{ness}$ of a given track. The track's properties are used to traverse the tree, and select the cocktail contents. . . . .	108
6.5	Left: the distribution of rpc3dca for each arm and charge, produced from the PHENIX data set, after the basic cut. Right: the same distributions from a simulation of the W-Signal. . . . .	109
6.6	Left: the distribution of rpc1dca for each arm and charge, produced from the PHENIX data set, after the basic cut. Right: the same distributions from a simulation of the W-Signal. . . . .	110
6.7	Left: the distribution of DDG0 for each arm and charge, produced from the PHENIX data set, after the basic cut. Right: the same distributions from a simulation of the W-Signal. . . . .	110
6.8	Left: the distribution of chi2 for each arm and charge, produced from the PHENIX data set, after the basic cut. Right: the same distributions from a simulation of the W-Signal. . . . .	111
6.9	Left: the distribution of dcar for each arm and charge, produced from the PHENIX data set, after the basic cut. Right: the same distributions from a simulation of the W-Signal. . . . .	111
6.10	Left: the distribution of DG0 for each arm and charge, produced from the PHENIX data set, after the basic cut. Right: the same distributions from a simulation of the W-Signal. . . . .	112

6.11 After $W_{ness}$ tagging, we can visualize the classification of signal from background by comparing the distribution of $W_{ness}$ in physics data, and the simulated data data. Note that the vertical is plotted on a log scale. The two distributions have been normalized prior to plotting. . . . .	113
6.12 We look at the fraction of signal and background remaining in the total data set as we make successively higher cuts in $W_{ness}$ . At the turning point of the blue distribution (the fraction of remaining signal) is where we choose to cut the data, corresponding to removing data with a $W_{ness}$ value of less than 0.95. . . . .	114
6.13 The first column of plots is $\eta$ plotted as a function of $W_{ness}$ where we see a 2D histogram of the even distribution. The middle column is $dw_{23}$ as a function of $W_{ness}$ , and the right column is a simple histogram of $W_{ness}$ . The rows all correspond to the same arm and charge. From top to bottom: North, $\mu+$ , North $\mu-$ , South $\mu+$ , North $\mu-$ . Distributions shown here are all from the physics data set. . . . .	117
6.14 The first column of plots is $\eta$ plotted as a function of $W_{ness}$ where we see a 2D histogram of the even distribution. The middle column is $dw_{23}$ as a function of $W_{ness}$ , and the right column is a simple histogram of $W_{ness}$ . The rows all correspond to the same arm and charge. From top to bottom: North, $\mu+$ , North $\mu-$ , South $\mu+$ , North $\mu-$ . Distributions shown here are all from simulated W-genic data set. . . . .	118
6.15 A summary of the fourth degree polynomial fit (Equation 6.7) to the $W_{ness}$ distribution from the physics dataset in the background region. . . . .	119
6.16 From left to right the columns are: $dw_{23}$ for the full $W_{ness}$ range, $0.1 < W_{ness} < 0.3$ , $0.3 < W_{ness} < 0.7$ , $0.3 < W_{ness} < 0.7$ , $0.7 < W_{ness} < 0.9$ , and finally the extrapolated shape for $W_{ness} > 0.95$ . In red, we see the 1D projection of the 2D distribution to the slice. This overlays a green curve, which is a fit done independently to a slice. The rows are labeled with the Arm and charge corresponding to the subdivided dataset. As you can see, the matching is often exact, between green and red curves. As the final column is the extrapolation, there is no slice-fit. . . . .	121
6.17 The four parameters from the co-axial Gaussian parameterization of $dw_{23}$ as a function of $W_{ness}$ . Though some parameters ( $G_{factor}$ , $N\mu-$ ) may appear to be non-linear, note that the uncertainty on some bins is quite large. Rows are arm/charge, labeled on the left, while columns are co-axial Gaussian parameters, summarized in Equation 6.10 . . . . .	122
6.18 The red wire-frame is the resultant fit of to the $dw_{23}$ vs $W_{ness}$ distribution. We extrapolate the shape of $dw_{23}$ to the signal region to obtain the hadronic background PDF for $dw_{23}$ . . . . .	123
6.19 An overhead view of the various results of the $dw_{23}$ vs $W_{ness}$ fit for each arm and charge combination. . . . .	124
6.20 Abraham, Mike, Ralf and Daniel all independently parameterized and extrapolated $dw_{23}$ obtaining consistent results. Figure prepared by Dr. Francesca Giordano [27] . . . . .	125

6.21 Left Column: The hadronic background PDFs, Middle Column: The Summed Muon Background PDFs, Right Column: The W-Signal PDF. For South Arm, $\mu+$ . . . . .	127
6.22 Left Column: The hadronic background PDFs, Middle Column: The Summed Muon Background PDFs, Right Column: The W-Signal PDF. For South Arm, $\mu-$ . . . . .	127
6.23 Left Column: The hadronic background PDFs, Middle Column: The Summed Muon Background PDFs, Right Column: The W-Signal PDF. For North Arm, $\mu-$ . . . . .	128
6.24 Left Column: The hadronic background PDFs, Middle Column: The Summed Muon Background PDFs, Right Column: The W-Signal PDF. For South Arm, $\mu+$ . . . . .	128
6.25 Here, we see the preliminary results of the EULMF for the 2013 Run. On the left, $\eta$ is shown. In the middle, $dw_{23}$ . On the right, $dw_{23}$ is subdivided into the three standard $\eta$ bins. In all cases, we see the unbinned data in black (with error bars), and the sum of the three fits in black. In Blue, we can see the fake-muon hadronic background. In Green, the muon background. In blue, we see the W-Signal result. The area under the curves represents the yield, relative to the total. Figure prepared by Dr. Ralf Seidl [27]. Shown: South Arm, $\mu-$ . . . . .	129
6.26 Here, we see the preliminary results of the EULMF for the 2013 Run. On the left, $\eta$ is shown. In the middle, $dw_{23}$ . On the right, $dw_{23}$ is subdivided into the three standard $\eta$ bins. In all cases, we see the unbinned data in black (with error bars), and the sum of the three fits in black. In Blue, we can see the fake-muon hadronic background. In Green, the muon background. In blue, we see the W-Signal result. The area under the curves represents the yield, relative to the total. Figure prepared by Dr. Ralf Seidl [27]. Shown: South Arm, $\mu+$ . . . . .	130
6.27 Here, we see the preliminary results of the EULMF for the 2013 Run. On the left, $\eta$ is shown. In the middle, $dw_{23}$ . On the right, $dw_{23}$ is subdivided into the three standard $\eta$ bins. In all cases, we see the unbinned data in black (with error bars), and the sum of the three fits in black. In Blue, we can see the fake-muon hadronic background. In Green, the muon background. In blue, we see the W-Signal result. The area under the curves represents the yield, relative to the total. Figure prepared by Dr. Ralf Seidl ???. Shown: North Arm, $\mu-$ . . . . .	131
6.28 Here, we see the preliminary results of the EULMF for the 2013 Run. On the left, $\eta$ is shown. In the middle, $dw_{23}$ . On the right, $dw_{23}$ is subdivided into the three standard $\eta$ bins. In all cases, we see the unbinned data in black (with error bars), and the sum of the three fits in black. In Blue, we can see the fake-muon hadronic background. In Green, the muon background. In blue, we see the W-Signal result. The area under the curves represents the yield, relative to the total. Figure prepared by Dr. Ralf Seidl ???. Shown: North Arm, $\mu+$ . . . . .	132

7.1	Shown: the average beam polarization per run over the course of the 2013 data set. All of the runs in the analysis were indexed from 0 to approximately 1000, and plotted in the order that they were taken. The blue open circles are from the blue beam, the yellow open circles are for the yellow beam. . .	138
7.2	The blue beam had a tighter polarization distribution, peaked at just about 50% polarization, whereas the yellow beam's polarization distribution was broader, still peaking at about 55%. . . . .	139
7.3	Here, we see the crossing distribution for every run taken for the 2013 data set. We use the typical code for arm/charge. The top row is for the South Arm. The bottom row is for the North Arm. The left column is for negative charge, the right column is for positive charge. . . . .	141
7.4	Here, we can see the yield for various crossing combinations as taken from the dataset itself, rather than the database. We see a very consistent distribution between the various possible crossing patterns. In this case, the horizontal axis is the crossing pattern code - 0:++, 1:-+, 2:+-, 3:--. Any slight difference between yields for each pattern is well below our experimental precision. . . . .	142

# List of Tables

4.1	A summary of PHENIX hardware [28]. Electron/pion separation and Pion/Kaon separation requires the Time of Flight (ToF) working with PbGl and PbSc data. PbGl refers to "Lead Glass Scintillator" and PbSc refers to "Lead Scintillator". The Muon Identifier (Muon ID, MuID) can help separate muons from hadrons. . . . .	58
4.2	A brief summary of the FVTX design parameters [22] . . . . .	63
4.3	The design characteristics of the RPCs [23] . . . . .	72
4.4	A typical run from the 2013 data set. This run was numbered '396418', according to PHENIX's numbering scheme. The 'name' column is the name given to the physics trigger, with one trigger per row. Names are descriptive, such that when boolean operators appear, this corresponds to that operation on the presence of that particular subsystem's trigger signal. Though a W-boson can occur for any triggered events, events firing a 'MUON' styled trigger are most likely. One can get a flavor for the relative frequency of triggers in the "Raw Trigger Rate" column (Hz), as well as the relative importance of that trigger in data taking, from the "Scale Down" column. Rare triggers have a smaller scale-down than common ones. The live-time column describes the fraction of the time that PHENIX saw an event worthy of recording, and then recorded it. . . . .	83
5.1	Variables characterizing events overall . . . . .	89
5.2	Muon tracker variables. Generally, this data set is indexed on a subevent level, where one event will contain all reconstructed muon tracks seen for that event. . . . .	90
5.3	A summary of the variables reconstructed from FVTX raw data [29]. . . . .	90
5.4	RPC Track matching variables . . . . .	91
6.1	The Basic Cuts used in the Run 13 analysis. lastGap refers to the last gap in the MUID which saw a $\mu$ candidate event. The fourth gap is the furthest penetration possible, therefore suggesting a high energy muon. Other parameters are described in Tables 5.1, 5.2, 5.3, and 5.4 . . . . .	98

---

6.2	Simulated sub processes in Run 13 including their generated event numbers as well as the corresponding luminosity and cross sections. Dr. Sanghwa Park has done an extensive analysis of the simulated data to determine an appropriate k-factor. Process which contribute very little to the muon background include W had, W tau, and $d\gamma$ ; they are scaled to zero. . . . .	100
6.3	$\eta$ dependent trigger efficiencies are calculated for the South arm in 20 $\eta$ bins. Each correction has both systematic and statistical error accounted for. . . . .	101
6.4	$\eta$ dependent trigger efficiencies are calculated for the North arm in 20 $\eta$ bins. Each correction has both systematic and statistical error accounted for. . . . .	102
6.5	South arm $W \rightarrow \mu^-$ fit results per analyzer [27] . . . . .	133
6.6	A summary table from the results of the EULMF to the unbinned data set, summed to one $\eta$ bin per arm and charge. . . . .	135
7.1	Patters P1-P8 were filled into RHIC for the first portion of the 2013 data taking period, with P21-P28 being filling in the second portion. For each pattern, from left to right, bunch 0 in the blue or yellow beam is filled with the leftmost polarization, with bunch 1 getting the next, and so on. The pattern repeats as soon as the end has been reached, until we get to the last filled bunch, with any empty bunch being 'polarized' as if it were not empty. . . . .	144
7.2	Due to much higher integrated luminosity of Run 13, we can actually subdivide the muon yields into rapidity bins for the purposes of trying to cover a wider kinematic range (at the expense of uncertainty). Here, we see the South arm's yields for each helicity combination of colliding protons, with the polarization of the blue beam and yellow beams color coded in column 2. Recall that of the yields, about 20% are actual signal events. . . . .	146
7.3	Due to much higher integrated luminosity of Run 13, we can actually subdivide the muon yields into rapidity bins for the purposes of trying to cover a wider kinematic range (at the expense of uncertainty). Here, we see the North arm's yields for each helicity combination of colliding protons, with the polarization of the blue beam and yellow beams color coded in column 2. Recall that of the yields, about 20% are actual signal events. . . . .	147
7.4	As a consistency check to previous analysis which only had enough statistics for two $\eta$ bins, one forward, and one backward for $A_L^{W+}$ , we have binned the data to match. Here, we see a division of the data by arm, charge, and helicity combination, which is color-coded for the polarization of the blue and yellow beams. Note that of the yields, only $\sim 20\%$ of the yield comes from a W-Boson decay. . . . .	148

# Chapter 1

## Introduction

A brief note - figures used here without attribution were either: produced by me, produced in collaboration with others in my working group, or obtained by authors who labeled them for reuse without attribution. Other figures here are all fair-use.

THIS THESIS IS CURRENTLY AN UNPUBLISHED DRAFT. IT HAS NOT BEEN SUBMITTED AND MAY HAVE MISSING CITATIONS AND CONTENT

### 1.1 A Brief History of the Proton

The angular momentum of the proton and neutron has been a subject of study for the last 30 years. One of the challenges of particle physics is to create a framework which can accurately describe matter, as well as predict the behavior of matter at all energy scales. Protons and neutrons are baryons which make up the majority of the mass in the visible universe, yet fully understanding the origins of their properties - such as mass and spin, still eludes us. However, through the application of the scientific method over many generations of physicists, we have magnificently described this important particle, and understood much of its properties. However, one property which still defies our descriptions is its fundamental angular momentum, spin.

Our understanding of the proton has evolved and sharpened since the first experiments in deep inelastic scattering showed that the proton is not a fundamental particle [30]. Gell-Mann later planted the seeds of a theoretical framework which could in part describe some of the structure of baryons, a class of hadrons which we may naively describe as

composed of three 'valence quarks' [31]. We can apply well known spin-sum rules to the individual spins of the valence quarks which compose the proton in our naive valence-model to produce a correct prediction for the protons' spin  $\frac{1}{2}$ . When experimenters set out to measure the contribution of these valence quarks in 1988 at the EMC experiment [1], they were flabbergasted to find that the valence quarks carry only a small fraction of the proton's spin. Although recent papers [32] suggest that this 'spin crisis' is simple due to mis-attribution of spin, most literature to date has focused on understanding how to model the proton with parton distribution functions. These parton distribution functions come in many varieties, and probe different degrees of freedom within the proton, in both the case of unpolarized parton distribution functions, and polarized parton distribution functions.

## 1.2 Scope and Objectives of This Work

This thesis will describe the research I carried out between May of 2010 through August of 2016. I will often quote work that was carried out in active collaboration with Ralf Seidel, Francesca Giordano, Daniel Jumper, Sanghwa Park, Abraham Meles and Chong Kim. Daniel, Abraham, Ralf, Francesca, and myself all worked on the 2013 polarized proton data set taken at RHIC with PHENIX. This analysis comprises the body of work devoted to calculating  $A_L$  for the  $W \rightarrow \mu$  decay. Since 2013, the five of us collaborated closely on all aspects of the work, which provided invaluable cross-checks at nearly every stage. Many of the figures in this document were produced by our collective efforts, and I will do my best to cite when possible, if one analyzer played a particularly large role in generating the data or visualization, however after several years of working together, I will certainly fail to attribute, or mis-attribute at times.

The other portion of this thesis will discuss the Vernier Analysis, which is instrumental for every single-cross-section calculation taken with RHIC data. The thrust of the Vernier Analysis is to determine the beam luminosity at PHENIX's interaction point, so as to normalize these cross-section calculations. This is done with a series of specialized Vernier-Scans, where beams are scanned across one-another in order to measure beam geometry. The luminosity can then be calculated from first principals, and compared to the advertised machine luminosity published by RHIC's collider-accelerator department. I began working with the Vernier Analysis under the tutelage of K. Oleg Eyser, but eventually

moved to work independently on the analysis, producing an entire software framework for handling data cleaning, analysis, visualization and simulation.

## Chapter 2

# Historic Perspective on the Structure of Matter and Spin

### 2.1 The Phenomena of Spin

Spin is a fundamental quantity possessed by all elementary particles. We use the word 'spin' to describe the property, because particles which possess spin, behave as though they have some kind of intrinsic, hidden rotation, as if they were 'spinning'. The dimension of spin, therefore is angular momentum. What is somewhat bizarre about spin, is that we do not observe anything physically spinning - although there are some phenomena (such as orbital angular momenta) which can be naively thought of as a 'spinning system' (but this description escapes classical analogy, due to its quantum, probabilistic nature). The role of Spin in Physics is of foundational importance, and yet, we have not successfully produced a model which can accurately predict the spin of hadrons.

The presence of spin in relativistic particles creates the phenomena of chirality, which has huge implications for how elementary particles can generate structure in matter itself [33]. In the case of the weak interaction, the presence of spin, which creates Chiral spinors breaks the left-right symmetry of weak coupling in matter (a fact which will be exploited in this thesis to probe the spin of the proton sea).

The phenomena of spin also changes the rules for how ensembles of particles may exist in a potential. Particles with spin are fermions, and because these particles must obey Fermi-statistics, we can observe structure in matter in the universe. Without spin,

DRAFT

---

DRAFT

DRAFT

the world as we know would collapse on itself, making any kind of extended non-exotic structures which currently exist by virtue of the Pauli exclusion principal, impossible.

## 2.2 A Brief History of Relevant Physics

The study of Spin is really just an outgrowth of the general study of matter. Our models for matter, and the underlying structure of matter (in the modern sense), represents over a hundred years of experimental and theoretical efforts, and thousands of years of contemplating what makes up the universe.

Although indulgent on my part, I find it interesting, and humbling, to try and map out the path that humanity and science has trodden on its way to understanding the building blocks of the universe. To find the first time that humanity had murmurings that suggested our visible world is built from invisible, fundamental building blocks, we must travel back, nearly 2,500 years into the past.

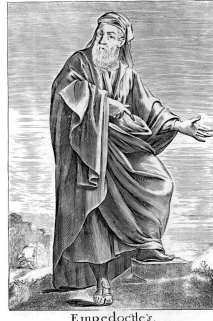
Rather than provide a complete mathematical background to my measurement from a historic perspective, I will instead focus on the experimental historic narrative surrounding our quest to understand the structure of matter. After, I will present mathematical formalism relevant to this measurement directly - if the reader desires an exhaustive mathematical context, I invite them to read the classic tomes on Field Theory by Weinberg and reference the numerous theses written by my colleagues in theoretical physics and phenomenology.

### 2.2.1 Ancient Foundations

Sometime around 490 - 370 BCE lived two philosophers, Empedocles (Fig 2.1a), and Democritus (Fig 2.1b). Both men lived approximately at the same time, and made huge philosophical leaps in attempting to understand the nature of the visible world.

Democritus was part of a movement of thought which was first to make the intellectual jump that perhaps matter was not a continuum, but instead, composed of 'atomon', small, indivisible particles which when configured together, created all that is observable [36]. Empedocles was making equally important philosophical strides - in a manner complimentary to Democritus' opinion that matter must be made of atomon, Empedocles argued that matter is composed of elemental primitives [2].

Although Empedocles' 'periodic table' was only composed of Earth, Water, Fire, and Air, the idea that some unseen transmutation of elemental forces might generate observables in nature with quite different (but perhaps reminiscent) properties then the 'pure



(a) Empedocles [34]



(b) Democritus [35]

Figure 2.1: Two Greek philosophers, who made important philosophical contributions our understanding of matter. Empedocles (left), postulated the precursor to the elemental theory of matter[2] and Democritus (right), postulated the precursor to the atomic theory of matter.

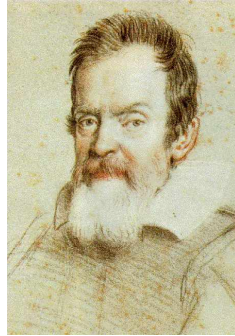
substances' was an important step forward. Proto-scientists were beginning to generate models which derived our complicated observations, from simpler forms.

It took centuries of cultivation, leading up to the Scientific Revolution, for the next great steps to occur, for science. Thankfully, the luminaries of the Islamic Golden Age kept the fires of inquiry burning [37].

### 2.2.2 The Scientific Revolution

Thanks to the mathematical foundations laid out, build, and maintained by the minds of the Islamic Golden Age, Europe was well poised to reignite the flames of scientific inquiry, during the post Renaissance Scientific Revolution [37].

This period of growth in science was unprecedented during the Scientific Revolution, thanks to the seeds of empiricism germinated during the Islamic Golden Age, fertilized by the Italian Renaissance, and helped to flourish through British Empiricism [38].



(a) Galileo [39]



(b) Newton

Figure 2.2: Giants in the age of Empiricism, Newton (left) and Galileo (right) both made foundational contributions to Physics. Galileo lived in Italy, born in 1564 and dying in 1642. Newton lived in England from 1642 until his death in 1727

#### 2.2.2.1 Galileo Galilei

While Galileo is best known for his work in Observational Astronomy, his importance to science extends beyond this. During his years in exile for his controversial views of the heliocentric universe, he produced some of his most important scientific work in kinematics [40]. What made this work remarkable is the care that Galileo took in merging careful mathematical modeling with well designed experimentation. This methodical approach to inquiry laid the foundation for others to slowly begin to pull back the curtains obscuring physical law.

Galileo's formalization of the scientific method inexorably set science on a course to delving deep into the nature of matter, and the laws of nature.

### 2.2.2.2 Isaac Newton

Fittingly born in the same year as Galileo's death, Isaac Newton would carry on Galileo's legacy of rigorous mathematical modeling mixed with experimentation. Perhaps no other scientist has touched so many different aspects of physics, from theories of propagation of light, to celestial mechanics, to mathematics, and kinematics.

Newton's Principia is perhaps the most important scientific work ever published. It opened the doors of the universe in a way that nobody has since duplicated. Newton's laws of motion are still taught in school today, and although they have since been shown to be inaccurate at the smallest and largest scales, they still provide startlingly accurate predictions for the regular motion of matter.

One particularly tantalizing theory of Newton's was the corpuscular theory of light. Although not his most influential theory by far, the idea that an apparently continuous medium such as a beam of light might be made of small packets of energy (corpuscles) turned out to be partially right [41].

Newton's theories, and contributions to science are enormous, and have moved us deeper still into the underpinnings of matter. It would not be until roughly 200 years after his death, in the 19th century, that we finally can take the first steps into the world of the atomic, and sub-atomic: the world of the proton.

### 2.2.3 Atomic Theory

On the shoulders of giants such as Newton and Galileo, science finally came to know the tool which has been indispensable to modern particle physics: scattering. Rutherford and Thompson both carried out the most important scattering experiments in modern science, and provided us with the first hints of a hidden, quantum world, though it would not be until the 20th century that these important experiments would be fully contextualized with a theory of quantum scattering.

Scattering experiments offer a very powerful method where we one uses a well known initial state of matter (typically in the form of a beam), allows this beam to interact with an unknown configuration of matter, and measures the scattered beam. By carefully studying the kinematics of the scattered beam, we can create models which allow us to understand the structure of the target matter or describe the nature of the interaction between the beam and target.

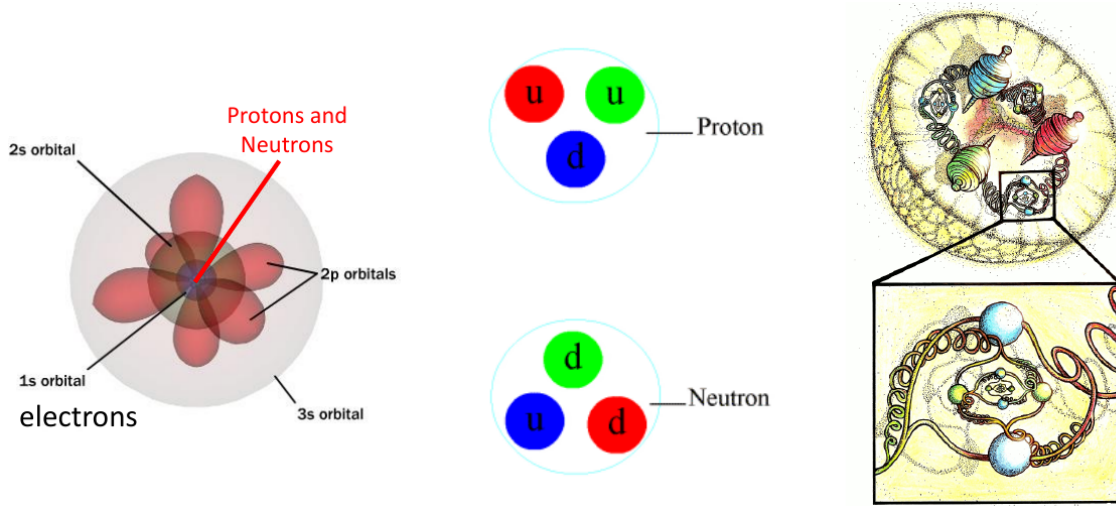


Figure 2.3: As we journey down further in scale, matter begins to look quite different. In fact, the models we use are scale dependent. Thomson 2.8, and Rutherford 2.5 began to see matter as collections of atoms (left) [3] (though not in terms of the orbital structure pictured), though it would not be until 20th century quantum mechanics that electron orbitals were discovered. Soon, nuclei were discovered to be divisible into protons and neutrons [4] (center), which in turn were discovered to be composed of a sea of quarks and gluons (right). (Right image drawn by the talented Astrid Morreale, PhD, [5])

### 2.2.3.1 John Dalton

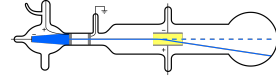
While many had postulated the existence of atoms, the first evidence based theory which suggested the existence of atoms was produced by John Dalton in the early 19th century. Dalton made an important conceptual leap to relate the existence of stoichiometric ratios in chemistry to the presence of small, individual functional units in his experiments with chemical reactions. Dalton's realization was only made possible due to his careful accounting of reactants in his experiments.

It was not until Einstein's 1905 theory on Brownian Motion was experimentally verified by Jean Perrin to place limits on the mass and size of atoms that Dalton's atomic theory was ultimately vindicated [42].

### 2.2.3.2 J.J. Thompson



(a) J.J. Thomson [43]



(b) Cathode Ray Tube [44]

Figure 2.4: Left: J.J. Thomson, who showed that cathode ray tubes were in fact producing the first observed subatomic particle: the electron. Right: A cartoon of Thomson's cathode ray tube setup. Electrons would be deflected by a magnetic field, sent from cathode to anode.

Thomson (Figure 2.4) would discover that atoms are not the smallest, indivisible piece of matter. In his landmark experiment, he used cathode ray scattering experiments to show that cathode rays were in fact subatomic particles. He showed these cathode rays were identical to particles given off by the photoelectric effect, and that these same particles were responsible for electric current. He had discovered the electron. And, if atoms were not the smallest piece of matter, then perhaps, atoms themselves might not be 'indivisible' as previously thought [45].

### 2.2.3.3 Ernest Rutherford

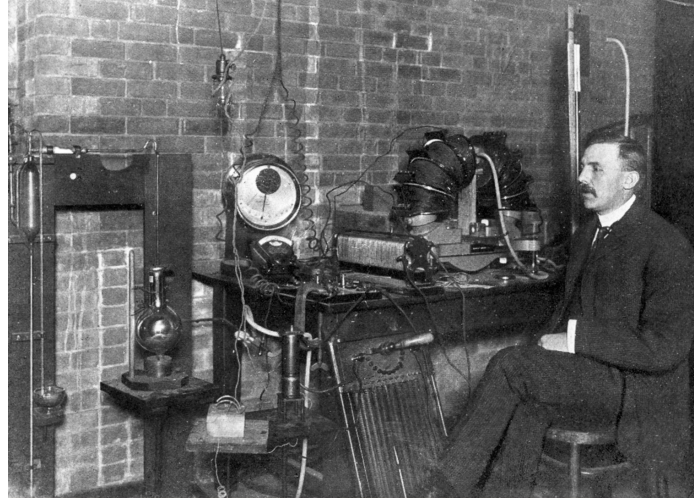


Figure 2.5: Ernest Rutherford, in his lab. [6]

Ernest Rutherford (Fig 2.5) was the first to show that atoms themselves were highly structured - and consisted of a small dense center, later called the nucleus.

Rutherford's work with radioactivity was of fundamental importance, he discovered and classified both alpha-particle radioactivity and beta-particle radioactivity. Further studies into these types of nuclear radiation would unlock the nucleus of atoms through the work of future scientists. Notably, Rutherford discovered the proton.

Rutherford's proposed planetary model for the nucleus, while technically wrong, shifted paradigms from the pudding model of atoms, to the more familiar nucleus + electron cloud model which has been spectacularly modeled and verified with the forthcoming scientists which defined the field of quantum mechanics.

Rutherford's work helped push us out of the cocoon of classical mechanics into the weird world of the quantum mechanics - scientists would soon find that the nucleus is not just a dense concentration of charge, but a probabilistic structure, with rich sub nuclear structure.

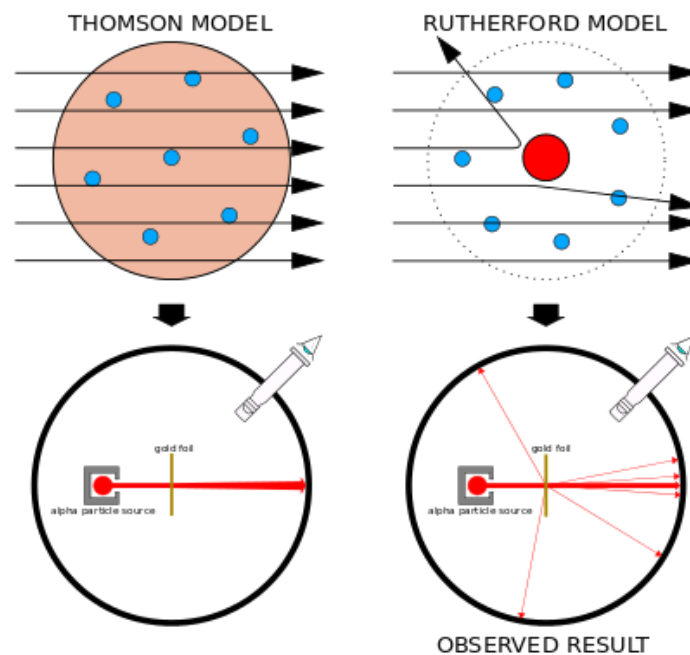


Figure 2.6: Ernest Rutherford's historic experiment, showing (top right) that atoms were composed of a small dense nucleus, in contrast to Thomson's 'pudding model' of homogeneous charge (top left). The experiment, (bottom left and right) contrast the expected results (bottom left) against the observed results (bottom right) [7].



Figure 2.7: The attendees of the Solvay Conference in Brussels, 1927 [8].

### 2.2.4 Early Quantum Theory

During Rutherford's time, experiments were already underway which were investigating modeling light as a wave phenomena. This was in contrast to Newton's (unverified) corpuscular theory of light. The argument whether light was wave-like or particle-like eventually lead to a classical field theory describing light, and the electromagnetic interaction, yet scientists such as Max Planck were proposing theories which required the quantization of light [46]. Einstein would show that in his analysis of the photoelectric effect, that light indeed was quantized into 'corpuscles'. The nascent atomic theory of matter was also hinting at a hidden, quantized world.

At the Solvay Conference in Brussels, Figure 2.7, in 1927, we saw an unprecedented gathering of some of the most important figures in modern physics, all in one place, laying down the foundations of what would become quantum mechanics. These scientists defined the nature and rules of quantum mechanics - the weird model which accommodates a duality

of matter - both wave-like, and particle like. The notion that probing the structure of matter did not yield a simple, deterministic hierarchy of structure was revolutionary, confusing, and bizarre, and still is to this day.

It was found that not only light possesses this wave-particle duality, but also the very particles that make up atoms as well. These models were formalized by Dirac, Hilbert and Von-Neumann.

Though experiment tended to lead theory, regarding understanding the composition and rules of interactions in matter, in the mid 20th century, further refinements and additions to quantum mechanics gave birth to quantum field theory. While early quantum models were very successful at describing static particles trapped in static potentials - such as refining atomic theory to include predictions of observed atomic spectra, more work was needed to understand the relationship between electrical currents, light and magnetism. These concepts were all related by Maxwell [47] in the latter half of the 19th century, but did not make good predictions for systems in motion.

Dirac was first to create a model for describing the electron, its behavior in electromagnetic fields, and photon emission and absorption, under fully relativistic and quantum conditions [48]. Dirac's model was so successful, that it would become the basis for what we now call quantum electrodynamics. Much of the mathematical formalism has been reused to describe other field theories, which are the ultimate language which model and describe the structure of matter - including the insides of a proton.



(a) Paul Dirac, 1933 [49]

$$\left( \beta mc^2 + c \left( \sum_{n=1}^3 \alpha_n p_n \right) \right) \psi(x, t) = i\hbar \frac{\partial \psi(x, t)}{\partial t} \quad (2.1)$$

(b) The Dirac Equation

Figure 2.8: Paul Dirac, next to his original formulation of the Dirac Equation, describing the wave function for an electron with rest-mass  $m$ , in terms of its spacetime coordinates.

Dirac's work also began to incorporate relativistic effects in his wave equations modeling the electron, as well as crucially incorporating the spin (I.e. Dirac Spinors) of

these particles, which were important for making precise predictions for atomic spectra [48].

By this time, the proton was already known to reside in the enigmatic nucleus of atoms, however, attempts to use Quantum Electrodynamics to describe the state of the nucleus failed - it was clear that there was a very strong force, holding together the protons of a nucleus tightly - far in excess of the electromagnetic repulsion felt by the positively charged particles. There was a completely different coupling strength between this apparent strong nuclear force, and the better known electromagnetic coupling. Further complicating an understanding of the nucleus is the fact that as the length scale of probing decreases, the energies probed increase, fundamentally making the nucleus a relativistic object. Experimental physics would once again, forge ahead, in attempting to understand the inner workings of the nucleus, in the time-honored tradition of performing scattering experiments.

### 2.2.5 Early Particle Physics and The Eightfold Way

The hydrogen atom, and its spectra was well modeled with quantum mechanics by the end of early 20th century, however attempts to study Helium were not as successful. However, in 1932, when Chadwick turned a beam of helium particles (at that time only known as  $\alpha$  particles) on a sample of Beryllium, he observed that neutral, non-ionizing, penetrating radiation was produced [50]. Photons were ruled out as possible candidates, leading to the discovery of the neutron. Protons and neutrons were hypothesized by Heisenberg to both be the same state of a new conceptual particle, the nucleon, [51]. In the same year, Anderson discovered the positron.

By 1934, Hideki Yukawa (Fig. 2.9) had created an effective field theory for interactions of 'elementary particles' (at this time, thought to be protons and neutrons). He predicted the existence of mesons, and wrote down an effective field theory which described how protons and neutrons bind together in the nucleus [52].

Though non-relativistic quantum mechanics was mostly complete by 1934, scientists were already hard at work incorporating relativistic corrections to the theory. Experiments with cosmic rays soon revealed the existence of muons and the first observation of mesons.

Three separate paths eventually lead to the development of particle accelerators, which are to date, the best mechanism we possess in physics to probe nuclear structure. These accelerators are an outgrowth of ever more intense Rutherford-style experiments, Tandem Van-Der-Graaf generators, resonant acceleration techniques, RF linacs, and betatron accelerators [53].

By the 1950's, a cornucopia of strange new particles had been discovered, both matter and antimatter. But scientists drove forward, deeper, yearning to discover what was fundamental. By the 50's, neutrinos had been proposed, as well as Kaons, Pions, and Lambdas. Physicists were doing nuclear chemistry, in a sense, attempting to work out how quickly some particles decayed, and what decays were allowed or forbidden - science entered an age of nuclear alchemy.

"Strange" particles were discovered ( $K$  and  $\Lambda$ ), so called because in bevatron experiments, they were produced in great quantities, but were slow to decay, unlike the faster  $\pi$  decay. Gell-Mann proposed that this strangeness in matter was due to a new quantum number (he called it 'strangeness'). The name stuck. [54], [55], [50]



Figure 2.9: Hideki Yukawa, the first Japanese Nobel Laureate and publisher of influential research on the theory of mesons, and other elementary particles [9].

The introduction of new conserved quantities, and the vast proliferation of particles was in full swing - the subatomic world by the 1950's was confusing, and complex. In his book "The God Particle", Leon Lederman recalled his adviser, Enrico Fermi frustratedly remarking 'Young Man, if I could remember the names of these particles, I would have been a botanist'. At this time, in the mid 1950's, the number of mesons and baryons which had been discovered were at least in the dozens, if not more.

While the use of particle accelerators were speeding us along in our search for the structure of matter, one particular invention truly revolutionized the field - the bubble chamber (Figures 2.10 and 2.11.)

The bubble chamber was essentially a large vat of supercritical fluid which could easily be caused to boil with small perturbations. This feature was exploited, by positioning a bubble chamber in a magnetic field (to cause charged tracks to bend) near the interaction

point between a particle beam and a fixed target. The bubble chamber itself was sometimes the target - since a popular liquid to use was hydrogen.



Figure 2.10: An old bubble chamber, once used at Fermilab, [10]

Invented by Donald Glaser in 1952, the bubble chamber was 'perfected' by Luis Alvarez when he helped to develop a version which could be used with liquid hydrogen. Hydrogen was desirable as a substance due to its extremely simple structure, which supplied much cleaner results than other fillings, unlike the original filler, Ether.

Soon after the advent of bubble chambers, physicists were able to macroscopically image these new, exotic particles interacting with normal matter as well as decaying - and develop novel computer techniques to analyze and catalog the massive influx of data.

The break-through came in 1961, when Gell-Mann and Nishijima leveraged recognized the underlying symmetry of the interactions taking place, and created what would be known as 'the eightfold way'. This theory created a scheme for organizing the observed baryons and mesons according to their properties in groupings called "octets". These octets



Figure 2.11: An example of the photographs taken with a Bubble Chamber, in 1973. In this picture, we see a  $300 \text{ GeV}$  proton producing particles as it travels through a hydrogen-filled bubble chamber at fermilab [11].

were in fact representations of the elements of members of the  $SU(3)$  group. Another way of stating this, is that Gell-Mann had discovered the underlying structure of flavor-symmetry between the three lightest quarks -  $u$ ,  $d$ , and  $s$ . This work directly led to the development of the quark model of matter, the foundation of what would become the foundation of the standard model of particles. To date, the standard model is the most successful theory describing particles, and their interactions.

Gell-Mann's quark model soon made important predictions which were later verified, notably the  $\Omega^-$ , which was the ground-state particle of the spin-3/2 decuplet - discovered at Brookhaven National Laboratory (the same lab from which my research has been derived!).

Gell-Mann formalized his quark theory of matter in 1964, however, due to the unforeseen phenomena of color confinement, it would be several years before evidence of quarks composing baryons and mesons was directly obtained from deep inelastic scattering experiments.

### 2.2.6 Deep Inelastic Scattering and The Parton Model

Deep inelastic scattering experiments, Figure 2.12 were a natural outgrowth of Rutherford's experiment from the late 19th century. There are a few notable differences. Rutherford's scattering experiments can be modeled classically, by using a classical potential as a scattering source, and then solving as usual using an impact parameter and potential as in central force problems. Rutherford's experiments were considered generally 'elastic' because the target absorbed very little kinetic energy from the projectile, and no new particles were created from the kinetic energy of the projectile-target system.

However, in the late 20th century, scattering experiments became highly inelastic - targets would absorb a lot of kinetic energy - sometimes so much that targets would break apart and the kinetic energy of the system would create particles. When referring to scattering as 'deep inelastic', the 'deep' part refers to the process by which a scattering event occurs between a target particle and an internal, pointlike element of some complex ensemble (such as a nucleus).

During the process of a high energy interaction between the projectile (often a beam) and the target, some kind of interaction occurs between the target and the projectile, in a way that changes the state of the projectile, and generates matter due to the high energies involved. One can observe the state of the projectile, and account for the matter which is created, and if there are laws which govern how the state of the projectile changes, or the kinds of matter that can be created, then we can run the clock backwards, reconstructing the kind of interactions that happened, to learn something about nuclear structure (or even partonic structure). In this way, one can also identify conserved quantities, which in turn suggest physical symmetries, which in turn help to build models.

One can think of interaction of a beam and target in terms of a probability of interaction - and this formalism will be discussed further in chapters related to the Vernier Analysis I worked on. Succinctly, however, one can mathematically 'separate' part of this interaction probability into a quantity called a 'cross-section', often denoted as  $\sigma$  for a total cross section, or  $d\sigma$  for a differential cross section, or even  $\frac{d\sigma}{d\Omega}$  to refer to a differential cross section scattered into a solid angle. The  $\sigma$  of any scattering experiment can be represented many different ways.

From a theoretical standpoint, we can represent protons (and other baryons) by selecting the relevant internal degrees of freedom we may want to study, and then devising

some rules for the internal structure. We may be interested in the momentum fraction carried by some distribution of partons, or how the relative populations of partons within a certain kinematic regime changes with distance/energy scale. For all of these cases, we use parton distribution functions, or structure functions. Concretely, these functions depend on:

A subcategory of deep inelastic scattering is 'Semi-Inclusive Deep-Inelastic Scattering'. This refers to a case where a beam (say a lepton, such as an electron) interacts inelastically with a pointlike internal structure of a target particle, and a hadron is produced (such as a  $\pi^+$ ), which is then detected. Semi-Inclusive Deep-Inelastic scattering is then the process by which the scattered lepton and a specific hadron are measured in the final state of the interaction (but other particles that might be produced are neglected or ignored).

I said the word parton, which I have been carefully avoiding, but now the cat's out of the bag. Nuclei, as we will learn, are not elementary particles, but instead, are built up from what we assume are fundamental, elementary particles. Deep inelastic scattering experiments slowly revealed that nuclei (individual protons and neutrons) were not elementary particles, but instead, composite particles. It is natural to assume then, that the properties of protons and neutrons are not fundamental either. And in fact, the vast zoo of particles that were discovered in early inelastic scattering experiments, such as  $\pi$  or  $K$  or  $\Lambda$  (discussed briefly earlier) were not fundamental either.

In Michael Riordan's excellent 1992 summary of the discovery of quarks, Riordan lays out a very succinct and thorough history of the late 20th century experimental and theoretical works which built on Rutherford and Gell-Man's work. Riordan states that surprising 'results came from a series of electron scattering experiments...from 1967 through 1973' at MIT and SLAC, which comprised the first set of evidence produced in favor of the partonic model. As described earlier, Gell-Mann created a three-quark model to produce predictions consistent with these observations [56].

By the 1970's, collaborations between Bjorken, Feynman, and others had produced a coherent partonic model which contained quarks, and force mediating gluons. Additionally, the concept of Structure functions had been developed. Modified from Rutherford's original scattering formula, this new formula to describe the cross section of deep inelastic scattering incorporated structure functions, which separated out the momentum exchange between target and projectile (via a virtual photon), and isolated this from  $W_1$  and

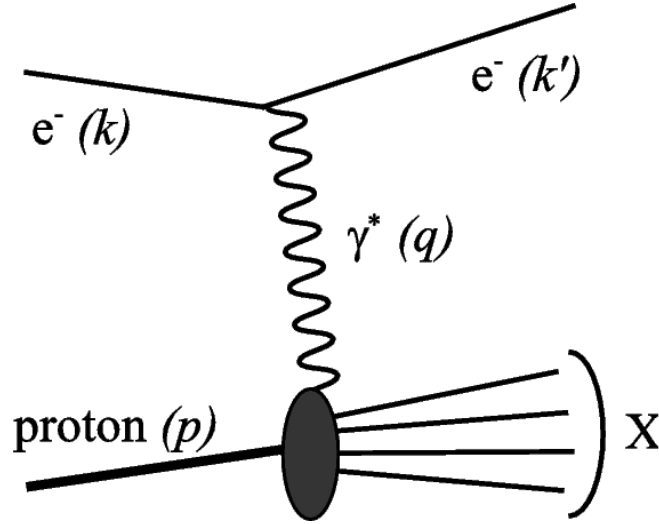


Figure 2.12: A schematic of deep inelastic scattering, where the incoming electron inelastically scatters off the proton, producing results  $X$ , via virtual photon exchange,  $\gamma^*$  [12]

$W_2$ , structure functions which were experimentally measured quantities representing the electron-proton interaction (the 'physics-y' part of the interaction).

This period of time, from 1970 - 1990 was truly the golden age of Deep Inelastic Scattering Experiments - the biggest laboratories running experiments were (and some are still running) The European Organization for Nuclear Research (CERN), The Stanford Linear Accelerator Center (SLAC), and The German Electron Synchrotron (DESY). Thousands of papers were published - some groundbreaking, such as the CERN's European Muon Collaboration experiment which showed a measurement of the spin asymmetry and determination of the proton structure function  $g_1$  in muon-proton deep inelastic scattering [1].

The formalism of scattering theory continued to evolve during the booming period of particle physics from 1960 to present day. Though the mechanics of scattering experiments have remained essentially unchanged, vast improvements in technology in detectors, data collection and reconstruction, and beam production have evolved from Geiger and Marsden's humble beginnings to create scientific measurements of particles and their properties with exquisite and unprecedented precision. The kind of precision I'm talking about is exemplified in Brookhaven National Laboratory's E821 Muon ( $g-2$ ) experiment - which measured the anomalous magnetic moment,  $g-2$ , of the muon to a precision of 7 parts in

ten million [57].

The advent of structure functions hailed an era of non-point-like baryonic matter. The mathematics of scattering formalism had to change to accomodate the underlying physical distribution of partonic matter in baryons. Deep Inelastic Scattering continued to probe various portions of these structure functions, and the structure of the standard model began to come into focus, distilled into the relatively simple mathematical structure of group theory. Concretely, the standard model is a gauge theory, which contains the internal symmetries of  $SU(3) \times SU(2) \times SU(1)$ , Figure 2.13. The Standard Model is said by some to be "complete" with the discovery of the Higgs Boson, yet with emergent phenomena such as proton spin, it does not provide a straightforward prediction. The model still has not included gravitation and relativistic effects fully - and probably isn't entirely correct.

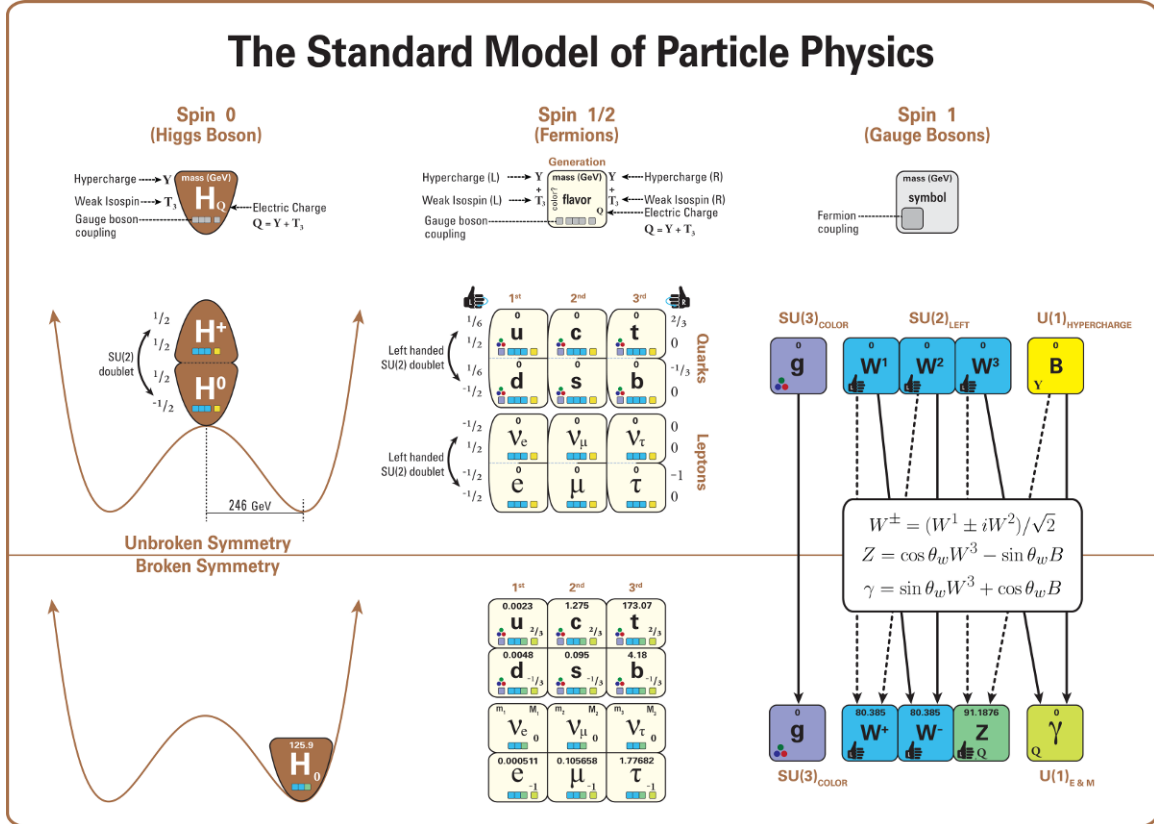


Figure 2.13: "This diagram displays the structure of the standard model (in a way that displays the key relationships and patterns more completely, and less misleadingly, than in the more familiar image based on a 4x4 square of particles). In particular, this diagram depicts all of the particles in the standard model (including their letter names, masses, spins, handedness, charges, and interactions with the gauge bosons – i.e. with the strong and electroweak forces). It also depicts the role of the Higgs boson, and the structure of electroweak symmetry breaking, indicating how the Higgs vacuum expectation value breaks electroweak symmetry, and how the properties of the remaining particles change as a consequence." [13].

## 2.3 World Experiments in Deep Inelastic Scattering

International Symposium on Spin Physics: [http://inspirehep.net/search?ln=en&cc=Conferences&ln=en&cc=Conferences&p=Symposium+on+Spin+Physics+SPIN&action\\_search=Search&sf=conferencestartdate&so=d&rm=&rg=250&sc=0&of=hb](http://inspirehep.net/search?ln=en&cc=Conferences&ln=en&cc=Conferences&p=Symposium+on+Spin+Physics+SPIN&action_search=Search&sf=conferencestartdate&so=d&rm=&rg=250&sc=0&of=hb)

International Symposium on Deep Inelastic Scattering: [http://inspirehep.net/search?ln=en&cc=Conferences&ln=en&cc=Conferences&p=Deep+Inelastic+Scattering+DIS&action\\_search=Search&sf=conferencestartdate&so=d&rm=&rg=250&sc=0&of=hb](http://inspirehep.net/search?ln=en&cc=Conferences&ln=en&cc=Conferences&p=Deep+Inelastic+Scattering+DIS&action_search=Search&sf=conferencestartdate&so=d&rm=&rg=250&sc=0&of=hb)

The following Deep Inelastic (Inclusive and Semi-Inclusive) experiments highlighted here represent a period of science from approximately 1979 to present day, and focus mostly on efforts to understand the structure of baryons. Along the way, much of the Standard Model was discovered and codified, but I will try to keep the narrative focused on how experiments contributed to understanding both the structure of baryons in terms of parton distribution functions, and structure functions. Structure functions fall into two broad categories, within the scope of this work - cases which ignore the contribution of spin and cases which include the contribution of spin. Relevant maths will be presented largely only in the context of the experiments, which does not do a very good service to the progression of ideas on the theoretical side of physics, but hey, I'm an experimentalist. Once finished, I will present a brief overview of our best models developed for understanding the proton spin, developed in parallel with these experimental efforts, before transitioning to a discussion of RHIC, and my efforts on the subject.

Many of the experiments to be discussed here took data over a long period of time - some experiments were in competition, while others complimented each-other.

Though there are other experiments which currently take data complimentary to RHIC, I will cover only the experiments which directly lead to RHIC's spin program, with apologies to those experiments I've left out.

EIC white paper: [14]

Discuss SLAC, CERN, DESY, and RHIC. Discuss although DESY took data with HERA from 1992 - 2007, analysis and publication of the data is still ongoing.

HepData: <http://hepdata.cedar.ac.uk/review/f2/index.shtml>

### 2.3.1 CERN - European Muon Collaboration: 1979-1997

Overview Paper: Highlights of the European Muon Collaboration [58]

A measurement of the spin asymmetry and determination of the structure function  $A_{g_1}$  in deep inelastic muon-proton scattering: [1].

An investigation of the spin structure of the proton in deep inelastic scattering: [59].

Although Gell-Mann's simple quark model of baryons [60] predicts the correct quantity for the spin of the proton, the work of Ashman et al (1988) [1] at the European Muon Collaboration directly measured a portion of the proton structure function  $g_1$  and found that a rather small fraction of the proton spin comes from quarks - and most of the spin is carried by the gluons (Figure 2.14).



Figure 2.14: [FIGURE NEEDED] [CAPTION NEEDED]. Results of EMC experiment showing that the structure function  $g_1$ , tells us a thing about proton spin.

inSPIRE: collaboration:'European Muon'

### 2.3.2 SLAC - E142: 1993-1994

inSPIRE: collaboration:'E142'

### 2.3.3 SLAC - E143: 1992-1999

inSPIRE: collaboration:'E143'

### 2.3.4 DESY - ZEUS: 1992-Present

inSPIRE: collaboration:'ZEUS' H1+ZEUS combined results: [https://www.desy.de/h1zeus/combined\\_results/](https://www.desy.de/h1zeus/combined_results/) ZEUS figures: [http://www-zeus.desy.de/zeus\\_papers/zeus\\_papers.html](http://www-zeus.desy.de/zeus_papers/zeus_papers.html)

### 2.3.5 CERN - Spin Muon Collaboration: 1993-1998

Spin Asymmetry  $A_1$  and structure functions  $g_1$  [61] NLO QCD analysis of spin structure function  $g_1$  [62] inSPIRE: collaboration:'Spin Muon'

### 2.3.6 SLAC - E154: 1994-1997

inSPIRE: collaboration:'E154'

### 2.3.7 DESY - HERMES: 1995-2007

inSPIRE: collaboration:HERMES HERMES website, publications, figures: <http://www-hermes.desy.de/>

### 2.3.8 SLAC - E155: 1997-2003

inSPIRE: collaboration:'E155'

### 2.3.9 CERN - COMPASS: 2005-Present

inSPIRE: collaboration:'COMPASS'

### 2.3.10 DESY - H1: 1992-Present

H1 Publications: <http://h1.desy.de/e104552/e104555/> inSPIRE: collaboration:'HERA' (HERA is the accelerator) inSPIRE: collaboration:'H1' (this is the data)

## Chapter 3

# Models and Associated Probes For Proton Spin Structure

### 3.1 Modeling the Proton Structure

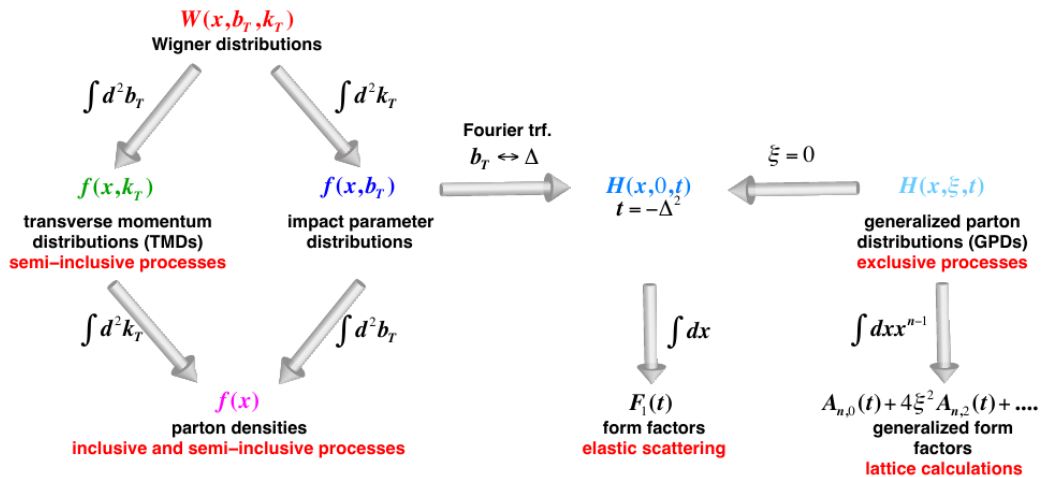


Figure 3.1: Figure from [14].

## 3.2 Structure Functions

Spin structure overall: [14] pp 29-31 Longitudinal spin structure: [14] pp 32-43

		Quark Polarization		
		Un-Polarized (U)	Longitudinally Polarized (L)	Transversely Polarized (T)
Nucleon Polarization	U	$f_1 = \text{circle with dot}$		$h_1^\perp = \text{circle with dot} - \text{circle with dot}$ Boer-Mulders
	L		$g_{1L} = \text{circle with dot} \rightarrow - \text{circle with dot} \rightarrow$ Helicity	$h_{1L}^\perp = \text{circle with dot} \rightarrow - \text{circle with dot} \rightarrow$
	T	$f_{1T}^\perp = \text{circle with up arrow} - \text{circle with down arrow}$ Sivers	$g_{1T}^\perp = \text{circle with up arrow} - \text{circle with up arrow}$	$h_1^\perp = \text{circle with up arrow} - \text{circle with up arrow}$ Transversity $h_{1T}^\perp = \text{circle with up arrow} - \text{circle with up arrow}$

Figure 3.2: Figure from [14].

### 3.2.1 Parton Distribution Functions

### 3.2.2 Polarized Parton Distribution Functions

Discuss DSSV fits

### 3.2.3 Proton Spin Decomposition with the Ellis-Jeffe Sum Rule

Gauge invariant Ellis-Jeffe

$$\langle P, \frac{1}{2} | \hat{J}_z | P, \frac{1}{2} \rangle = \frac{1}{2} = \frac{1}{2} \Delta \Sigma + L_q + J_g \quad (3.1)$$

Infinite momentum decomposition:

$$\langle P, \frac{1}{2} | \hat{J}_z | P, \frac{1}{2} \rangle = \frac{1}{2} = \frac{1}{2} \Delta \Sigma + L_q + \Delta g + L_g \quad (3.2)$$

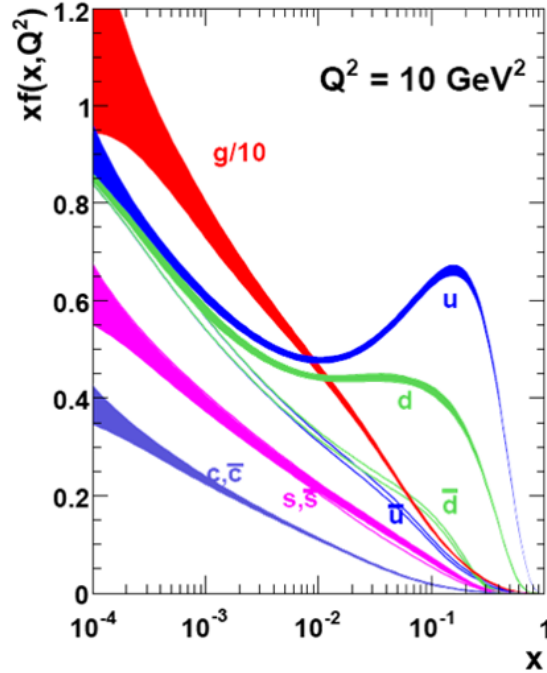


Figure 3.3: Shown: quark kinematics [CAPTION NEEDED]

Quark decomposition:

$$\Delta\Sigma = (\Delta u + \Delta \bar{u}) + (\Delta d + \Delta \bar{d}) + (\Delta s + \Delta \bar{s}) \quad (3.3)$$

### 3.2.4 The Spin Asymmetry: An Experimental Probe

Write in terms of the cross-section of polarized scattering.

## 3.3 that sweet table from Delia hasch

## 3.4 Experimental Probes for Proton Spin Structure

### 3.4.1 Physics Probes for the Proton Spin

### 3.4.2 W Production

The standard model tells us that W production occurs through a pure vector-axial interaction, this implies that the helicity of the parents particles - in particular  $u + \bar{d} \rightarrow W^+$

and  $\bar{u} + d \rightarrow W^-$  have fixed helicities, due to the relativistic final state neutrino (which is not measured, of course). To visualize the leading order of W production, with regards to the quark-sea element being probed, the leading order diagrams for the interaction are shown in Figure 3.5 [15]

Since  $\Delta q$ , the polarized parton distribution function can be split into contributions from valence quarks, and also sea quarks, understanding  $\Delta \bar{q}$  is an important step towards understanding  $\Delta q$  better to better understand the total proton spin.

Though both protons in the collision are polarized, the polarization of one participant proton can be effectively ignored by summing over all polarization states for one of the two protons. With this assumption, we may construct a single spin asymmetry for colliding protons by counting difference in the number of positively and negatively polarized W's produced in collisions, scaled by the total production:

$$A_L^W = \frac{1}{P} \times \frac{N_-(W) - N_+(W)}{N_-(W) + N_+(W)} \quad (3.4)$$

This is a relatively easy experimental probe to measure (assuming that we can accurately count events which produced a W, which naturally, is nearly impossible, as we will see in Section 6.4).

As we saw earlier, in Section 3.2.2, we can write an asymmetry in terms of the scattering cross section for the process responsible for particle yields. These cross-sections were shown to be written in terms of polarized parton distribution functions, thus, we cut to the chase to write down the full expression of the theoretical asymmetries for this process in terms of those parton distribution functions.

The following equations all contain an implied integration over  $x_1$  and  $x_2$ .

For  $W^+$  and  $u$ :

$$A_L^{W^+} = \frac{u_-(x_1)\bar{d}(x_2) - u_+(x_1)\bar{d}(x_2)}{u_-(x_1)\bar{d}(x_2) - u_+(x_1)\bar{d}(x_2)} \quad (3.5)$$

For  $W^+$  and  $\bar{d}$

$$A_L^{W^+} = \frac{\bar{d}_-(x_1)u(x_2) - \bar{d}_+(x_1)u(x_2)}{\bar{d}_-(x_1)u(x_2) + \bar{d}_+(x_1)u(x_2)} \quad (3.6)$$

Observationally, we see a superposition of 3.5 and 3.6, which is expressed as ??:

$$A_L^{W^+} = \frac{\Delta u(x_1)\bar{d}(x_2) - \Delta \bar{d}(x_1)u(x_2)}{u(x_1)\bar{d}(x_2) + \bar{d}(x_1)u(x_2)} \quad (3.7)$$

For the case of  $W^-$ , we observe  $\bar{d}$  and  $u$ : For  $W^-$  and  $d$ :

$$A_L^{W^+} = \frac{d_-(x_1)\bar{u}(x_2) - d_+(x_1)\bar{u}(x_2)}{d_-(x_1)\bar{u}(x_2) - d_+(x_1)\bar{u}(x_2)} \quad (3.8)$$

For  $W^-$  and  $\bar{u}$

$$A_L^{W^+} = \frac{\bar{u}_-(x_1)d(x_2) - \bar{u}_+(x_1)d(x_2)}{\bar{u}_-(x_1)d(x_2) + \bar{u}_+(x_1)d(x_2)} \quad (3.9)$$

Observationally, we see a superposition of 3.8 and 3.9, which is expressed as 3.10:

$$A_L^{W^-} = \frac{\Delta d(x_1)\bar{u}(x_2) - \Delta \bar{u}(x_1)d(x_2)}{d(x_1)\bar{u}(x_2) + (\bar{u})(x_1)d(x_2)} \quad (3.10)$$

Kinematics of the collision can simplify the equations even further, when at very forward or very backward rapidities [15].

Reaction	Dom. partonic process	probes	LO Feynman diagram
$\vec{pp} \rightarrow \pi + X$ [61, 62]	$\vec{gg} \rightarrow gg$ $\vec{qg} \rightarrow qg$	$\Delta g$	
$\vec{pp} \rightarrow \text{jet(s)} + X$ [71, 72]	$\vec{gg} \rightarrow gg$ $\vec{qg} \rightarrow qg$	$\Delta g$	(as above)
$\vec{pp} \rightarrow \gamma + X$ $\vec{pp} \rightarrow \gamma + \text{jet} + X$ $\vec{pp} \rightarrow \gamma\gamma + X$ [67, 73, 74, 75, 76]	$\vec{qg} \rightarrow \gamma q$ $\vec{qg} \rightarrow \gamma q$ $\vec{q}\bar{q} \rightarrow \gamma\gamma$	$\Delta g$ $\Delta g$ $\Delta q, \Delta \bar{q}$	
$\vec{pp} \rightarrow DX, BX$ [77]	$\vec{gg} \rightarrow c\bar{c}, b\bar{b}$	$\Delta g$	
$\vec{pp} \rightarrow \mu^+ \mu^- X$ (Drell-Yan) [78, 79, 80]	$\vec{q}\bar{q} \rightarrow \gamma^* \rightarrow \mu^+ \mu^-$	$\Delta q, \Delta \bar{q}$	
$\vec{pp} \rightarrow (Z^0, W^\pm) X$ $\vec{pp} \rightarrow (Z^0, W^\pm) X$ [78]	$\vec{q}\bar{q} \rightarrow Z^0, \vec{q}'\bar{q}' \rightarrow W^\pm$ $\vec{q}'\bar{q}' \rightarrow W^\pm, q'\bar{q} \rightarrow W^\pm$	$\Delta q, \Delta \bar{q}$	

Figure 3.4: A summary of the various probes for longitudinally polarized protons. The ”**Reaction**” column summarizes the reaction observed experimentally. The ”**Dom. partonic process**” column describes the dominant process at the partonic level. The ”**probes**” column shows which proton spin structure can be measured with the reaction. Finally, the leading order Feynman diagram for the partonic process is drawn. Figure is reproduced from: [15].

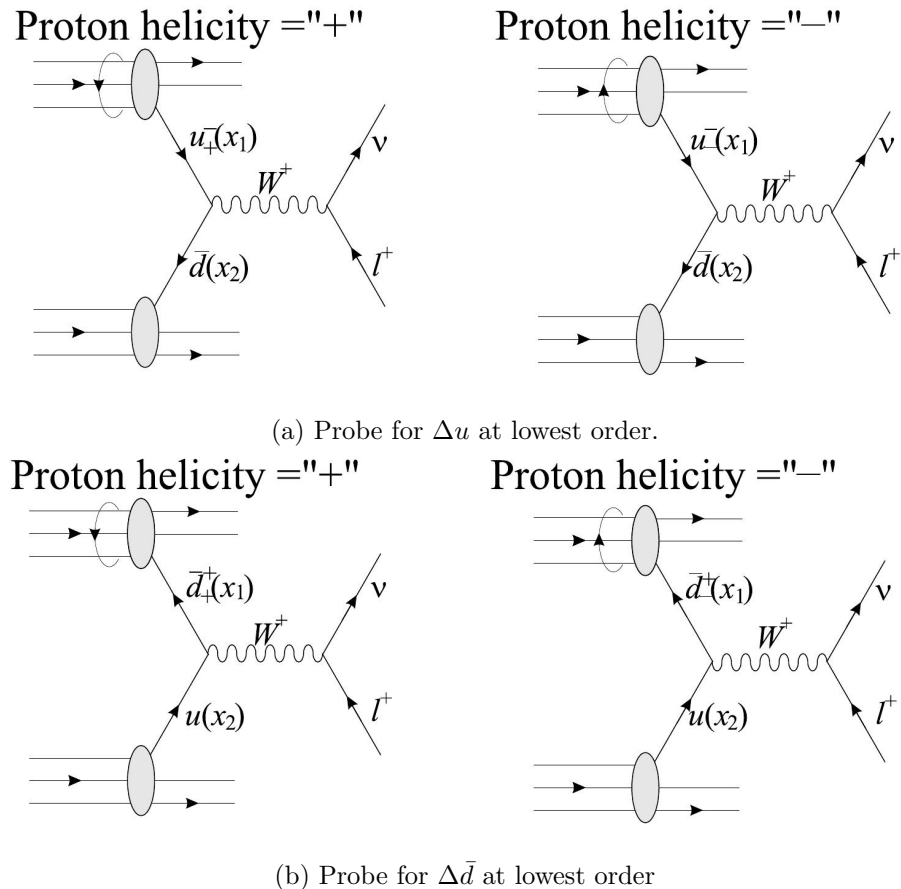


Figure 3.5: Real  $W^+$  production as produced at PHENIX. The helicity of the initial state fixes the helicity of the partonic participants due to the relativistic final state of the neutrino + the handedness of the  $W$  boson.  $x_1$  and  $x_2$  are the momentum fractions of the quarks participating from the participant partons [15].

### 3.5 Cross Sections and Luminosity

- vernier analysis note intro, equations
- summarize the papers on Lumoninosity

## Chapter 4

# The Relativistic Heavy Ion Collider

### 4.1 Overview

While there have been many experiments which have performed deep inelastic scattering over the years, the experiments built around the Relativistic Heavy Ion Collider at Brookhaven National Laboratory are positioned to take advantage of the unique accelerator.

The Relativistic Heavy Ion Collider (RHIC) is the world's only intersecting ring particle accelerator which is capable of producing polarized proton beams. The beams are differentiated with the mnemonic "Blue" and "Yellow" beam. The Blue beam circulates clockwise when viewed from above the RHIC complex, the Yellow beam circulates counter-clockwise. As is typical for intersecting ring experiments, the beams are bunched, with bunches of ions intersecting at designated intersection points, around which experiments are built. The Blue beam is nominally used to time these collisions, such that experiments which have bunch-sensitive measurements (i.e. any experiment where bunch polarization is important) can associate the correct bunch polarization with the correct collision. This will be discussed more in the section of beam-polarization ([4.3](#)).

RHIC generally separates data taking into beam 'fills' which are uniquely numbered, and for which general data characterizing the machine state is logged in various databases and online logbooks. Each fill is a unique population of beam ions, circulating around the RHIC rings. The beam ions are subdivided into discrete collections of ions called bunches. At the end of each fill, (typically 8 hours of collisions), the beam is dumped, and a new fill is generated. Experiments built around RHIC generally subdivide fills into 'runs',

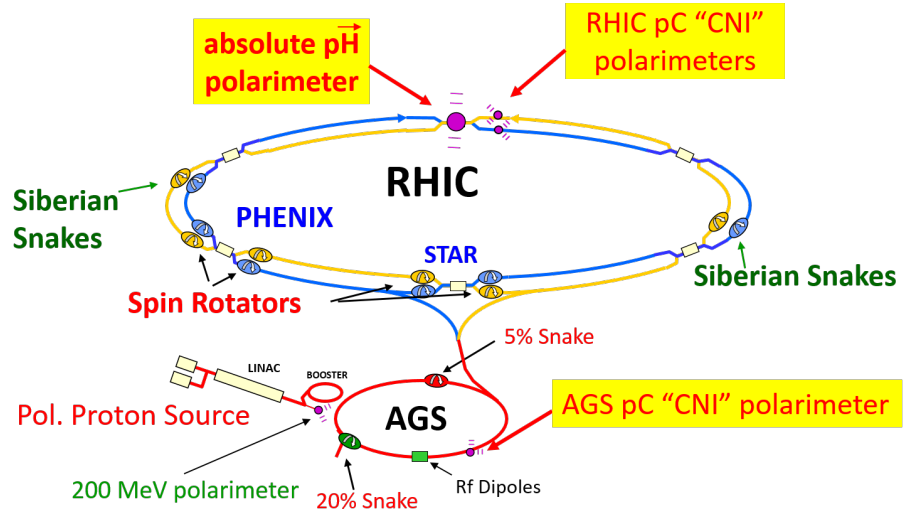
where a run is a period of time where the experiment is taking data. At PHENIX, runs are always segregated within a fill - no run will ever contain data from multiple fills.

Scientists at RHIC have come up with many ingenious ways to create and maintain beam polarization, once this is accomplished, various kinematically select probes are engineered, based on collisions observed which provide important cross-checks to DIS data as well as original discoveries and measurements of proton structure. RHIC is a unique collider in that it is quite flexible. Beams may be transversely or longitudinally polarized, a variety of ions may be used to fill the beams. To date, RHIC has collided many beam ions and species, summarized in Figure 4.2 and Figure 4.3.

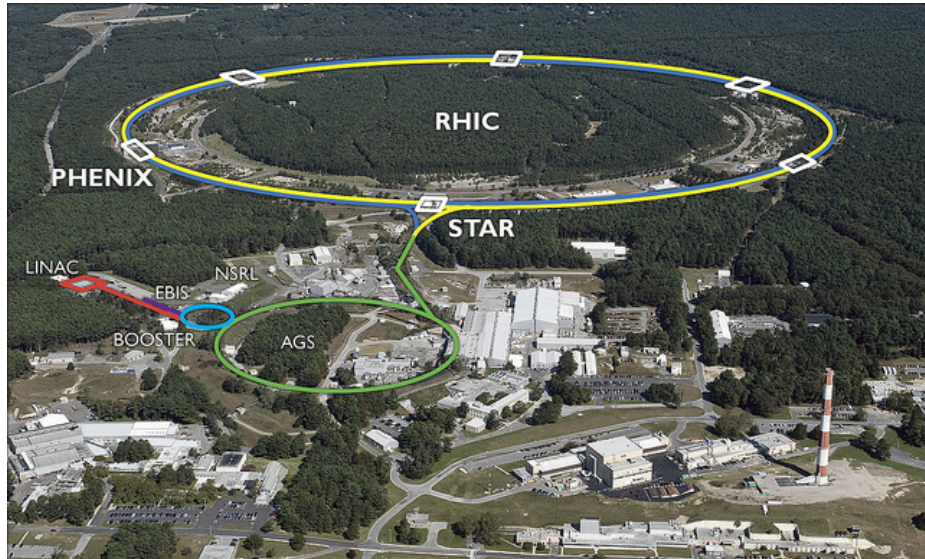
RHIC is an experiment which has been built on top of previous accelerator experiments which have been reused magnificently - a Linear Accelerator, a booster ring, and an Alternating Gradient Synchrotron, all of which now have been repurposed to create a high quality collider physics experiment. Many experiments are still set up around various egress points along the acceleration chain, which are publicised on the Brookhaven National Laboratory website [www.bnl.gov](http://www.bnl.gov)

At the time of writing of this thesis (Spring of 2016), there are two experiments which are actively taking data from collisions produced by RHIC: The Pioneering High Energy Nuclear Interaction Experiment (PHENIX, Section 4.4, Figure 4.5), and the Solenoidal Tracker at RHIC (STAR, Figure 4.5). STAR and PHENIX are complimentary to each other - PHENIX has a very high precision centrally covering Electromagnetic Calorimeter, and other high precision detectors, but lacks full kinematic coverage, whereas STAR has lower precision, but has nearly full kinematic coverage around the beam intersection at its center.

RHIC's luminosity and beam polarization has been continuously improving (Figure 4.4) since RHIC was first turned on. As we will discuss later (4.5), this increased luminosity observed in 2013, was maximally leveraged with upgrades to the PHENIX detector.



(a) Diagram of RHIC Accelerator Complex, (Figure from Kiyoshi Tanida)



(b) Aerial photograph of RHIC Complex [63]

Figure 4.1: A diagram of the acceleration process of RHIC is shown in the top panel, and aerial view is on bottom. RHIC is nearly four miles in circumference and collides a variety of ions at center-of-mass energies between  $62\text{GeV}$  and  $510\text{GeV}$ .

RHIC operating modes and total integrated luminosity delivered to 6 experiments						
Run	species	total particle energy [GeV/nucleon]	calendar time in physics	total delivered luminosity	average store polarization, (H-jet) <sup>*</sup>	
<b>Run-1</b> CY2000, FY2000 33.6 cryo-weeks	$^{197}\text{Au}^{79+} + ^{197}\text{Au}^{79+}$	27.9	3 shifts	< 0.001 $\mu\text{b}^{-1}$	—	
	$^{197}\text{Au}^{79+} + ^{197}\text{Au}^{79+}$	65.2	5.3 weeks	20 $\mu\text{b}^{-1}$	—	
<b>Run-2</b> CY2001/02, FY2001/02 40.7 cryo-weeks	$^{197}\text{Au}^{79+} + ^{197}\text{Au}^{79+}$	100.0	15.9 weeks	258 $\mu\text{b}^{-1}$	—	
	$^{197}\text{Au}^{79+} + ^{197}\text{Au}^{79+}$ polarized p + p	9.8 100.2	2 shifts <small>8.3 weeks total, no continuous physics operation</small>	0.4 $\mu\text{b}^{-1}$ 1.4 $\text{pb}^{-1}$	— 14%	
<b>Run-3</b> CY2002/03, FY2003 30.4 cryo-weeks	d + $^{197}\text{Au}^{79+}$	100.7 + 100.0	10.2 weeks	73 $\text{nb}^{-1}$	—	
	polarized p + p	100.2	<small>9.0 weeks total, no continuous physics operation</small>	5.5 $\text{pb}^{-1}$	34%	
<b>Run-4</b> CY2003/04, FY2004 26.7 cryo-weeks	$^{197}\text{Au}^{79+} + ^{197}\text{Au}^{79+}$	100.0	12.0 weeks	3.53 $\text{nb}^{-1}$	—	
	$^{197}\text{Au}^{79+} + ^{197}\text{Au}^{79+}$ polarized p + p	31.2 100.2	9 days <small>6.1 weeks total, no continuous physics operation</small>	67 $\mu\text{b}^{-1}$ 7.1 $\text{pb}^{-1}$	— 46%	
<b>Run-5</b> CY2004/05, FY2005 31.4 cryo-weeks	$^{63}\text{Cu}^{29+} + ^{63}\text{Cu}^{29+}$	100.0	7.8 weeks	42.1 $\text{nb}^{-1}$	—	
	$^{63}\text{Cu}^{29+} + ^{63}\text{Cu}^{29+}$ polarized p + p	31.2 100.2	12 days 5 shifts	1.5 $\text{nb}^{-1}$ 0.02 $\text{nb}^{-1}$	— —	
<b>Run-6</b> CY2006, FY2006 21.2 cryo-weeks	$^{63}\text{Cu}^{29+} + ^{63}\text{Cu}^{29+}$ polarized p + p	11.2 204.9 100.2	9.4 weeks 2 stores	29.5 $\text{pb}^{-1}$ 0.1 $\text{pb}^{-1}$	47% 30%	
	polarized p + p	31.2	13.1 weeks	88.6 $\text{pb}^{-1}$	55%	

Figure 4.2: Runs 1 - 3 at RHIC focused on commissioning work for experiments measuring collisions at RHIC. Work was mostly characterized by heavy-ion measurements related to understanding Quark-Gluon Plasma. The spin program began with Run 5. Table produced from data posted at the RHIC run page [16].

RHIC operating modes and total integrated luminosity delivered to 6 experiments					
Run	species	total particle energy [GeV/nucleon]	calendar time in physics	total delivered luminosity	average store polarization, (H-jet)*
<b>Run-7</b> CY2006/07, FY2006 18.4 cryo-weeks	$^{197}\text{Au}^{79+} + ^{197}\text{Au}^{79+}$	100.0	12.8 weeks	7.25 nb <sup>-1</sup>	—
	$^{197}\text{Au}^{79+} + ^{197}\text{Au}^{79+}$	4.6	3 shifts total, no continous physicsoperation	small	—
<b>Run-8</b> CY2007/08, FY2008 19.0 cryo-weeks	d + $^{197}\text{Au}^{79+}$	100.7 + 100.0	9.0 weeks	437 nb <sup>-1</sup>	—
	polarized p + p	100.2	3.4 weeks	38.4 pb <sup>-1</sup>	44%
	$^{197}\text{Au}^{79+} + ^{197}\text{Au}^{79+}$	4.6	3 shifts	small	—
<b>Run-9</b> CY2008/09, FY2009 22.0 cryo-weeks	polarized p + p	249.9	4.1 weeks	110 pb <sup>-1</sup>	34%
	polarized p + p	100.2	9.9 weeks	114 pb <sup>-1</sup>	56%
	polarized pp2pp	100.2	3.5 days	0.6 nb <sup>-1</sup>	63%
	$^{197}\text{Au}^{79+} + ^{197}\text{Au}^{79+}$	100.0	10.9 weeks	10.3 nb <sup>-1</sup>	—
	$^{197}\text{Au}^{79+} + ^{197}\text{Au}^{79+}$	31.2	2.9 weeks	544 μb <sup>-1</sup>	—
<b>Run-10</b> CY2009/10, FY2010 27.1 cryo-weeks	$^{197}\text{Au}^{79+} + ^{197}\text{Au}^{79+}$	19.5	1.8 weeks	206 μb <sup>-1</sup>	—
	$^{197}\text{Au}^{79+} + ^{197}\text{Au}^{79+}$	3.85	4.6 weeks	4.23 μb <sup>-1</sup>	—
	$^{197}\text{Au}^{79+} + ^{197}\text{Au}^{79+}$	5.75	1.4 weeks	7.8 μb <sup>-1</sup>	—
	polarized p + p	249.9	9.7 weeks	166 pb <sup>-1</sup>	48%
	$^{197}\text{Au}^{79+} + ^{197}\text{Au}^{79+}$	9.8	1.4 weeks	33.2 μb <sup>-1</sup>	—
<b>Run-11</b> CY2010/11, FY2011 24.4 cryo-weeks	$^{197}\text{Au}^{79+} + ^{197}\text{Au}^{79+}$	100.0	6.4 weeks	9.79 nb <sup>-1</sup>	—
	$^{197}\text{Au}^{79+} + ^{197}\text{Au}^{79+}$	13.5	8 days	63.1 μb <sup>-1</sup>	—
	polarized p + p	100.2	4.4 weeks	74.0 pb <sup>-1</sup>	59%
<b>Run-12</b> CY2011/12, FY2012 22.9 cryo-weeks	polarized p + p	254.9	4.9 weeks	283 pb <sup>-1</sup>	52%
	$^{238}\text{U}^{92+} + ^{238}\text{U}^{92+}$	96.4	3.1 weeks	736 μb <sup>-1</sup>	—
	$^{63}\text{Cu}^{29+} + ^{197}\text{Au}^{79+}$	99.9 + 100.0	5.4 weeks	27.0 nb <sup>-1</sup>	—
<b>Run-13</b> CY2012/13, FY2013 17.0 cryo-weeks	polarized p + p	254.9	13.3 weeks	1.04 fb <sup>-1</sup>	53%

Figure 4.3: Though RHIC is currently still running (as of May 9, 2016), I include runs here up to and including the run producing my data set (Run 13). An unprecedented 13.3 cryo-weeks of running was awarded to the W-Physics group. Table produced from data posted at the RHIC run page [16].

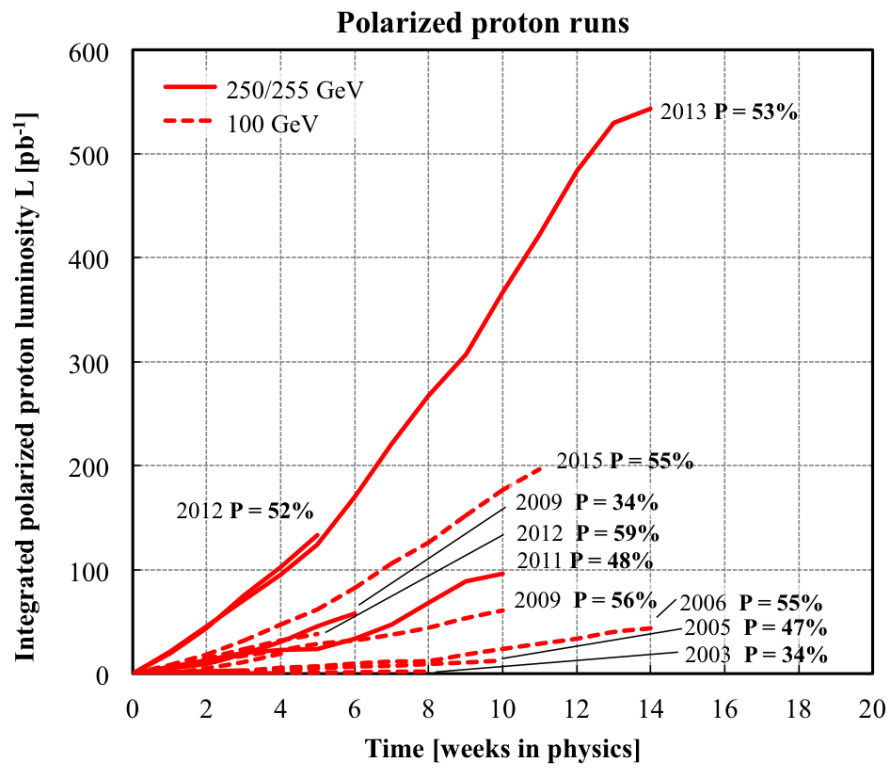


Figure 4.4: Upgrades to RHIC's electron lens have enabled massive improvements to luminosity - seen in the year 2013. The high luminosity was taken advantage of with an extra long proton+proton run. Figure obtained from [16]

#### 4.1.1 Experimental Apparatus

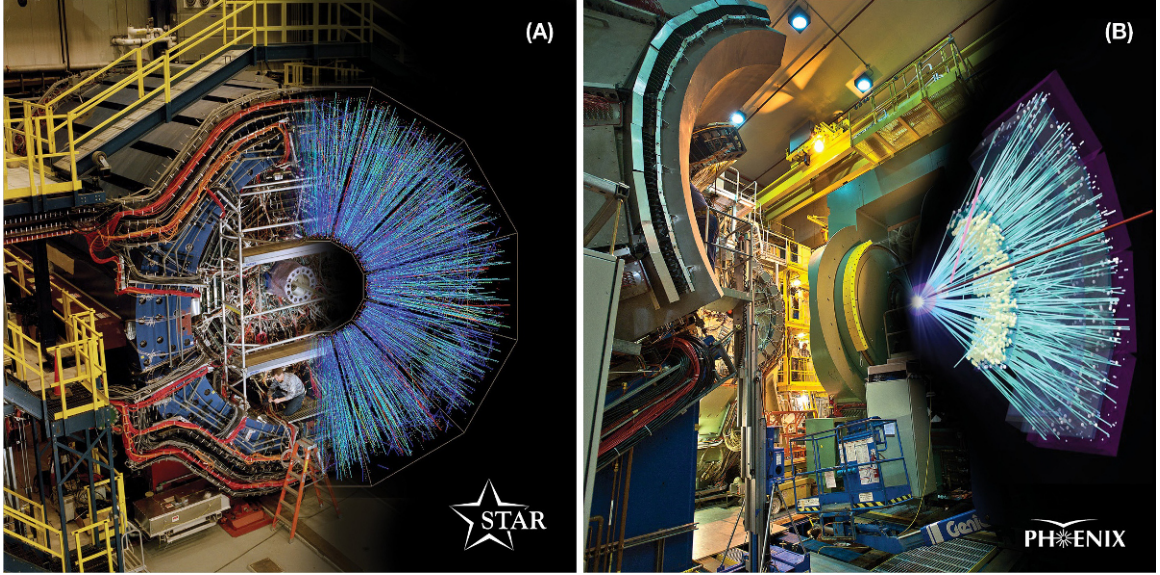


Figure 4.5: STAR (a) and PHENIX (b) with cutaways showing the event display for a heavy-ion collision as reconstructed by the detectors' electromagnetic calorimeters [17].

RHIC accelerates ions in a multi-stage process, summarized in Figure 4.1. The first stop is the **Electron Beam Ion Source**, built on top of a  $200\text{MeV}$  linear accelerator (Linac). Once ions are injected into the Linac, they travel to the *Booster Synchrotron*. At this stage, ions are accelerated with pulsed RF fields. Once the beam of ions has been accelerated to nearly the speed of light, they are fed into the **Alternating Gradient Synchrotron** or AGS. At this time, ions are traveling at about  $0.37 c$ . By the time the ions leave the AGS, they are moving at  $0.997 c$ . Once the ions are ready, they are transferred to the **AGS-to-RHIC Line**, where a switching magnet pumps bunches of ions into either the counterclockwise circulating ring of RHIC, or the clockwise circulating ring of RHIC. The ions are 'spun-up' here to maximum speed, and are accelerated around the RHIC complex - each beam-ion travels nearly 2.4 miles in microseconds, for the duration of a physics-fill [64].

When the RHIC rings are filled with ions, the ions are bunched into rotating electromagnetic potentials called 'buckets'. There are 360 beam-buckets in total, but typically only a fraction are filled with ions. For this analysis, we took data with beams with 110 filled buckets. The sequence of beam buckets from one bunch to the next is referred to as a

'bunch' - and are rather long - Figure 4.6. A detailed presentation of beam dynamics with regards to luminosity will be presented in chapter 8.

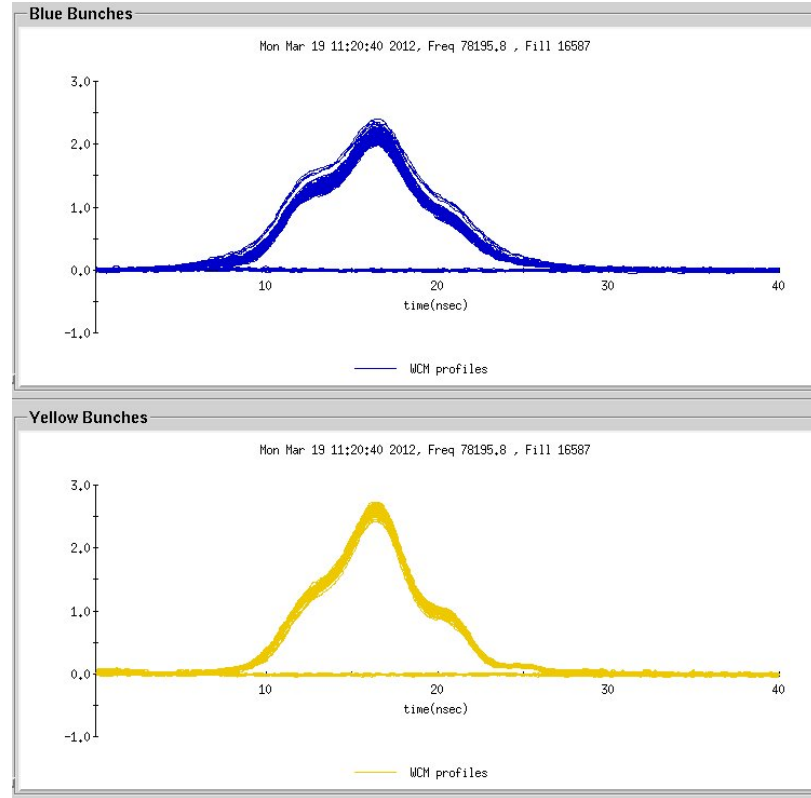


Figure 4.6: Plot courtesy of Angelika Drees, of RHIC's Collider-Accelerator department. The blue beam (blue) and yellow beam (yellow) are overlaid over a 40 nanosecond time period. Even with bunches crossing a fixed point over 40 nanoseconds, this still corresponds to an overall bunch length of about 12 meters. Conversely, the bunch width is quite narrow - with Gaussian geometry, it is between 150 millimeters and 300 millimeters depending on the beam energy. Understanding the beam bunch geometry is a crucial component to understanding total the total luminosity delivered by RHIC to PHENIX.

## 4.2 Production of Polarized Proton Beams

The production of polarized beams is crucial to the physics of this measurement - without polarized beams, no spin structure analysis can be done at RHIC. This is due to the fact that the helicity state of the protons in the initial state of any proton proton collision can be connected to the final observed states in a way which provides information about the spin structure function, as was discussed in section 3.

The production of polarized beams is a multistage process, and involves several experimental components. The importance of polarizing the beams is fully realized once polarized beams are collided at relatively high center of mass energies - where the beams behave less like polarized proton beams, but more like polarized beams of quarks and gluons [65]. Beam polarization is achieved incrementally - with polarization starting as soon as the booster and AGS stage of the acceleration process 4.1.

The RHIC Configuration Manual [19] provides a wealth of information, accelerator physics, diagrams, equations, and descriptions of the extremely precise and comprehensive approach to creating polarized proton beams and injecting them into RHIC. This work was crucial to this section of my thesis, and is recommended reading for anyone who wishes to know 'all the details' of how RHIC handles polarized beams.

### 4.2.1 Polarized Injection

RHIC uses an optically pumped polarized ion source (OPPIS), Figure 4.7 to produce a polarized ion source greatly in excess of RHIC's design intensity. This is used to our advantage, as the emittance of the beam can be lowered to create a highly collimated beam for physics use.

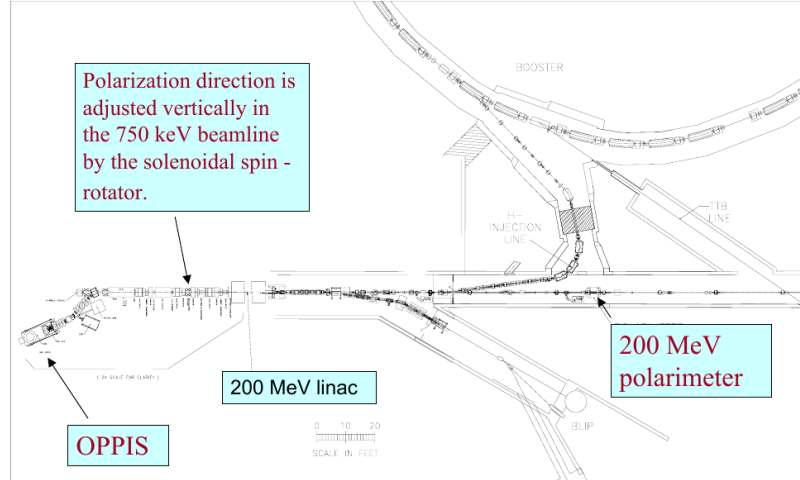


Figure 4.7: RHIC's optically pumped polarized ion source. Produces 0.5-1.0 mA current of polarized  $H^-$  ions. The optical pumping is pulsed at 400  $\mu s$ , [18]

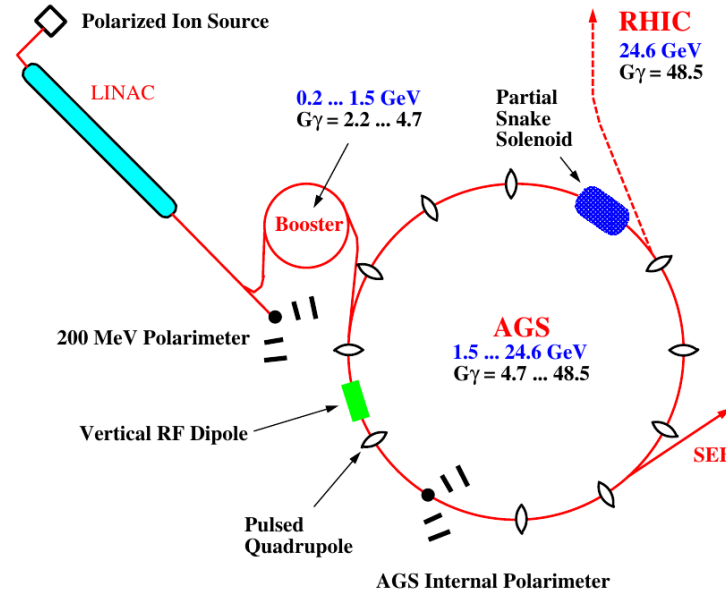
#### 4.2.2 AGS to RHIC Transfer Line

Once ions have been optically pumped, we have a direct-current beam at approximately 80% polarization. The pumping is accomplished using Rubidium vapor. The polarized ions are then moved into the booster from the Linac, where some polarization is lost to spin precession, intrinsic to accelerating charged ions in a circular path. However, polarization is maintained, for the most part, by matching the precession resonance to the orbiting frequency of the booster ring. The Siberian snakes and spin rotators at this stage serve to incrementally flip the ion spin such that the natural depolarization works to re-polarize the orbiting ions, every full-turn. The full details of this procedure are well described in [19].

After the ions are sufficiently polarized and filled in the AGS, they are moved into the AGS to RHIC Transfer line, Figure 4.9. The beam is focused and fed through a switching magnet - which must be timed with great precision in order to fill the blue and yellow beams with the appropriate polarization patterns. In fact, the precision is so great, that the earth's curvature must be taken into account over this relatively short injection line - the entry point and exit point are bent ever so slightly different - the entry being 12.51 mrad, vs the egress being 12.46 mrad [19]. At the point of injection in the transfer line, the beam size and emittance are measured, as well as the beam polarization.



(a) Technical schematic of Polarized Injection Line [18]



(b) Overhead view of Polarized Injection Line [19]

Figure 4.8: A view of the RHIC polarized injection system. We see a zoomed in technical view of the OPPIS to the booster (a), below, we see a zoomed out cartoon of the next step in the polarization injection system, including the AGS, and the feeder line to RHIC.

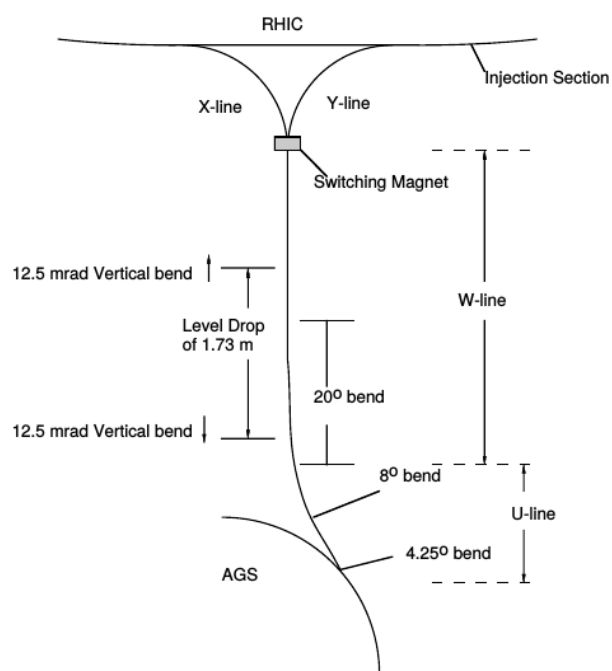


Figure 4.9: A schematic of the geometry of the AGS-to-RHIC transfer line [19].

## 4.3 Maintaining Beam Polarization

The creation of polarized beams is only half the battle. Depolarizing resonances in any particle beam are intrinsic in the design of any circulating beam particle accelerator - without intervention, after a few rotations, RHIC's polarized beams would be unpolarized. RHIC uses several strategies in concert to correct for the largest of these depolarizing resonances - including beam orbit corrections, the Siberian Snakes, Betatron Tune Spreading, and sextupole magnetic depolarizing resonances.

### 4.3.1 Siberian Snakes and Spin Rotators

The Siberian Snakes are positioned at two locations on the RHIC ring (as well as others along the injection sequence). The most stable configuration of spin injected in RHIC is such that the spin axis is perpendicular to the plane of the accelerator ring. The Siberian snake is a helical magnet which forces the spin to rotate 180 degrees every half rotation. This special configuration of snakes (see Figure 4.1) ingeniously takes advantage of the rotational precision of the spin (a depolarizing resonance) to re-polarize the beam, every half-orbit.

The spin rotators are located outside of experimental interaction regions around PHENIX and STAR. These special dipole magnets rotate the spin of the beams onto a longitudinal (parallel with beam) axis - these magnets are important for any measurement (such as this one) requiring longitudinal spin polarization. Otherwise, transverse spin effects can by studied.

### 4.3.2 Measuring Beam Polarization

The RHIC Collider-Accelerator Department provides several means of measuring the beam polarization over the course of the data taking period. PHENIX takes special data and studies it, to determine the real beam polarization delivered to the detector, in a yearly analysis (for years where polarized data is taken). This analysis is often called "Local Polarimetry", but is often abbreviated as LPol in PHENIX logs.

CAD will additionally measure polarization in via inelastic proton-carbon scattering in the Coulomb-Nuclear Interference (CNI) region. Relative polarization can be determined with to within 10% in only a few seconds of measurement.



Figure 4.10: As beams are longitudinally rotated into position for collision, it is crucial to keep careful track of the magnet currents rotating the beams, as well as the overall polarization pattern. Shown is a cartoon of one potential polarization pattern.

Vertical polarization is determined through the calculation of the left and right particle production, with a known analyzing power ([19], Ch 8):

$$P_B = \frac{1}{A_p} \frac{N_L - N_R}{N_L + N_R} \quad (4.1)$$

Where  $P_B$  is the beam polarization,  $N_L$  and  $N_R$  are the left-scattering produced particles, and right-scattering produced particles and  $A_p$  is the analyzing power, which can be calculated from first principals, and experimentally verified. Scattering takes place as a carbon filament is swept across the beam.

As many decisions are financially constrained, this one was too. Using a p-Carbon CNI polarimeter provides an economically viable way to measure beam polarization within the precision needed for the spin experiments.

#### 4.3.2.1 The Spin Monitor

One of my major contributions to the PHENIX experiment was in the upkeep and development of the spin monitoring systems for the online data taking portions of the experiment.

During a RHIC run, it is crucial to keep track of the polarization patterns being collided at the PHENIX IR 4.10

The spin monitor was composed of tens of thousands of lines of code, and was quite a monstrosity to keep running, however, I managed it. I contributed better error logging, and helped to facilitate a total rewrite of the software, to create more understandable and reliable output. However, in the interim, I reprogrammed the monitor to handle spin patterns, and provide the shift crew at PHENIX with immediate feedback regarding the

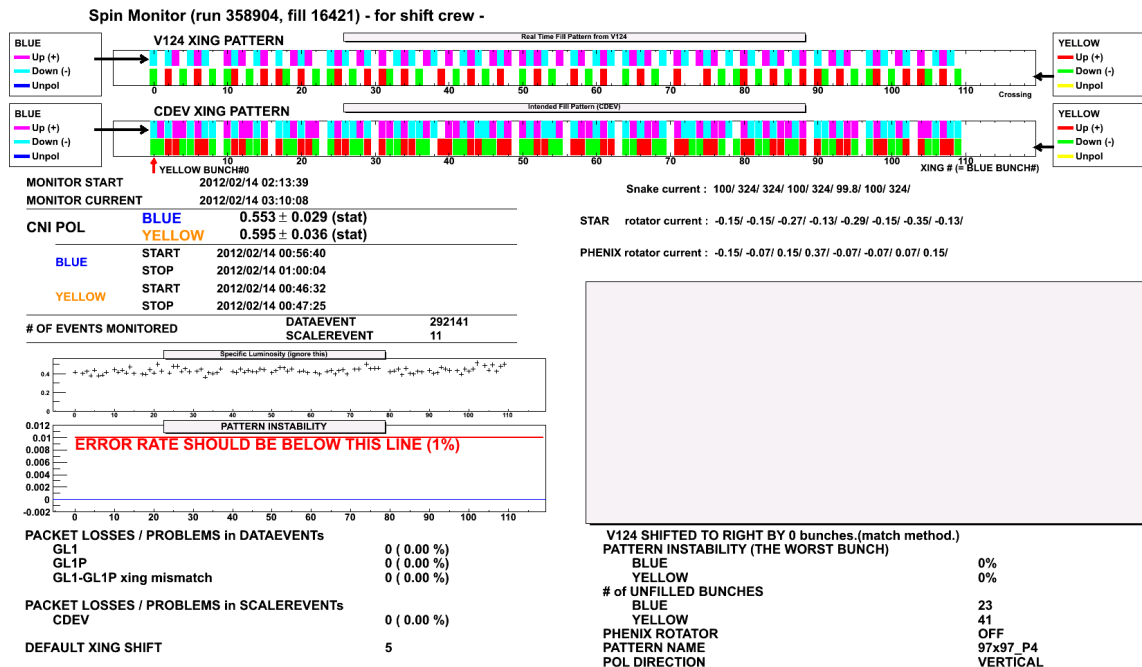


Figure 4.11: The shift-crew display output for the Spin Monitor. The upper panel shows the polarization of the blue and yellow beams, and other panels summarize information including magnet currents (needed to understand the spin orientation), issues with data packet loss, the recognized spin-pattern, as well as a large boxed area on the lower left where errors could be shown to the shift crew along with the proper response.

spin-quality of the live data, Figure 4.11

## 4.4 The Pioneering High Energy Nuclear Interaction Experiment

### 4.4.1 Overview

The Pioneering High Energy Nuclear Interaction Experiment is a synthesis of many smaller detectors all of whom were commissioned for various physics goals, some of which have been repurposed from their original application once the primary physics mission of the detectors were completed.

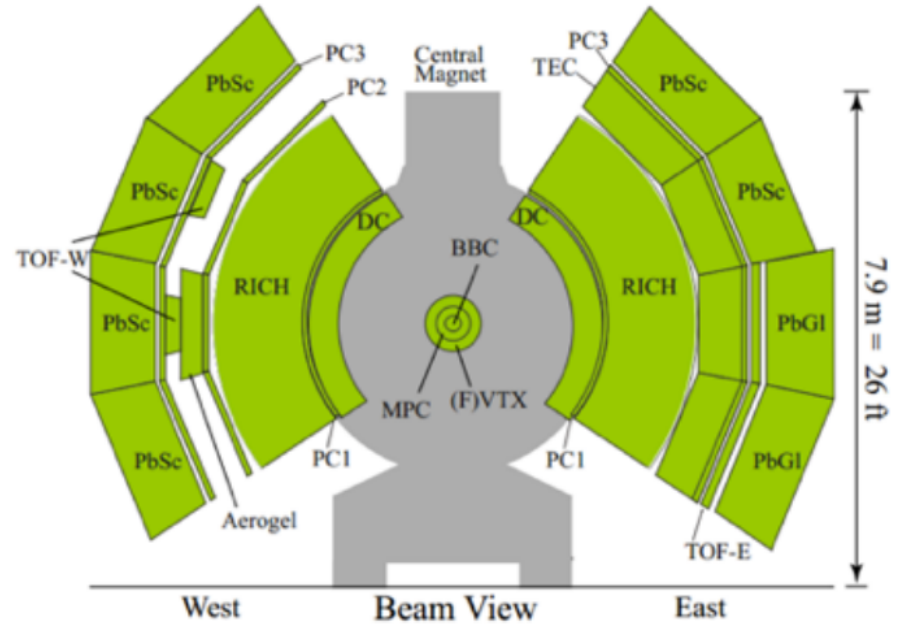
The configuration of the PHENIX spectrometer can be changed from year to year, depending on the analysis needs of the physics working groups. The configuration of the detector for the 2013 physics run is shown in Figure 4.12.

PHENIX makes use of many classic detector technologies, it contains Čerenkov light detectors, resistive plate chambers, electromagnetic calorimeters, silicon chip detectors, time of flight detectors, scintillation light detectors, cathode strip chambers, and proportional tube counters.

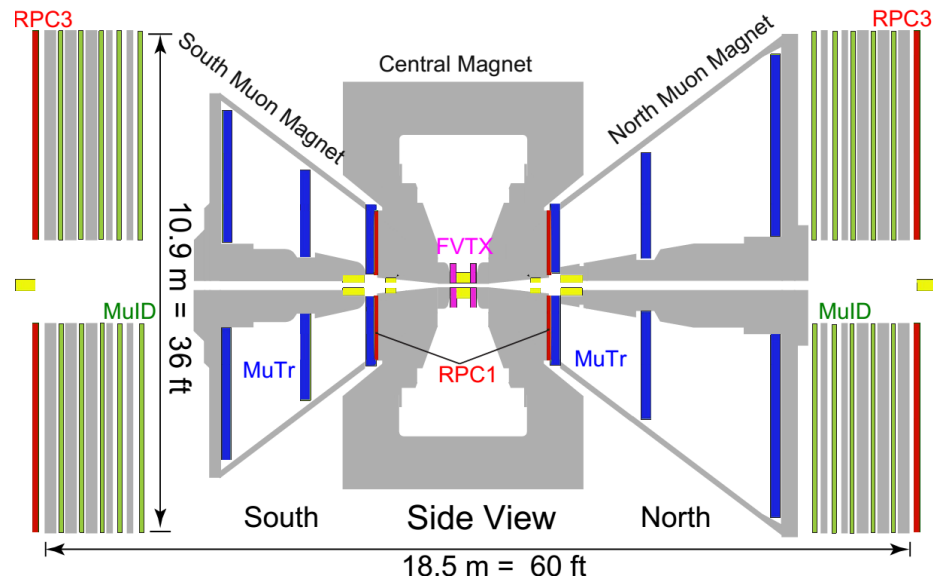
While all of these subsystems are interesting, and have produced excellent physics results, I will focus only on those pertinent to this analysis.

PHENIX is generally thought of as two 'halves', which often are used in separate analyses - the forward muon arms, and the central arms. While both halves are used for both heavy ion, and spin physics analyses, this analysis exclusively uses the forward muon arms, so the central arms will not be discussed (though, a closely related analysis, dealing with  $A_L$  for  $W \rightarrow e$  exclusively uses the central arms). The different subsystems cover different rapidity ranges, so many times, complimentary results are obtained from central and forward analysis. Results from such a complementary central analysis will be presented alongside my results in later chapters.

PHENIX also utilizes a complex data acquisition system (DAQ) which streams data from each detector, assembles this data into a labeled event, compresses and stores into a proprietary storage format, the work-flow of this is summarized in Figure 4.13. A complete summary of PHENIX detector subsystems (excluding the Forward Vertex Detector, Silicon Vertex Detector, and Resistive Plate Chambers, which are new, and discussed separately)



(a) Central Arms



(b) Forward Muon Arms

Figure 4.12: Shown: The two main halves of the PHENIX Spectrometer. The central arms are shown via the beam-on view of PHENIX (left) and Forward Muon Arms are shown via the 90-degree rotated view. In both cases, the 2013 configuration is shown. The beams are brought into intersection at the geometric center of each figure (immediately between the BBCs)

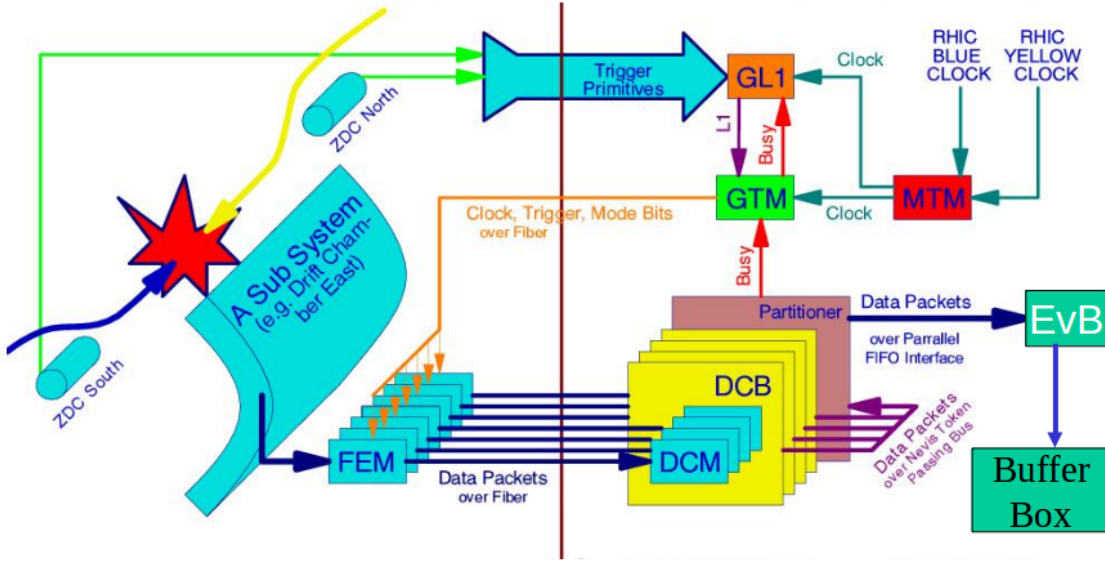


Figure 4.13: A flow chart summarizing the PHENIX DAQ [20]. From left to right, we can get a feel for the data flow at PHENIX. Shown is an event, the red splat on the far left. Particles from this event are transduced by a detector ('A Sub System'). The transduced signals are serialized into a detector specific data stream, such that the state of the detector's excitation can be recorded and reproduced later. This information is stored on the front-end-electronics modules (FEMs), and synchronized with timing information from the clock (ticks once every time there is a bunch crossing) and a Global Trigger decision, i.e. whether or not the right parts of the detector lit up to make this particular event worth keeping. After this, if the event is designed by the heuristics to be worthy of keeping, the uncompressed serialized information is sent to the DCMs, where it is assembled into a packet, and then sent to the event builder (EvB), where all packets sharing a common collision are assembled into an event. The event is compressed into a proprietary PRDF format, and sent to the Buffer Boxes, which are a cache of high density local storage, which is later sent off to cold storage on magnetic tape drives.

<b>Element</b>	$\Delta\eta$	$\Delta\phi$	<b>Features</b>
<b>Magnets</b>			
Central Magent	$\pm 0.35$	$360^\circ$	$1.15 \text{ T}$
Muon Magnet North	$-1.1 - -2.2$	$360^\circ$	$0.72 \text{ T}$
Muon Magnet South	$1.1 - 2.4$	$360^\circ$	$0.72 \text{ T}$
<b>Minimum Bias</b>			
Beam Beam Counter	$\pm(3.1 - 3.9)$	$360^\circ$	Vertex Reconstruction
Zero Degree Calorimeter	$\pm 2\text{mrad}$	$360^\circ$	Minimum Bias Trigger
<b>Central Detectors</b>			
Drift Chambers	$\pm 0.35$	$90^\circ \times 2$	Central $p$ and $m$ resolution
Pad Chambers	$\pm 0.35$	$90^\circ \times 2$	Pattern Recognition, Tracking
Ring Imaging Čerenkov	$\pm 0.35$	$90^\circ \times 2$	Electron ID
Time of Flight	$\pm 0.35$	$45^\circ$	Hadron ID, $\sigma < 100\text{pm}$
PbSc EMCal	$\pm 0.35$	$90^\circ \text{--} 45^\circ$	Calorimetry, photon and electron energy
PbGl EMCal	$\pm 0.35$	$45^\circ$	$e^\pm, \mu^\pm$ separation at $p > 1\text{GeV}/c$ , EM Shower and $p < 0.35\text{GeV}$ , $K^\pm, \pi^\pm$ separation up to $1\text{GeV}/c$
<b>Muon Arms</b>			
Muon Tracker South	-1.15 to -2.25	$360^\circ$	North installed 2003
Muon Tracker North	1.15 to 2.44	$360^\circ$	
Muon ID South	-1.15 to -2.25	$360^\circ$	Steel absorbers, larocci tubes
Muon ID North	1.15 to 2.44	$360^\circ$	""

Table 4.1: A summary of PHENIX hardware [28]. Electron/pion separation and Pion/Kaon separation requires the Time of Flight (ToF) working with PbGl and PbSc data. PbGl refers to "Lead Glass Scintillator" and PbSc refers to "Lead Scintillator". The Muon Identifier (Muon ID, MuID) can help separate muons from hadrons.

can by found in Table 4.1.

#### 4.4.2 The Spin Program

The PHENIX spin program was planned as part of the RHIC upgrade to produce polarized proton beams. The major analysis thrust of the PHENIX spin program has been to understand the spin structure of the proton, and has historically used various flavors of particle production asymmetries (left-right and forward-backward) as an experimental probe for polarized parton distribution functions (as we saw in Chapter 3).

Much of PHENIX collaboration's early published work focused on creating and studying quark gluon plasma in heavy ion collisions, but in following years spin papers came too. Major question in physics that PHENIX set out to answer with its heavy-ion program include studying confinement - i.e. why are quark color charges confined to exist in the nucleus, baryons and mesons? PHENIX sought to study this via examination of the  $J/\Psi$  and measuring screening length in heavy ion collisions. Additional research topics included the study of chiral symmetry restoration, thermal radiation of hot gasses, QCD Phase transition, Strangeness and Charm Production, Jet Quenching, and Space-time evolution [66].

The spin program came shortly after the 2001 commissioning run. The first polarized proton run was produced by RHIC for PHENIX in 2002, with 8.3 total weeks of data, run discontinuously. The primary goals of the PHENIX spin program are to study the polarization of the proton, specifically in the context of the Ellis-Jaffe sum rule, which decomposes the proton spin into various contributions from its substructure. The main structures studied by PHENIX are the gluon polarization,  $\Delta g$  and the anti-quark polarization,  $\Delta \bar{q}$ . Additionally, the 'nature of parity non-conservation itself can be directly studied' using polarized beams, and spin asymmetries in collisions. Though this measurement generally requires a means of reconstructing jets (PHENIX doesn't have this), inclusive or leading particle production can be used as a substitute with some small asymmetry remaining [67].

#### 4.4.3 Subsystems

The major subsystems contributing to this work include the Muon Arms, the Beam Beam Counters (BBCs), and the Forward Vertex Detector, since the analysis is totally characterized with calculating the  $A_L$  for  $W \rightarrow \mu$  interactions, only muon reconstruction

and identification is required. The Central arms are used in the  $W \rightarrow e$  analysis.

#### 4.4.3.1 Beam Beam Counters

The Beam-Beam counters (BBCs, Figure 4.14) are photomultiplier tubes with scintillating lead-glass crystals. These detectors are situated about 144 cm on either side of the nominal center of the PHENIX interaction region, and typically are used to trigger on events with minimal bias towards any particular physics goal. This is important as a means for reconstructing the relative abundance of particle production, which is as you might expect, crucial for determination of any inelastic scattering cross section. The Beam-Beam counters provide us with vertex reconstruction by way of analyzing the time delay between triggering of the North BBC and the South BBC. The delay window is then used to reconstruct the event vertex by assuming particles are travelling at near light speed, Figure 4.15.

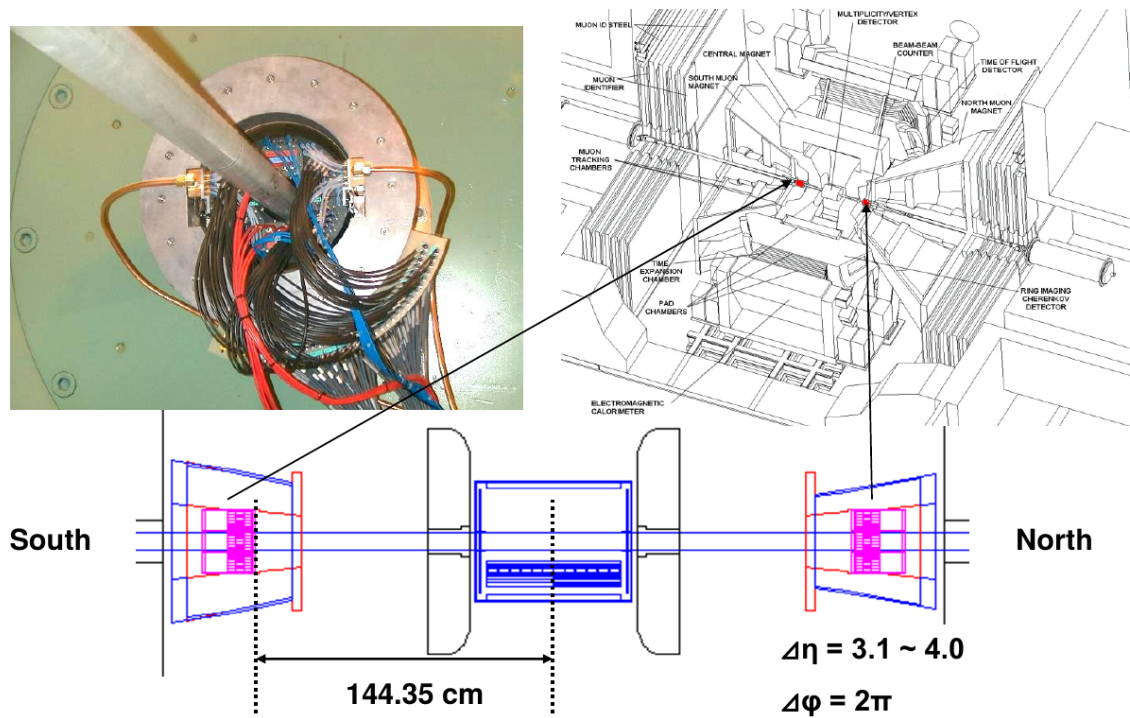


Figure 4.14: Shown: a photograph of the BBC hugging the beryllium beam pipe near the center of PHENIX (top left), a schematic showing the relative size and location of the BBCs as compared to the rest of PHENIX (top right), and a schematic of the exact proportions of the detector as viewed alongside the beam pipe (bottom), along with the rapidity and azimuthal coverage [21]

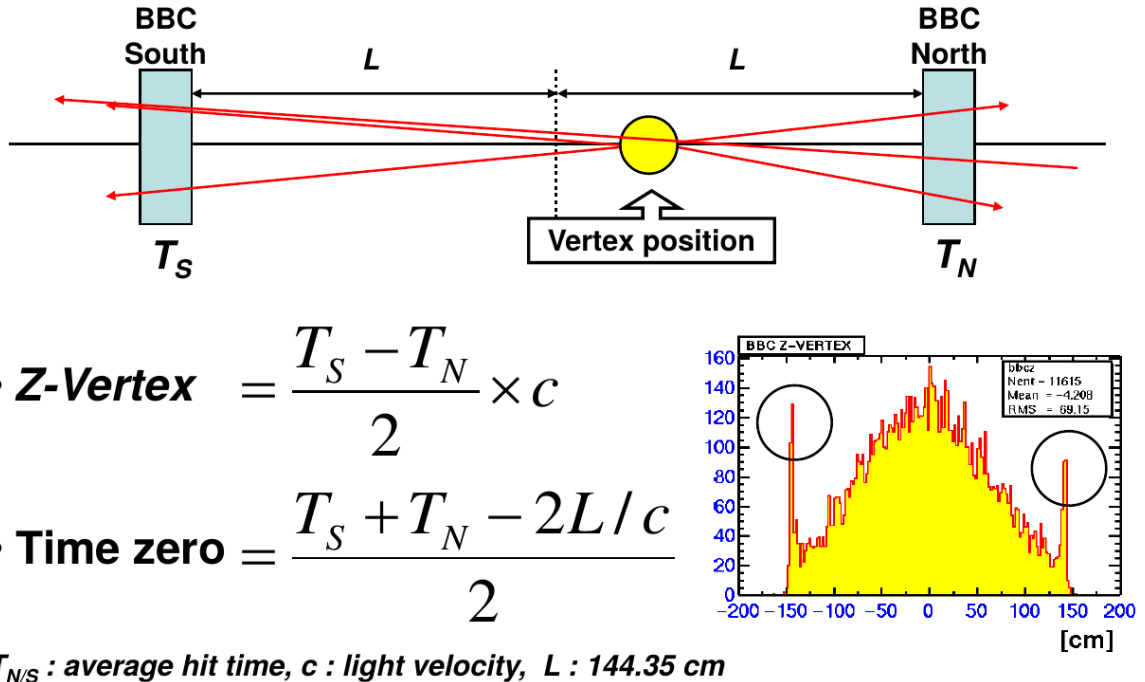


Figure 4.15: A diagram outlining the strategy for reconstructing the event z-vertex of a collision. Top: a cartoon of the North and South BBCs getting some particle penetration after an event. Bottom Right: a characteristic distribution of measured z-vertices for a short run taken in 2002 [21].

#### 4.4.3.2 Forward Vertex Detector

The Forward Vertex Detector, Figure 4.16 is a silicon detector, which provides additional tracking to detect secondary event vertices and additional precision to the Muon Tracking system. This detector can provide an important additional layer of precision, because it can help to identify events which do not originate from the primary event vertex of a collision, so they can be rejected from a pool of candidate  $W \rightarrow \mu$  events [22]. The properties of this detector are summarized in Table 4.2

Property	Value
Silicon sensor thickness ( $\mu\text{m}$ )	320
Strip pitch ( $\mu\text{m}$ )	75
Nominal operating sensor bias (V)	+70
Strips per column for small, large wedges	640, 1664
Inner radius of silicon (mm)	44.0
Strip columns per half-disk (2 per wedge)	48
Mean z-position of four stations (mm)	201.1, 261.4, 321.7, 382.0
Silicon mean z offsets from station center (mm)	5.845, 9.845

Table 4.2: A brief summary of the FVTX design parameters [22]

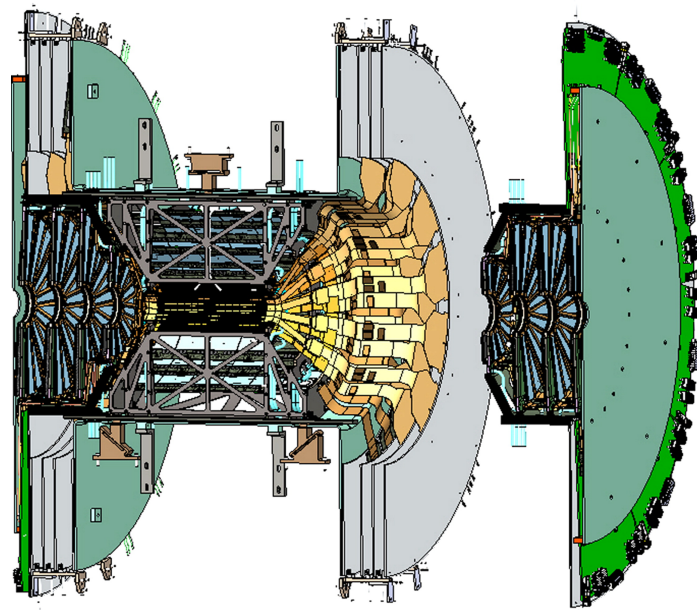


Figure 4.16: A schematic of the Forward Vertex Detector, showing the silicon chip layers (light blue wedges), and readout electronics (green). They are mounted directly onto the Silicon Vertex Detector, which was not used in this analysis. The FVTX and SVD together are used in heavy ion analyses [22].

#### 4.4.3.3 The Muon Arms

The Muon Arms are composed of several subsystems, including the Muon Tracker (MuTR, cathode strip chambers), the Muon Identifier (MuID, shielding and scintillation layers), and the Resistive Plate Chambers (RPC(s), bakelite gas gaps and azimuthal oriented capacitively coupled copper readout strips). The job of the muon tracker is to identify muons with the penetration through the many layers of the MuID, and provide momentum and charge reconstruction for muon tracks. Tracks are matched to the event vertex with Kalman filter during reconstruction, and can even be matched with FVTX secondary vertices as a means of rejecting non W-Boson decays. Prior to the Forward Upgrade (Section 4.5), the muon arms consisted solely of the Muon Tracker and the MuID.

The Muon Tracker has a radial magnetic field, leading to charged particles traversing the tracker to have a helical bend. This was suitable for lower energy muon tracks, such as muons coming from the  $J\Psi$  decay, which was one of the primary decays targeted in the original design of the muon tracker.

However, these  $J/\Psi$  muons have much lower energy than muons which decay from areal W-Boson production. To extend the muon tracker's usefulness into tracking these high energy muons, an upgrade to the triggering system was required to obtain adequate back-ground rejection for the Forward W analysis. The details of the muon arms will be discussed in the next section.

## 4.5 The Forward Upgrade

The muon arms were the subject of significant upgrades from 2011-2013. New front end electronics were added to improve triggering, and entire new detector subsystems (The RPCs) were added. The full details of these subsystems will be discussed in the forthcoming sections (Section 4.5).

One of the main stated physics goals of PHENIX is to constrain the sea-quark polarization of the proton spin. While this contribution is expected to be small, it is not because it is expected to be uniformly zero. Instead, the expectation is that the matter contribution to the quark sea is strongly positively polarized, while the antimatter contribution is strongly negatively polarized [15]. Measuring this polarization via  $A_L$  (Equation 3.4) is the means by which we will accomplish this. Prior to the Forward Upgrade, we only had results from the Central  $W \rightarrow \mu$  analysis, but to better constrain our models, we require lower uncertainty in the forward kinematic regime - thus, the Forward Upgrade.

The first data for this measurement was taken in 2009, and published in 2010 under [68] and [69], but only for central rapidities, where a clear Jacobean peak could be found in the electron invariant mass spectrum at  $40\text{GeV}$  mass-energy (half the rest mass of the W-Boson). This made evaluating yields and calculating asymmetries relatively straight-forward.

However, in forward kinematic regimes, it was very difficult to discriminate real  $W \rightarrow \mu$  from other sources  $X \rightarrow \mu$ . As one can observe in Figure 4.17, only at high  $p_T$  does the W-boson signal become dominant. The old muon trigger electronics did not allow triggering sufficiently close to the W-Boson production threshold to allow for enough data to be taken. This is because of how the Muon Tracker identifies the charge and momentum of particles - which is via track bending. As tracks become very straight (i.e. high  $p_T$ ), the muon tracker struggles to reconstruct the correct charge and momentum. The original Forward Upgrade called for a nose-cone calorimeter, which would have helped greatly for particle rejection, but was canned for budget reasons.

The Forward Upgrade to PHENIX increased the muon triggering threshold from about  $2\text{ GeV}$  to  $10\text{ GeV}$ , enough to insure that all muons produced from W-Boson decays can be recorded, with no loss of statistics. This of course is not to say, that these events were recorded without any background processes - the removal of the muon background was

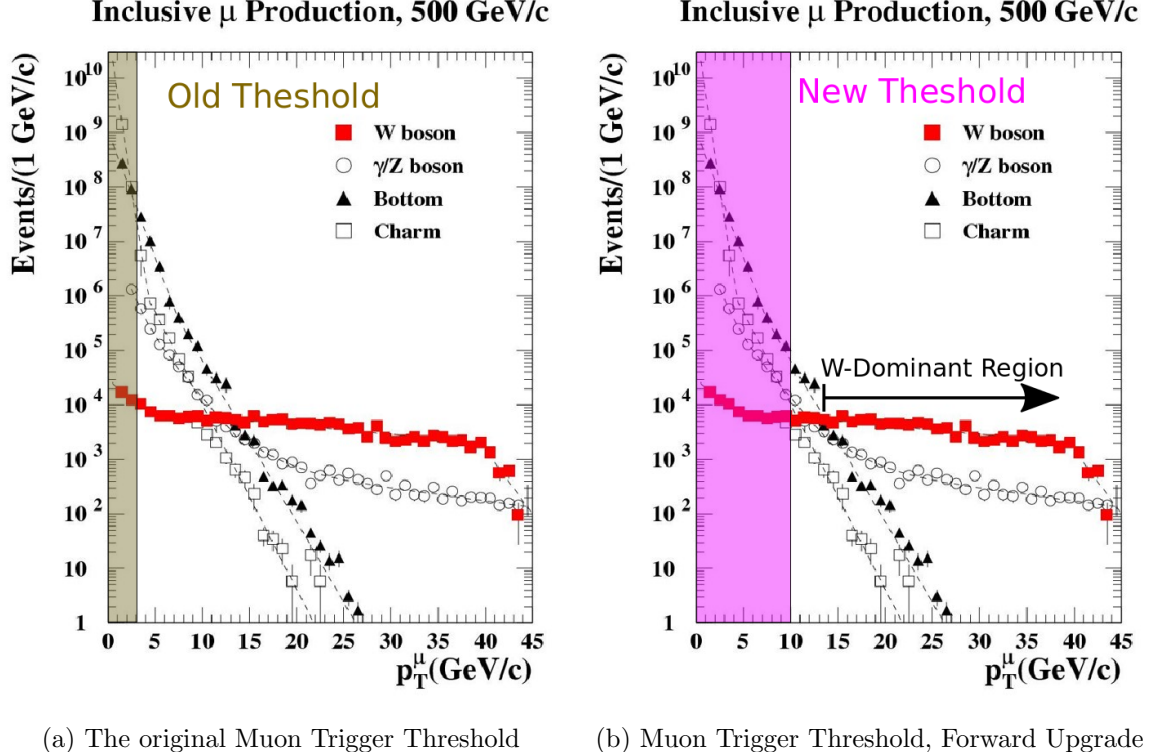


Figure 4.17: Observing the simulated production of muon as a function of  $p_T$ , we can see that in the kinematic region of  $W$  production that the dominant sources of muons come from other processes. The new PHENIX muon trigger threshold is sensitive at 10  $GeV/c$  and above. The threshold is still high enough that with other methods, we can record all events which come from the  $W$  boson, with triggering, whereas with the old threshold, this was impossible.

a substantial effort in this analysis, described in Section 6.4.

#### 4.5.1 The Muon Tracker

The primary purpose of the Muon Tracker is to reconstruct the energy and momentum of muons in the forward kinematic regime. Because the MuID is composed of larocci tubes sandwiched between solid steel sheets, only particles which penetrate all the layers of the MuID are identified as muons. The Muon Tracker has three cathode strip tracking planes in a volume of gas, with an applied radial magnetic field. Each plane has two faces of tracking strips, for six total tracking readouts total. The arrangement of cathode strips

makes the Muon Tracker very sensitive to the azimuthal dimension, but coarsely sensitive to the radial direction. The Muon Arms have three tracking stations for momentum and charge identification, sandwiched between two RPCS.

Since the MuID will fire on Muons with a  $2.5\text{ GeV}$  momentum threshold, it will trigger very rapidly at high beam energies and luminosities - too fast to record all data - event rates were in excess of 10 MHz in 2013, with only 2 kHz of DAQ bandwidth allocated to the W analysis. Thus, before the Forward Upgrade, the Muon Arms were insufficient. However, additional absorber was installed at the nose-cone of the muon tracker to block lower momentum particles. The addition of the RPCs as well as new Front End Electronics Modules allowed for the real-time calculation of pseudo-momentum to be fed into the trigger decision in order to provide high rejection power on tracks. These upgrades allowed us to trigger exclusively on relatively straight tracks, which is consistent with high momentum particles [23].

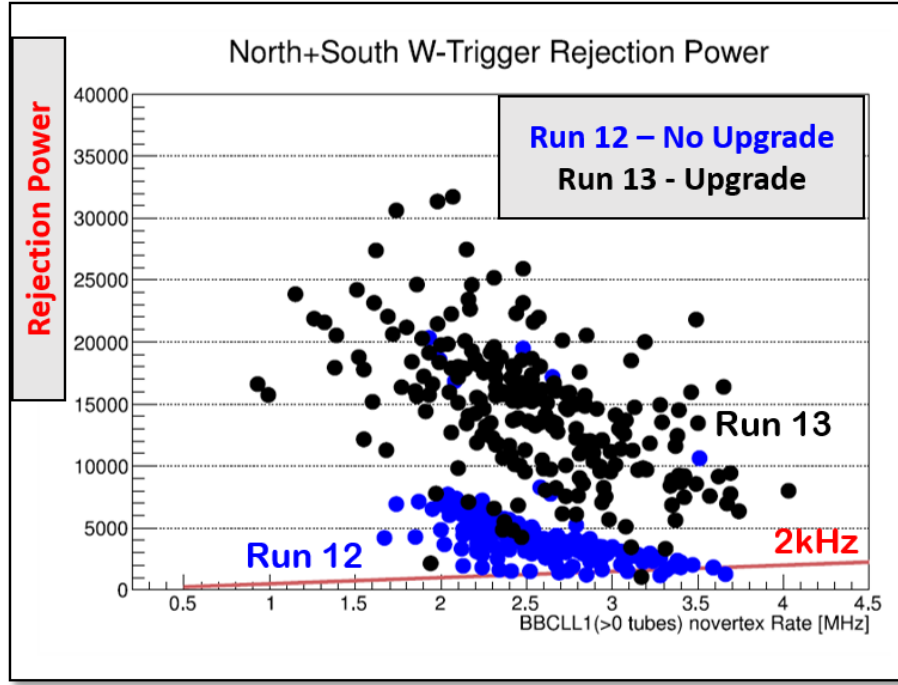
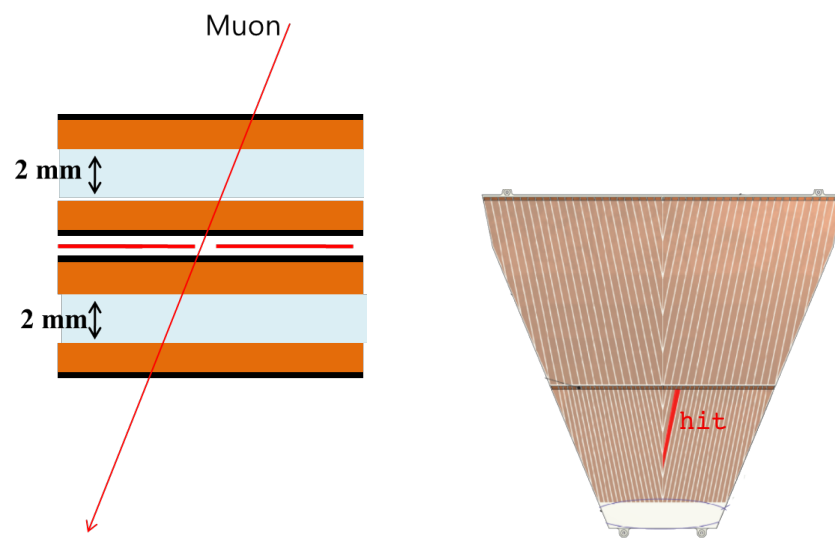


Figure 4.18: In 2013 with the final commissioning of the RPCs and the Forward Upgrade complete, we saw a drastic increase in rejection power, as planned.

#### 4.5.2 The Resistive Plate Chambers

One of my major contributions to the PHENIX experiment was in the construction and testing of the RPCs at station 1, in 2012. An exploded view of the RPC is shown in Figure 4.20. The RPCs were a crucial part of the W-Physics muon trigger. One primary feature the presence of RPCs add to the PHENIX triggering system is timing resolution - 2 nanoseconds (Table 4.3). This is crucial, because before the inclusion of RPCs, the only timing available was that of the BBCs. However - because the BBCs are minimally biased - they will fire nearly every time there is a collision - which at high luminosity is far greater than the assigned bandwidth to the W Physics trigger. The RPC provides local timing information, which allows the triggering system to record events which trigger the muon arm system, and not just the BBCs. This has the effect of significantly reducing backgrounds - by a factor of > 6000 [23], Figure 4.18.



(a) A muon passing through the layers of the RPC (left), the gas in the bakelite gap is ionized. This charge migrates and collects near the highly resistive graphite coating. An image distribution is induced on the overlapping readout strip (right), which is passed along its own channel to the front-end electronics.

Figure 4.19: As a muon passes through the layers of the RPC (left), the gas in the bakelite gap is ionized. This charge migrates and collects near the highly resistive graphite coating. An image distribution is induced on the overlapping readout strip (right), which is passed along its own channel to the front-end electronics.

#### 4.5.2.1 Design

As hinted at prior, the design goal of the Resistive Plate Chambers is to provide accurate timing information at high speed in order to build a Trigger which can record  $W \rightarrow \mu$  events. RPCs were first implemented at the Large Hadron Collider at CERN, and their design has been adopted for use at PHENIX both because of its high speed, and low cost. In Figure 4.20 the basic design is shown - the means of signal transduction is via ionizing of gas inside a highly resistive chamber. The chamber is held at a large bias - at 8.5 kilovolts, such that any ionization will collect on the interior of the resistive chamber in a fixed, and relatively static distribution in time (relative to time scales of triggering system timing, in millionths of a second). This charge distribution is read out by capacitively coupled copper readout strips, into fast electronics (Figure 4.19). The design requirements of PHENIX is that when triggered, 2 or fewer clusters (strips) are activated, the efficiency of the detector must be at least 95%, the time resolution must be at least 2 nanoseconds, with a particle transduction rate of 500 Hz per square centimeter. These properties are summarized in Table 4.3 [23].

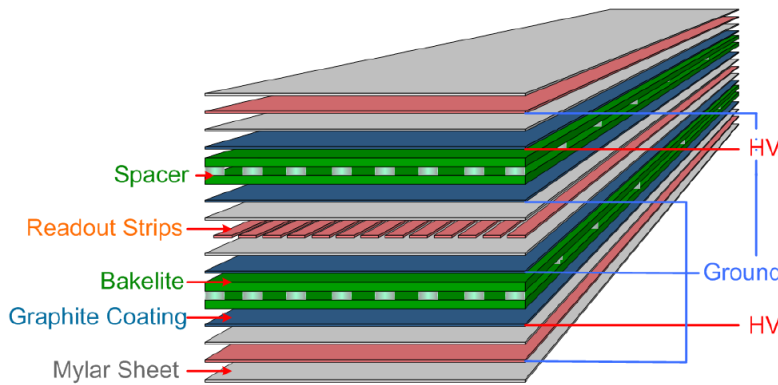


Figure 4.20: We can see the various layers that go into the construction of a typical RPC segment installed at PHENIX. A High Voltage bias is applied to the graphite coating on either side of bakelite gas-filled gaps. Readout strips are positioned between the two bakelite gaps. Finally, the entire double-gap structure is surrounded by a copper grounding cage, and wrapped in insulating mylar [23].

---

<b>Cluster Size</b>	<2 strips
<b>Efficiency</b>	>95% for MIP
<b>Time Resolution</b>	~2 nanoseconds
<b>Rate Capability</b>	0.5 kHz/cm <sup>2</sup>

---

Table 4.3: The design characteristics of the RPCs [23]

#### 4.5.2.2 Construction and Testing

Construction of the Resistive Plate Chambers took place in two stages over several years. Fabrication of the bakelite gas gaps was done overseas in Korea, and the aluminum chassis was manufactured in China. Pieces for the RPC 3 and RPC 1 were shipped to Brookhaven National Laboratory where they were assembled and tested, before being installed. The installation occurred over two years, with the first stage, the RPC 3, being installed in 2011, and the second stage, the RPC 1, being installed in 2012. After being fully commissioned, the capstone data set for W-Physics was taken in 2013, which is discussed in detail in Chapter 5.

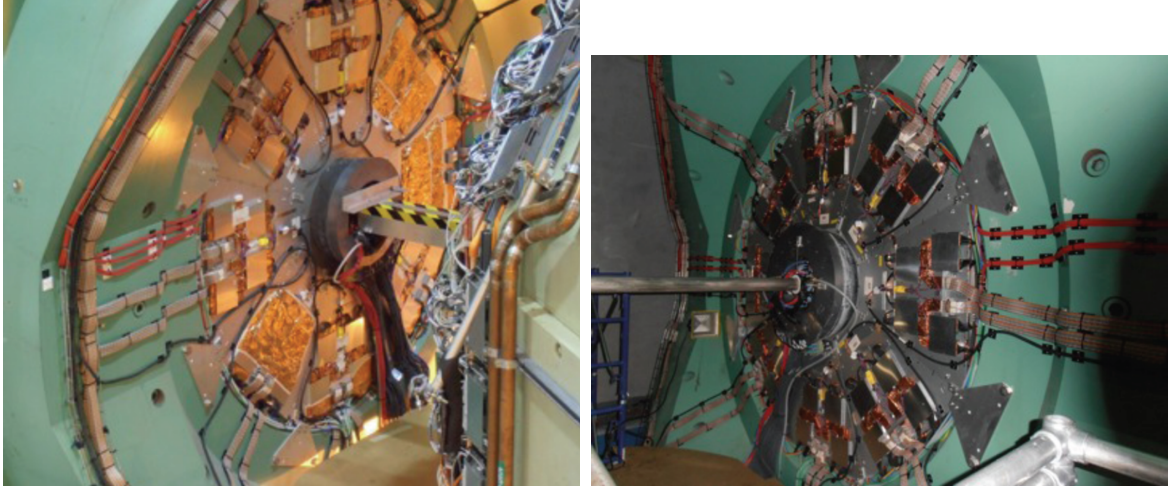
The RPC 3 and RPC 1 construction efforts took place in a special clean-room built inside of the cavernous building 9-12 (Figure 4.21) at Brookhaven National Lab. Construction was overseen by Dr. Francesca Giordano, working as a post doctoral associate for Dr. Matthias Grosse Perdekamp for the University of Illinois at Urbana Champagne. The electronics of the RPCs were funded by professors Ken Barish and Rich Seto at the University of California, Riverside, via a grant from the Department of Energy. I am very grateful for Francesca for her guidance and trust, as she allowed me to construct and test many of these octants. I constructed the gaps with Arbin Timilsina, who was a very entertaining and helpful lab-mate. Ihnjei Choi and Young Jin Kim were instrumental in the design, construction, and QA of the RPCs as well.

The RPCs are modular in design - the larger RPC 3 North and South were separated into 16 half octants, whereas the smaller RPC 1 North and South were separated into eight octants. Both North and South RPCs have the same full azimuthal coverage, but due to the differing size of the Muon Arms, they have different rapidity coverage.

The RPC 1 octants were installed directly on the nose-cone of the Muon Tracker, shown in Figure 4.22. Unlike to the RPC 3, the RPC 1 North and South are quite compact,



Figure 4.21: Two special tents inside building 912 at Brookhaven National Laboratory, built to house completed RPC octants and the laboratory used to construct and test the octants.



(a) RPC Station 1, North

(b) RPC Station 1, South

Figure 4.22: The North RPC Station 1 is installed on the muon tracker nosecone (left). Similarly we see the installation of the south RPC Station 1 (right). The metal tube in the center is the beryllium beam pipe.

and are the exact same size 4.23.

Each RPC1 octant was hand assembled, with components being tested at each stage of the construction, where relevant. The first stage of construction involved preparing the machined aluminum chassis. Mylar sheets were cut to fit the chassis baseplate, and secured to the aluminum with Kapton tape - chosen for robustness over high ranges of temperature, as well as good electrical insulating properties. The chassis itself is not one machined piece, but is bolted together with machine screws 4.24. The chassis is cleaned several times during the assembly process with methanol to remove any remaining machining debris.

Double-sided tape is then added to the mylar sheeting, and special foam is then placed down. Sections are removed from the foam to accommodate routing of the electrical hookup for setting the Bakelite gas-gaps to a high bias, Figure ??.

After the chassis has been prepared, the bakelite gas gaps are assembled. The gas gap itself (Figure 4.26, Figure 4.20), is composed of two layers of Bakelite, which are separated by small insulating spacers. On the outside, the Bakelite is coated with graphite



Figure 4.23: Here, we see one of the many hard-working physicists who tirelessly worked in building 911: a dusty, and irradiated construct built along the AGS beam-line. The physicist sits in the center of the RPC1 North chassis, for scale. More information can be found in [24].

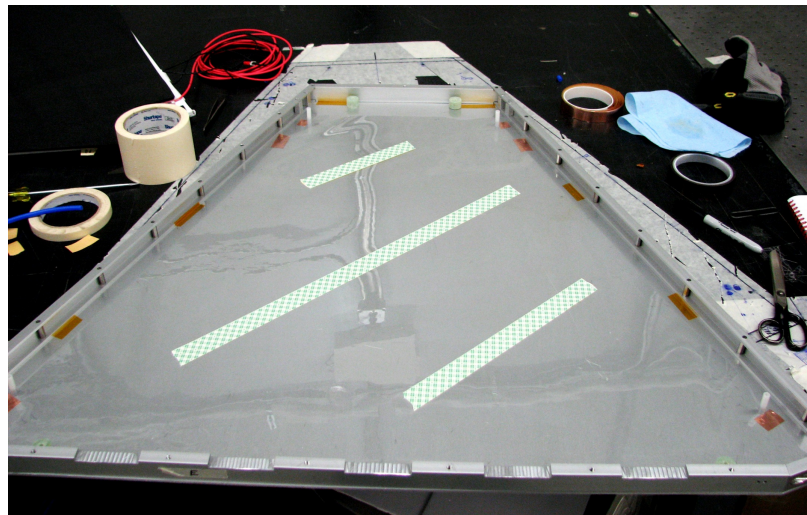


Figure 4.24: The chassis is prepared with insulating Kapton tape and mylar sheeting. The grooves along the bottom of the chassis are for routing cabling from the readout strips (shown later). The channels along the side of the chassis is for routing gas flow lines.

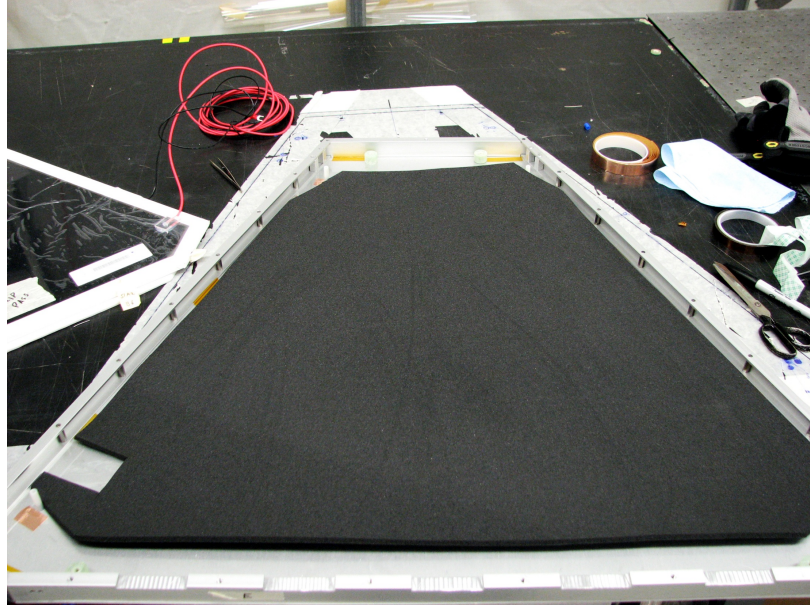


Figure 4.25: Foam shock insulation is added to the RPC 1 chassis.

suspended in linseed oil to produce outer surfaces that can be held at a fixed voltage bias. The separation of the plates forms a chamber, which is sealed from the outside. Electrodes are attached to the linseed oil to allow for bias, and plastic nipples are routed into the gap chamber allowing for gas flow. Tubes are cut to size and fixed to the gas chamber nipples, and then routed out down to the widest end. These gas feed tubes are color coded - a different color for each Bakelite section in the RPC. These gas gaps are leak/pop tested in the lab. This test involved pressurizing the gaps to 8.5 inches of water, and measuring pressure loss over a ten minute interval, using Argon. Pressure losses less than 1 inch was acceptable. During pressurization, I checked for an audible pop sound, which indicated one of the gap spacers popping lose. Popping noises, or bad pressure retention would both result in the gas gap being discarded. Finally, before installing the gap, the gap was 'burnt in', a process where the gaps were filled with the 'physics gas mixture' and then slowly voltage cycled to operating voltage over 24 hours.

After the bakelite gas gaps are tested and have passed, they are installed into the chassis, Figure 4.27. The chassis is prepared for installation with the addition of a layer of copper foil, to create a Faraday cage around the sensitive bakelite gaps. Tabs are left on the copper foil, such that they can be folded around the inner gaps, but not around the gas

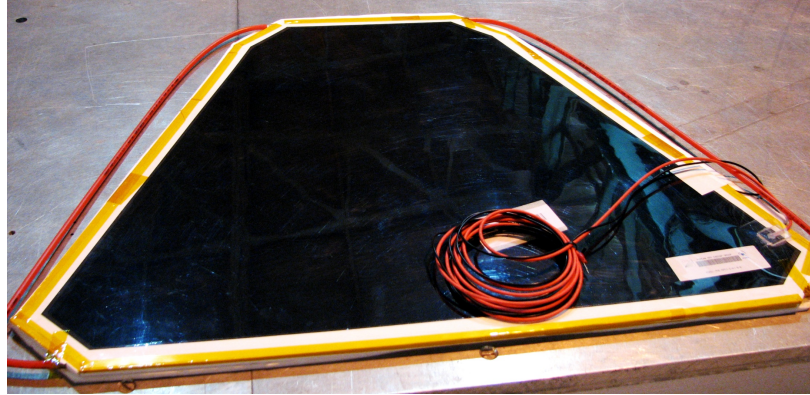


Figure 4.26: The assembled Bakelite gas gap, ready for leak/pop testing, followed by burn in.

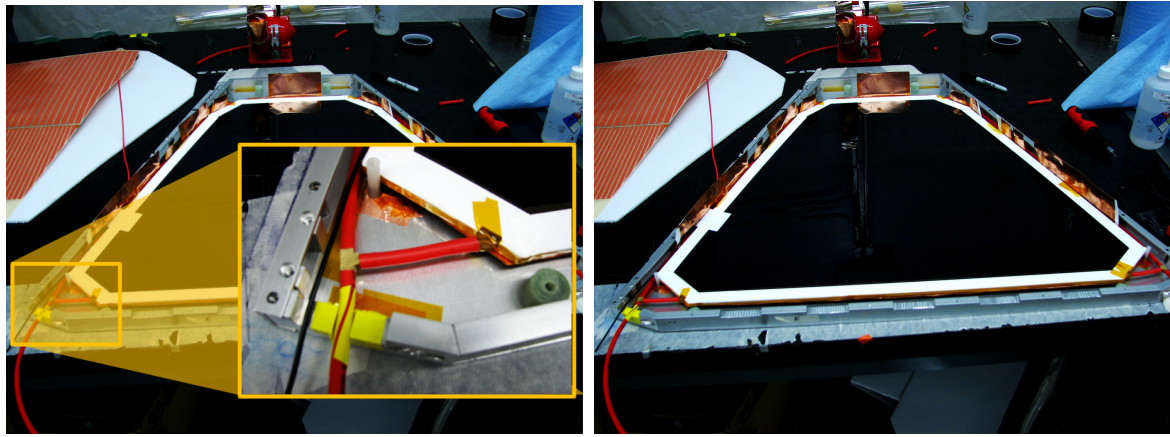
lines. The bias cables and gas lines are routed through the chassis side channels.

Once the bottom gas gap has been installed and secured, the copper readout strips are added, Figure 4.28. The strips are oriented such that two annuli of readout strips are created (azimuthally) when the RPC 1 is installed onto the nose cone of the muon trackers. The readout strips are designed this way as to offer some rough radial tracking. The copper readout strips are laminated with mylar, and each is soldered to its own channel, which are gathered and soldered onto PCB chips. The readout strips are laminated such that mounting holes in the laminate attach in the same way to each octant, for consistency.

Following the installation of the readout strips, the final two gas gaps are installed, with their electronics and gas lines routed through the chassis similarly to the bottom gap, Figure 4.29.

Finally, the high voltage cables are grounded to the chassis and soldered to the relevant wires leading to the graphite electrodes on the outside of the Bakelite gas gaps. Wires, tubes, etc. are all fixed in place with Kaptan tape. The top of the chassis is screwed into place, and the front-end electronics are installed, with the copper readout chips plugging into the relevant FEM board. Ribbon cables are appropriately routed, and all electronics are encased in copper foil, and then additionally protected with aluminum shells, Figure 4.30.

After assembly, the RPCs were subjected to a barrage of tests, using a cosmic



(a) Routing gas line

(b) Gas gap installed

Figure 4.27: The egress port of the gas gap is carefully shielded with tape to prevent friction from causing tears, and routed out of the ports machined into the bottom of the chassis (right), with the final position of the first gap shown on the left.

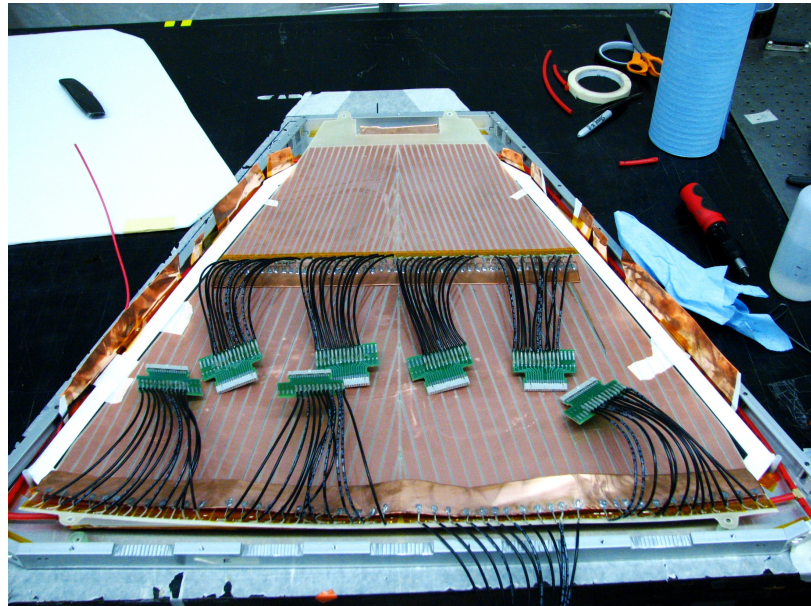
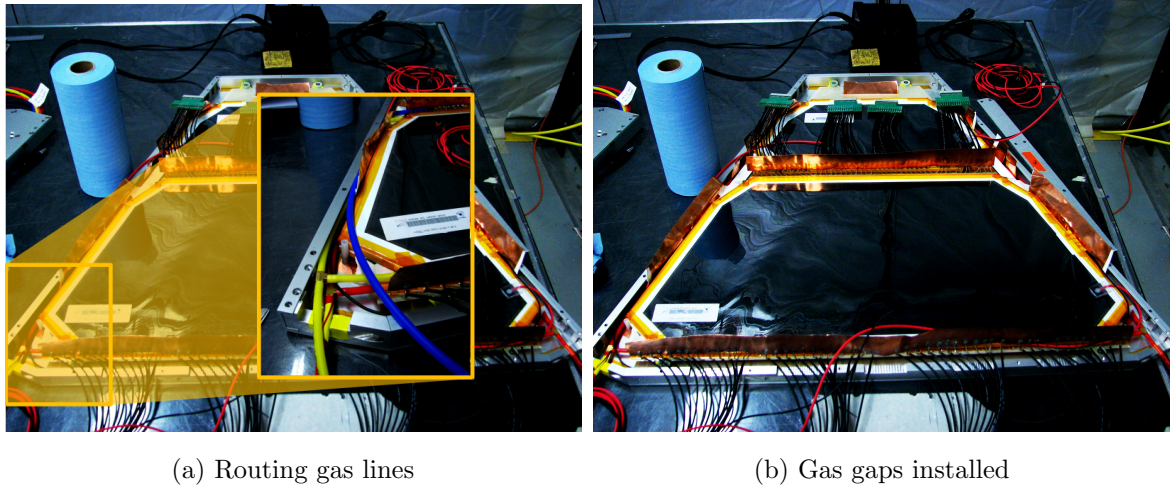


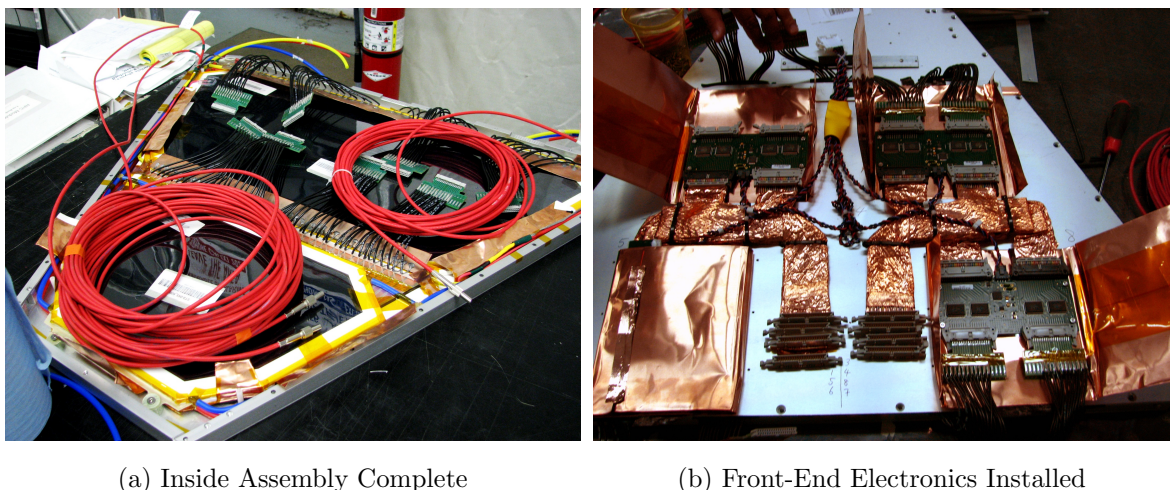
Figure 4.28: The copper readout strips are mounted to the chassis. Each readout strip is soldered to a copper wire, which in turn are gathered into readout chips.



(a) Routing gas lines

(b) Gas gaps installed

Figure 4.29: The final Bakelite gas gaps are installed on top of the copper readout strips. Gas lines are routed similarly to 4.27



(a) Inside Assembly Complete

(b) Front-End Electronics Installed

Figure 4.30: A completed RPC 1 octant, interior assembly complete, left, and the outer assembly completed on the right.

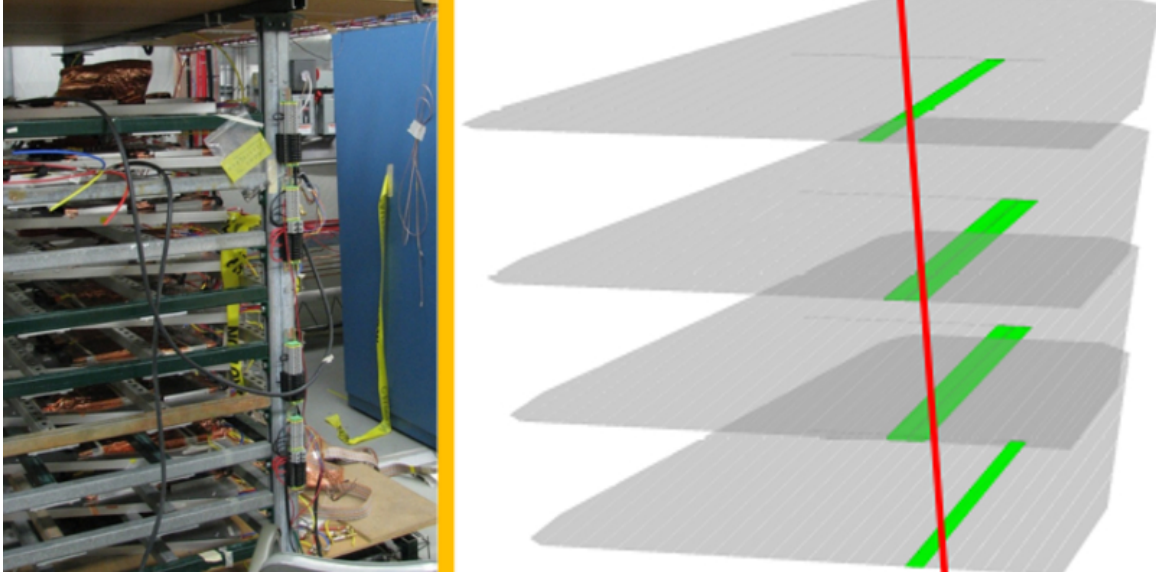


Figure 4.31: Left: the cosmic test stand setup. RPC octants were sandwiched between scintillators to run performance and efficiency tests. An example of the clustering due to a cosmic ray is shown on the right, with a particle (red) activating one or two strips per octant (activation shown in green).

ray test stand to measure clustering (Figure 4.31), designed to measure the activation threshold (combined with energy readings from scintillators above and below the test stand), determine the average cluster size, and measure overall detector efficiency. The overall ohmic ‘dark-current’ was also measured.

#### 4.5.2.3 Performance

With the construction and installation of the RPCs and new Front End Electronics for the Muon Tracker, PHENIX was ready to take data for the W measurement by 2013. A dedicated run was taken, accumulating over  $200\text{pb}^{-1}$  of data. All tolerances and design specifications for the upgrade were met.

#### 4.5.3 Triggering and Data Acquisition

The new triggering scheme incorporating the RPCs and the new FEEs is summarized in Figure 4.32, while the final configuration of the PHENIX detector after the forward

upgrade is shown in Figure 4.33. As discussed, data was recorded at about 30% of the total PHENIX DAQ bandwidth of 8 kHz over the 2013 polarized proton+proton run, which was sufficient to record every single  $W \rightarrow \mu$  event. This speaks to the relative rarity of this event, as compared to other events - the overall collision rate for protons at  $510\text{GeV}/c^2$  is as high as 10 MHz.

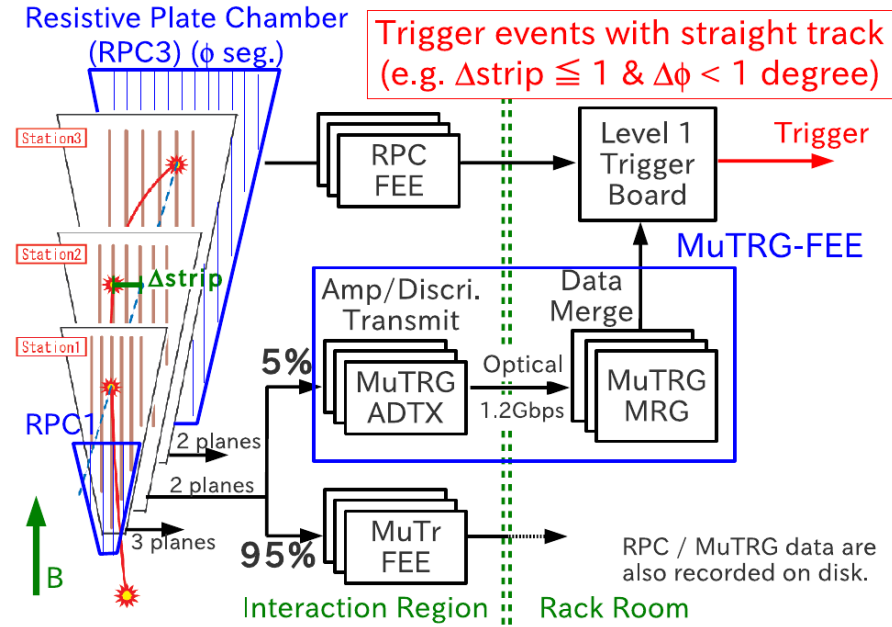


Figure 4.32: A schematic of the new muon trigger for recording W-Bosons [23]

#### 4.5.3.1 2013 Data Set Triggers

In general, when two protons inelastically interact, we do not care about the particles that are produced because they simply tell us about physics which we already understand. To learn about new physics, or to test models, we must devise a way to preferentially record this 'interesting' data, since data recording bandwidth is limited. A decision must be made within the time scale of one beam crossing (nanoseconds) whether or not to archive the data which is produced. This process is called 'triggering'. The overall trigger rates must be recorded, so as to reconstruct the relative abundance of events after the fact. Once a trigger condition has been satisfied, the entire PHENIX spectrometer will

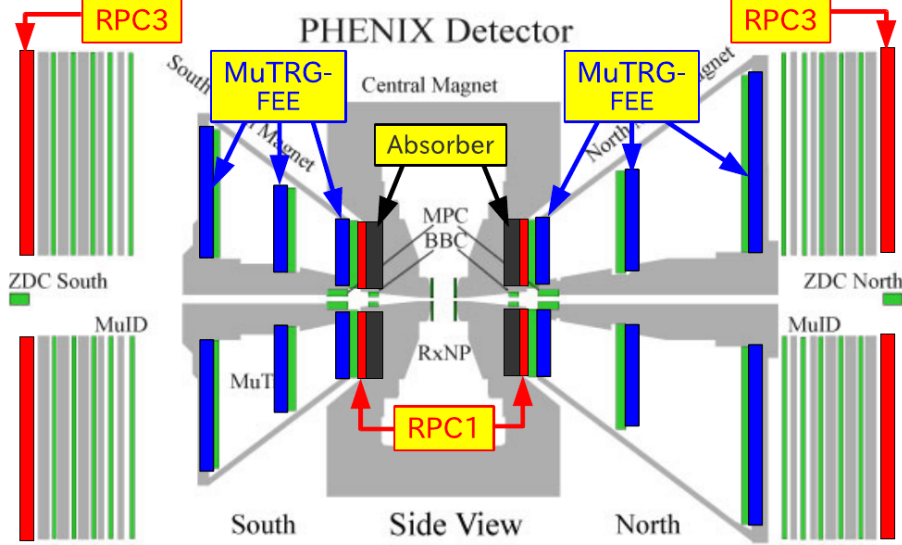


Figure 4.33: The position of the Front-End Electronics upgrades and new RPCs + Absorber are shown. Muon tracker stations are shown in blue (along with the front-end electronics). The RPCs sandwich the muon tracking stations and the MuID. The absorber material sits just inside of the muon arms, before the Forward Vertex Detectors and inner tracking stations of the muon tracker [23]

dump its data into the data stream.

The PHENIX DAQ can accommodate 32 different physics triggers. Any transduced signal by a part of the PHENIX spectrometer can be, provided the front end electronics are fast enough, be fed into a global triggering decision. Thus, PHENIX, like other triggered particle physics experiments can be arbitrarily configured to record a desired subset of data, from the total data set.

Of the 32 triggers available, one is always set to 'Noise' (but not recorded) and another is set to 'CLOCK' which is timed to trigger every beam crossing. No bandwidth is reserved for these triggers. There was one global physics trigger configuration used in the Run 13 data set, it was called 'PP510Run13'. An example configuration is shown in Table ??.

The each physics trigger is conveniently stored as a 32-bit integer. This is a very special integer, because it does not take on all possible values that a 32-bit integer can take on. A trigger with a bitnumber of '2' means that the second binary digit of the trigger's

Name	Scale Down	Raw Trigger Rate	Livetime
BBCLL1(>0 tubes)	31141	1921013.65	0.89
BBCLL1(>0 tubes) novertex	6732	3196505.83	0.89
ZDCLL1wide	6227	370696.78	0.9
BBCLL1(noVtx)&(ZDCN  ZDCS)	6396	1498978.93	0.9
BBCLL1(>0 tubes) narrowvtx	4070	925279.35	0.89
ZDCNS	4411	233334.89	0.89
ERT_4x4b	0	93.22	0.88
ERTLL1_4x4a&BBCLL1(noVtx)	0	490.47	0.89
ERT_4x4c&BBCLL1(noVtx)	1	2191.87	0.9
SG3&MUID_1H_N  S	95	14830.21	0.88
ERTLL1_E&BBCLL1(narrow)	1	1039	0.9
CLOCK	46765	9388833.68	0.89
MPC_B	0	263.11	0.89
MPC_A	0	1511.4	0.89
MPC_C&ERT_2x2	0	189.37	0.9
(MPCS_C&MPCS_C)  ((MPCN_C&MPCN_C)	0	10.19	0.63
((MUIDLL1_N2D  S2D)  ((N1D&S1D))&BBCLL1(noVtx)	0	260.64	0.63
((MUIDLL1_N1D  S1D)&BBCLL1(noVtx)	55	20196.39	0.87
RPC1+RPC3_S	359	23841.89	0.9
RPC1+RPC3_N	539	72270.55	0.9
SG3&RPC3&MUID_1D_N  S	2	5526.47	0.86
SG1+RPC1(C)&MUIDLL1_N  S	0	146.32	0.86
MUON_S_SG1_RPC3A&MUID_S1D	0	31.27	0.89
MUON_N_SG1_RPC3A&MUID_N1D	0	74	0.84
MUON_S_SG1&BBCLL1(noVtx)	2697	323237.99	0.9
MUON_N_SG1&BBCLL1(noVtx)	11128	1095764.77	0.9
MUON_S_SG1_RPC3_1_B  C	0	66.32	0.89
MUON_N_SG1_RPC3_1_B  C	0	173.57	0.88

Table 4.4: A typical run from the 2013 data set. This run was numbered '396418', according to PHENIX's numbering scheme. The 'name' column is the name given to the physics trigger, with one trigger per row. Names are descriptive, such that when boolean operators appear, this corresponds to that operation on the presence of that particular subsystem's trigger signal. Though a W-boson can occur for any triggered events, events firing a 'MUON' styled trigger are most likely. One can get a flavor for the relative frequency of triggers in the "Raw Trigger Rate" column (Hz), as well as the relative importance of that trigger in data taking, from the "Scale Down" column. Rare triggers have a smaller scale-down than common ones. The live-time column describes the fraction of the time that PHENIX saw an event worthy of recording, and then recorded it.

binary representation is flipped to "1" and the rest of the digits are "0". In this way, one can easily store and check which triggers for a recorded event actually fired. Thus, an important variable called 'trigscaled' in this analysis can be created, to track which triggers which fired on a certain event by taking the bitwise-OR operation between all binary representations of triggers which fired for that event.

For example, consider a simplified version of this scheme with four assigned trigger bits. Lets say we have an event where the following triggers fired:

- Trigger 1 Fired: 0001
- Trigger 3 Fired: 0100
- Trigger 4 Fired: 1000

The boolean-OR bitwise comparison is then:

- Trigscaled: 1101

Note how we lost no information regarding which triggers fired for this event. We can recover later, in code, the trigger mix for every event by using bitwise-AND operations, so long as we know which triggers were assigned to which bit, and we have the trig-scaled number.

This bit-masked final number, ones and zeroes, is one of the crucial variables in all PHENIX data sets (discussed in the next chapter). It is crucial to know which triggers fired for which event so that the original collision conditions, and therefore the physics, can be reconstructed. Since each detector subsystem may not have the same geometric acceptance, trigger acceptance, signal traducing hardware, triggering, while necessary for taking data, introduces severe bias into the data set. Knowledge of which triggers fire for each recorded event gives us the ability to correct for these kinds of biases to recover the original conditions of the data sample.

# Chapter 5

## Data Wrangling

The work discussed in this chapter was done in close collaboration with Dr. Ralf Seidl, Dr. Francesca Giordano, Daniel Jumper, and Abraham Meles. Eventually the analysis group merged with another year's analysis group, bringing in Dr. Sanghwa Park, and Dr. Chong Kim, who have made crucial contributions to this analysis, and have studied the complimentary 2012 data set, producing their own PhD theses on this analysis. Dr. Hideyuki Oide has also heavily influenced the techniques and work-flow of this analysis, pioneering many of the techniques used here (at PHENIX at least) for his analysis of the 2011 data set.

### 5.1 Overview

Although we have discussed in detail the theoretical motivations for the W physics program, as well as the machines producing the necessary collisions and recording data produced from these collisions, we have not yet addressed the form of the data set itself, and the substantial engineering it takes to extract the signal of interest out of that data set.

The relative abundance of the  $p + p \rightarrow W^\pm \rightarrow \mu^\pm + \nu$  signal events is rather low, compared to the other interactions which may take place when two protons collide. We must allow several hundred million proton proton collisions to occur, before we have a high probability of observing just one W-Boson event.

We discussed in the previous chapter how careful triggering is employed in order to ensure that any time this event does occur, it is recorded. This does not guarantee that we *only* record these events. Background events are still recorded much more frequently than

signal events, even with the improved triggering. The number of  $W \rightarrow \mu$  events produced over the 2013 data set number in the hundreds, while the total number of recorded events is approximately 15 billion.

This leads to the substantial problem of fishing out the appropriate physics events from the 15 billion event haystack. Why, I hear you ask, don't we just have a detector which can record only the W-Boson events of interest?

Because, as a multipurpose spectrometer, PHENIX must be ready to take all kinds of data, and satisfy many experimental requirements, in addition to fitting a lot of functionality into a relatively tight budget, as is common for federally funded research. Although this measurement would have been made much simpler with a forward calorimeter, we can't simply build and install a calorimeter the moment that an analysis would benefit from its presence.

So, instead, we must rely on our ingenuity and deep understanding of the data set, to tease out the results we want to measure.

## 5.2 Raw Data to Reconstructed Parameters

Any time a PHENIX trigger condition is satisfied, all of the information recorded by the PHENIX spectrometer are read out from temporary on-detector memory, and fed into a data stream that eventually is archived as a 'PHENIX Raw Data File Format' or PRDFF.

PRDFF data is hierarchical, first being organized by event-type, and then organized by packet-type. There are many event types - 'DATAEVENTS' typically carry the information relevant to a physics analysis, whereas other event-types carry very important QA information for determining the status of the RHIC apparatus, the beam, polarization, and PHENIX performance.

Every packet has a header, which contains general information such as what the packet contains, and in what order that packet was received. Every packet recorded can be associated with a unique event-sequence number, which specifies roughly the order in which the event owning the packet was received by the DAQ. Within a given run number, an event-number is guaranteed to be unique. The complexity of the packet is limited by the bandwidth available to move data off PHENIX onto other storage, and the buffers/reconstruction ability of the front end electronics modules built onto PHENIX sub-

systems. PHENIX archives data from the DAQ at a rate of approximately 700 Megabytes per second - or one compact disk.

Generally, raw PHENIX data is too complex to use straight-away, because minimal to no reconstruction of physical properties for a certain event is done, due to hardware limitations and time limitations - some of this raw data is often directly used in triggering decisions, which must be made once every 106 nanoseconds or faster (the bunch crossing frequency).

The raw data collected from PHENIX undergoes a process called "Data Production", where physical parameters are reconstructed from the simpler raw data. Raw data could take any form - for example - which cathode strips were activated in an event in the muon tracker, or, the number of photons counted in a photomultiplier tube. This information is often combined with extensive survey information about the geometry of a given detector, the known magnetic field in a detector, to reconstruct quantities such as momentum, or deposited energy.

Once reconstruction has finished in a Data Production, the data are then repackaged into ROOT files, often times internally structured into custom output objects which are associated with a various detector. These output objects are simply custom written C++ classes which have a serialization scheme, which have libraries and dictionaries compiled that allow for them to be serialized into ROOT's file format.

For the purposes of this analysis, all data has been reconstructed and serialized into a specific type of output object called a 'picoDST' or even more concisely, 'pDST'. This name, like many others in PHENIX has historical context: DST stands for 'Data Summary Tape' hearkening back to the days when data was stored primarily on magnetic tape (it is still archived on magnetic tape!), and 'pico' because of its relatively small disk-space requirement, compared to 'nanoDST' files or simply 'DST' files. I'm not making this up, I swear!

### 5.3 Choosing Analysis Variables

Even data reduced to the point of a pDST still is much more complicated and comprehensive than what is needed for this analysis - there are thousands of variables relating to reconstruction parameters. We only need a handful of variables for this analysis, summarized on Tables 5.1, 5.2, 5.3 and 5.4. When Cartesian coordinates are referenced,

implicitly, the reference frame is the PHENIX Coordinate system (Figure 5.2).

As you can probably guess, the only variables which are truly relevant to this analysis need to be relevant to understanding two questions:

1. *Is this reconstructed muon track the result of a real W-Boson Decay?*
2. *What is the polarization of the two colliding protons for every recorded collision?*

To properly answer these questions, we need to comprehensively understand what processes are capable of producing muons, as well as whether or not our detector can be 'tricked' by signals which look like muons, but really aren't. Secondly, we need a means of recovering the proton spin polarization for each colliding bunch-pair.

Polarization recovery is straight-forward - we already have mechanisms in the data stream which number and track the colliding bunch pairs. We additionally have well defined spin patterns which are applied to the 120 bunches, the same way every time this pattern is applied to the fill. As discussed previously, we have good QA apparatuses in place to ensure the advertised spin pattern is the same as the delivered spin pattern. Since polarization patterns do not typically change in a standard physics beam fill (if they do, alarms are raised and the data is typically discarded), all that is needed is to associate a PHENIX run number, with a RHIC fill number, and then look up the spin pattern, which in effect, is a database-call. Of course, the overall beam polarization percentage is an important factor, which dilutes any spin asymmetry, but this is taken into account in the final spin database QA analysis [70].

This leaves us with the first question, and the difficulty in answering this question is essentially that it is challenging to differentiate signal  $W \rightarrow \mu$  events from other  $X \rightarrow \mu$  events, or even events which look like muons, but are really due to incorrect track reconstruction.

Therefore, the thrust of the Data Analysis portion of this work is really just to tease apart the real W-genic muons, from all other muon candidates. To this requires some substantial feature engineering, and creating some statistical models, as well as a means of evaluating the performance of these statistical models - which is difficult because validating any statistical differentiation technique (aka machine learning technique) requires a labeled

Name	Description
Run_Number	A unique number identifying a run in a RHIC fill for PHENIX
Evt_Number	A unique number within a single run identifying the approximate order an event was taken.
Evt_bbcZ	The event z-vertex calculated by the BBC
triggerbit	The result of a bit-wise 'OR' applied to all 32-bit trigger bits which fired
clockcross	The bunch number of the two colliding bunches [0 – 119]. Required to look up the spin polarization, along with Run_Number

Table 5.1: Variables characterizing events overall

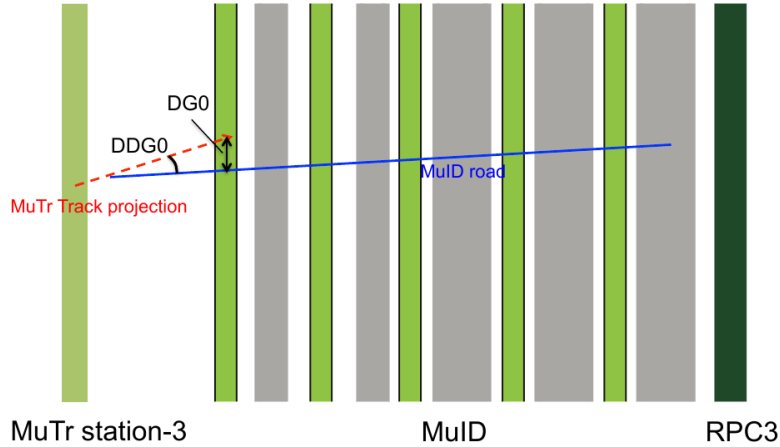


Figure 5.1: A schematic representation of the matching variables, DG0 and DDG0 at the intersection between the Muon Tracker and Muon Identifier [25]

data set, and we intrinsically do not possess this, since otherwise, this analysis would not need to be done.

The engineered variables in this analysis are  $dw_{13}$ ,  $dw_{23}$ ,  $d\phi_{13}$ , and  $d\phi_{23}$ . These variables are calculated from reconstructed physics data. They play an important role in our extraction of the signal to background ratio. The  $d\phi_{ij}$  variables represent the difference in azimuthal angle observed at the MuTR station i and j respectively.  $dw_{ij}$  is constructed

Name	(Unit) Description
Evt_Nmu	The number of muon tracks reconstructed for a given event
charge	$(\pm e)$ The charge associated with a reconstructed muon track
$p_z$	(GeV) The z-momentum associated with the muon track
$p$	(GeV) The total momentum of a charged track
$\chi^2$	The result of the Kalman fitter reconstructing the track
lastGap	The last gap in the Muon Tracker which was activated (there are 4)
$\eta$	The rapidity of the track
$\phi$	(rad) The azimuthal position angle the track makes relative to the x-axis
DG0	(cm) A Track matching variable (matching between MuID and MuTr) associated with the MuID road, at MuID station 3.
DDG0	(degree) The opening angle between the MuID track road, and the MuTr projection onto the MuID
xSta <sub>i</sub>	(cm) The x-coordinate of the track at Station i, $i \in 1, 2, 3$ of the MuTr
ySta <sub>i</sub>	(cm) The y-coordinate of the track at Station i, $i \in 1, 2, 3$ of the MuTr
$\phi_i$	(rad) The angle the track makes with Station i, $i \in 1, 2, 3$ , i.e.: $\phi_i = \tan^{-1} \left( \frac{x_i}{y_i} \right)$
$\theta$	(rad) Azimuthal angle of track, $\tan^{-1} \left( \frac{p_T}{p_z} \right)$
DCA <sub>z</sub>	(cm) Distance of closest approach between the z-vertex positions extracted by projecting the MuTR track z-vertex back to the BBC z-vertex
DCA <sub>r</sub>	(cm) Distance of closest approach between the track and beam axis

Table 5.2: Muon tracker variables. Generally, this data set is indexed on a subevent level, where one event will contain all reconstructed muon tracks seen for that event.

Name	Description
$fvtx_{d\phi}$	The $\phi$ residual between MuTR track and FVTX track
$fvtx_{d\theta}$	The $\theta$ residual between the MuTR track and FVTX track
$fvtx_{dr}$	The radial residual between the MuTR track and the FVTX track
$fvtx_{conebits}$	The number of FVTX clusters inside a cone around the track defined by: $0.04\text{rad} < dR < 0.52\text{rad}$ where $dR = \sqrt{d\eta^2 + d\phi^2}$

Table 5.3: A summary of the variables reconstructed from FVTX raw data [29].

Name	Description
RpcMatchSt1	Distance of closest approach between projected MuTR track onto the RPC 1 and the closest hit cluster on RPC 1
RpcMatchSt3	Distance of closest approach between projected MuTR track onto the RPC 3 and the closest hit cluster on RPC 3

Table 5.4: RPC Track matching variables

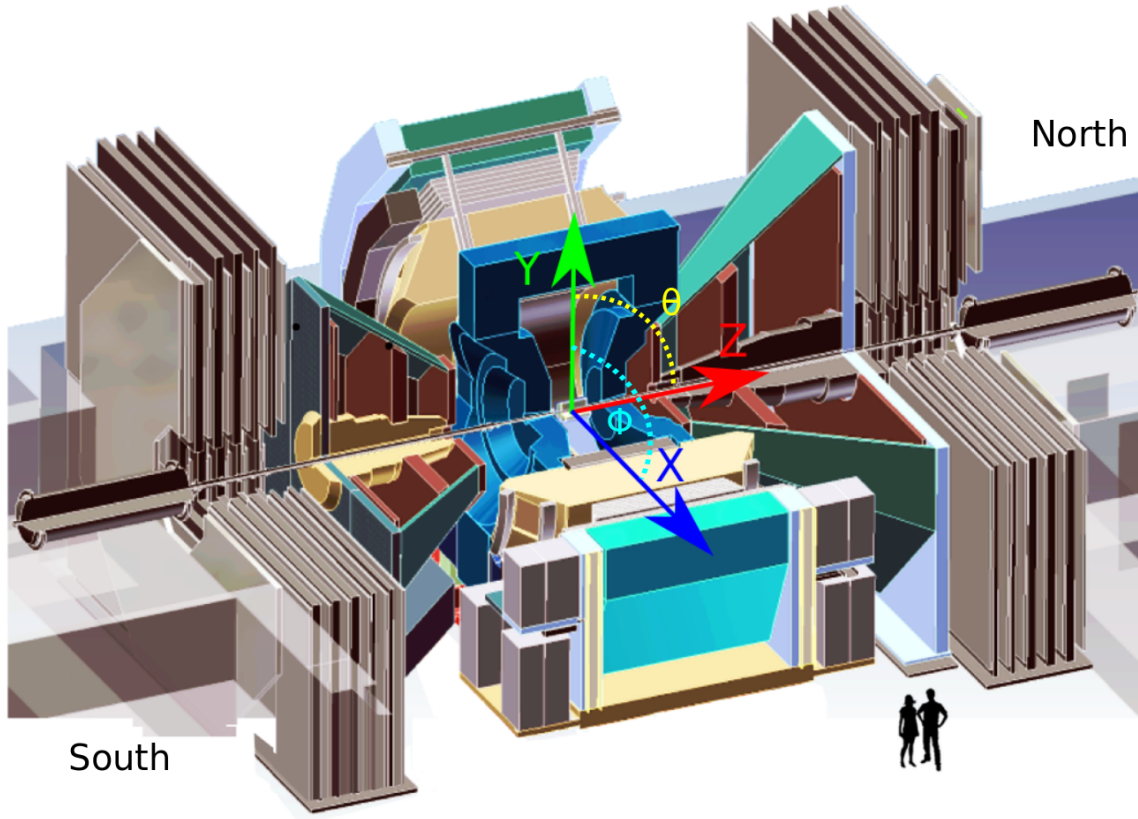


Figure 5.2: The PHENIX coordinate system is shown (RGB arrows) at the center of the nominal interaction point within PHENIX, the origin, in this quarter-cutaway drawing. The small black figures are actually miniaturized human beings, the PHENIX detector is very small - this is a full scale drawing of PHENIX. Shown: the x, y, and z coordinates, as well as the azimuthal coordinate,  $\theta$  and polar coordinate  $\phi$  [26]

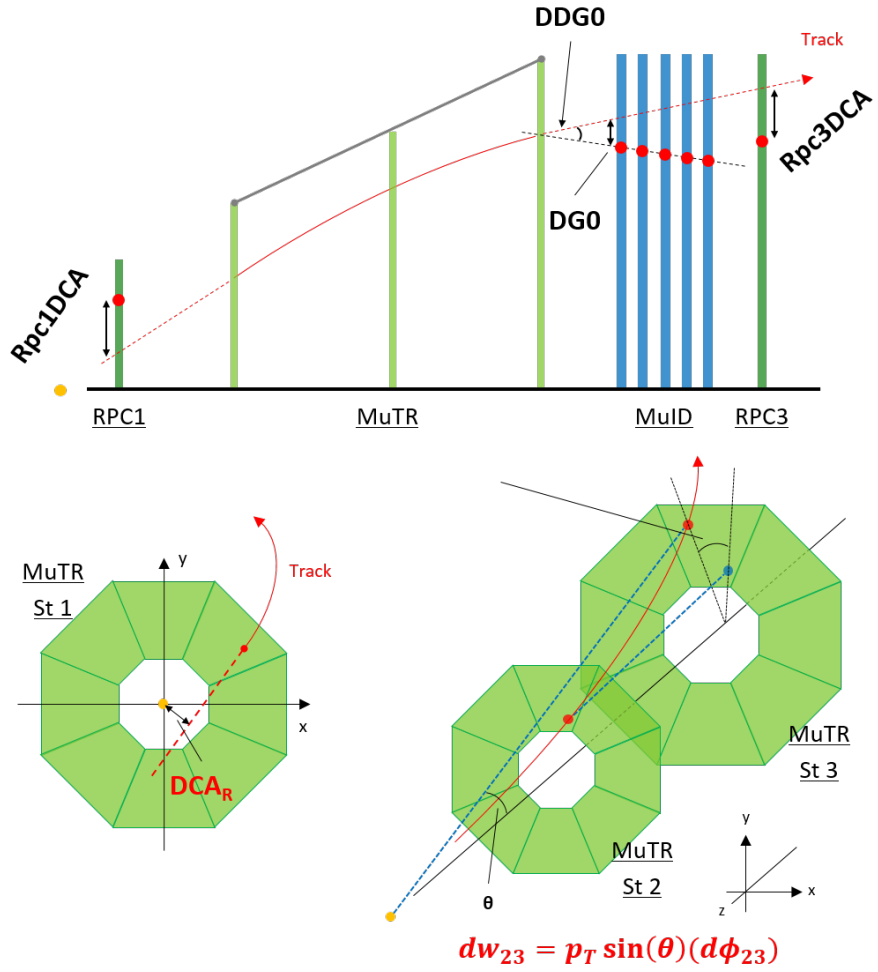


Figure 5.3: A nice summary of discriminating kinematic variables reproduced with permission from Dr. Chong Kim. We see the MuTR tracking planes in green, and a muon track penetrating the planes in red, and reference coordinates in the lower right-hand corner. The geometric relationship between the roads, reconstructed track are shown in the annotations.

from  $d\phi_{ij}$  as follows:

$$dw_{ij} = p_T \times \sin(\theta) \times d\phi_{ij} \quad (5.1)$$

While  $\phi_i$  is calculated from the x and y coordinates at Station i:

$$\phi_i = \tan^{-1} \left( \frac{ySta_i}{xSta_i} \right) \quad (5.2)$$

A common theme amongst these variables is that they should help us distinguish between high momentum muon tracks from W-Bosons, and other muon tracks. The hope is that the muon tracks from W-Bosons are kinematically restricted to have a relatively narrow momentum distribution in the forward kinematic regime, and so therefore, tracking variables can be used to partially differentiate between signal and background events.

In general, W-genic events will be mostly straight, geometrically, and so this constrains the values of variables such as  $DCA_r$  substantially, and other variables less so. Thus,  $dw_{23}$  should be a good discriminator, as it depends on  $p_T$  and the azimuthal bending of the charged tracks, due to the radial magnetic field in the MuTR.

Our secondary requirement of our variables is that they are relatively uncorrelated with each-other, to leave plenty of room for statistical modeling. Ultimately, we chose a subset of the available tracking variables to carry out the analysis, in two stages. The correlation of variables for both data and simulation are summarized in Table ??.

In the first stage of the analysis, we use: DG0, DDG0,  $DCA_r$ ,  $\chi^2$ , Rpc1DCA, Rpc3DCA,  $fvtx_{dr \times d\theta}$ ,  $fvtx_{d\phi}$ , and  $fvtx_{cone}$ . Of these variables, some were grouped to account for correlations: DG0 and DDG0,  $\chi^2$  and  $DCA_r$ . These variables are all related to track reconstruction. The Muon Tracker reconstructs tracks by essentially connecting the dots between x and y coordinate 'hits' that it records at each station. The lines connecting these hits are called 'roads'. Following this, the roads and hits are used to generate a curve fit to the data, given knowledge of the muon tracker's radial magnetic field. From this curve, we extrapolate the charge and momentum, and we construct variables which codify the difference between the reconstructed curve, and the 'connect the dots' roads. The smaller these differences are, the more straight the track is, and as discussed, straightness points to higher momentum, which ultimately leads to labeling as a W-genic particle, if the momentum is in the correct range.

In the second phase of the analysis, we use  $dw_{23}$  and  $\eta$  primarily. Both stages of the analysis are discussed in the following sections.  $dw_{23}$  is related to track straightness as

well, and is referred to as "reduced azimuthal bending". Since we're interested in forward muons,  $\eta$  is used as our second variable.

Generally, we are interested in recovering forward  $\mu+$ , forward  $\mu-$ , backward  $\mu+$  and backward  $\mu-$ . As the muon arms do not have the same rapidity coverage, we separate the data into these four categories - forward positive charged tracks, forward negatively charged tracks, backwards positively charged tracks and backward negatively charged tracks. Due to the geometry of the muon arms, the North Arm will always correspond with forward positive rapidity, whereas the South Arm will always correspond with backward, negative rapidity. I will use 'forward and backward' interchangably with 'North and Sout'. We perform all calculations with our data set in parallel between these four conditions.

The data is further subdivided based on the available track matching variables for a given event, but these subdivisions are not kept separate from the overall arm-charge separation. Some variables, such as the RPC track matching variables and the FVTX track matching variables exist for some events, but not others. We will discuss how this is managed in later sections, but this data is not generally partitioned in this way.

# Chapter 6

## Feature Engineering

The ultimate goal of Feature Engineering is to clean the data and transform the data with heuristic strategies that tag events coming from signal sources, as separate from events which come from our background, so that we can proceed with the calculation of the physics asymmetry.

Even with the Forward Upgrade (Section ??), our data set is still composed mostly of background events (Figure 6.1). The primary constituents of the data set are muons from the following sources:

- **Hadronic Background**

- The hadronic background is composed of hadrons which are produced from the primary event vertex, and then travel into the muon arms. The hadrons then decay in the muon arms, and create hits at each station, which are misreconstructed as high- $p_T$  muons.

- **Muon Background**

- The muon background is composed of processes which produce real muons which fall into a similar kinematic regime of the W-genic muons

- **W Signal**

- These are muons we are looking for. They come from the W boson decay, and carry information about the proton spin.

We will differentiate these types of data in two different step. In the first step, we will use likelihood event selection, where we lump hadronic background and muon background together, and merely distinguish it from W-genic events. In the second stage, we will further differentiate our model for the background, drawing heavily on the data to understand the hadronic background, and providing simulations of the W-genic events as well as simulation cocktail for other muon background events. Before we discuss this differentiation, it is important to discuss the simulations, as the rest of the analysis hinges on the simulation of both the W-genic events and the Muon Background events.

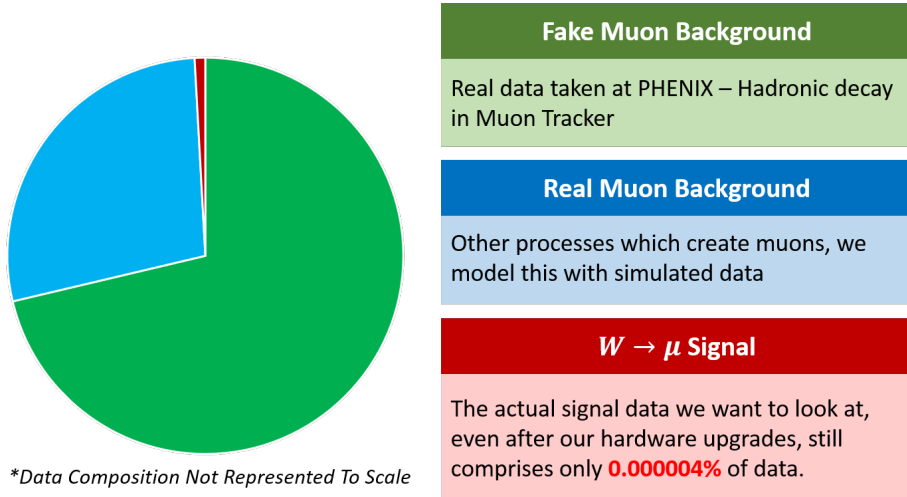


Figure 6.1: A cartoon of the dataset composition. The data, even after the Forward Upgrade, is mostly composed of hadronic background, which has tricked our Muon Tracker.

In subsequent sections, I will discuss what we do with the variables which we have chosen to use to identify W-genic events. Because our data set is so dominated by background sources, we must rely heavily on simulations to estimate what our signal events might look like. As of the time of this writing, the analysis has not yet incorporated the simulation of hadronic background, which is quite difficult, as there are a lot of effects at play - particles which interact with the material of PHENIX itself to produce secondary and tertiary vertices, for example. However, if we can simulate accurately the signal process (the W-Boson cross section and its scaling with energy is known to excruciating precision), and the muon background processes (known to similarly high precision), we can approach the problem from a standpoint of using our data set as a relatively good model for what

'hadronic background' looks like, and use simulations to fit the portions of the data which cannot come from this hadronic background.

## 6.1 The Basic Cut

The basic cut aims to remove all obviously bad events from our event mix. The cut approaches this from two premises. The first, is that if track reconstruction variables simply cannot have resulted from a W-genic event, then we remove the track. Secondly, if the track corresponds to a reconstructed energy which is larger than what is physically allowable for a W-genic track, we remove it.

The "Basic Cut" is defined:

Variable	Lower Bound	Upper Bound
MuID lastGap	*	Gap 4
$\chi^2$	0	20
$DG0$	0	20
$DDG0$	0	9
$\mu$ candidate	*	1

Table 6.1: The Basic Cuts used in the Run 13 analysis. lastGap refers to the last gap in the MUID which saw a  $\mu$  candidate event. The fourth gap is the furthest penetration possible, therefore suggesting a high energy muon. Other parameters are described in Tables 5.1, 5.2, 5.3, and 5.4

With this cut, we have removed quite a large fraction of the data, without worry of removing signal events.

## 6.2 Simulations

I did not do any work to produce the simulations used in this analysis, all of that credit goes to Dr. Ralf Seidl. I will generally describe how the simulations were produced, and paraphrase from the analysis note which we co-wrote with contributions also from Dr. Giordano, Abraham Meles and Daniel Jumper: [27].

PHENIX has a rather well developed simulation framework, which uses the in-house built "PHENIX Integrated Simulation Application" (PISA) [?] custom simulation framework. The simulation framework models in great detail the entire 12mx18mx18m volume of the PHENIX apparatus, as well as all the various material properties of the apparatus. The software package originated from the GEANT geometry and tracking packages. PISA encompasses more than this, though, it additionally encapsulates event-generators, a standalone geometry verification package, and the PHENIX offline analysis shell, to generate data that is completely compatible with PHENIX's data packaging framework. PISA has since been integrated into a simulation work-flow with the popular PYTHIA event generation system.

The simulations were created by selecting the biggest sources of muon background known to be produced at PHENIX as well as the W-Boson event and producing many events to generate good statistics. The primary purpose of simulating the muon background and W-Signal is to ultimately generate probability distribution functions for the variables which have the largest analyzing power - i.e. ability to differentiate between signal and background. The simulation and data both are ultimately described by the same variables.

The data are added together, when combined to generate a 'muon background pdf' or 'W-Signal pdf' according to the cross-section of the process and the number of generated events, so as to not add these ingredients into the cocktail in the wrong amounts. This process is described in the next section, but the simulations used in this analysis are summarized here, in Table 6.2. When adding the simulations together, one must be careful to scale the final-yields by a correction factor (called k-factor) such that events which produce boosted dimuons are properly accounted for.

PHENIX uses some somewhat exclusive jargon when describing the various quark bound states which contribute to the muon background, and signal events. Open charm or charmonium refer to the bound state of the  $c\bar{c}$  quarks. Onium generally refers to any process where a particle is in a bound-state with its own antiparticle (without of course

double-counting open charm/charmonoim). Direct photon, or alternatively  $d\gamma$  (sometimes also written as DY) refers to photons that are produced as an immediate result of an inelastic scattering process, not from secondary decays. Open bottom refers to the bound state of  $b\bar{b}$  quarks.  $Z/d\gamma$  refers to the production and decay of the mixing between the Z-boson and virtual photons. ONLY Z refers to Z production and decay. W is naturally the signal event. W tau refers to the production of tau leptons, which can decay weakly, producing electrons or muons. W had refers to the production of W bosons from hadronic processes, rather than as the primary event vertex. All of these processes are summarized in Table 6.2.

Reference Run 393888				
Process	k factor	$\sigma$ (mb)	# Events	$\mathcal{L}$ ( $fb^{-1}$ )
$c\bar{c}$	2.44	5.71e-01	5.85e+11	1.02
onium	0.415	1.35e-01	1.5e+11	1.11
$d\gamma$	0.0	5.32e-02	5.84e+10	1.10
$b\bar{b}$	1.83	7.30e-03	7.36e+09	1.01
ONLY Z	1.25	3.37e-07	1.73e+08	577.0
W	1.5	1.66e-06	3.38e+08	198.9
W tau	0.0	1.66e-06	3.43e+08	201.8
W had	0.0	1.66e-06	3.42e+08	201.2
Z	1.25	1.02e-06	2.93e+08	61.2

Table 6.2: Simulated sub processes in Run 13 including their generated event numbers as well as the corresponding luminosity and cross sections. Dr. Sanghwa Park has done an extensive analysis of the simulated data to determine an appropriate k-factor. Process which contribute very little to the muon background include W had, W tau, and  $d\gamma$ ; they are scaled to zero.

The simulations must additionally be weighted for trigger efficiency. To accomplish this, we weight events for each arm and charge with the associated trigger efficiency when constructing probability density functions representing the muon background. The trigger efficiencies generally manifest as  $\eta$  dependent functions - thus we bin the data into 20 separate  $\eta$  bins and calculate the efficiency associated with each bin. The bin ranges, and efficiency corrections are summarized in Table 6.4 for the North arm, and Table 6.3 for the

		<b>South Arm</b>	
$\eta_{min}$	$\eta_{max}$	$\mu^- \pm stat \pm sys$	$\mu^+ \pm stat \pm sys$
1.10	1.17	$0.27912 \pm 0.00297 \pm 0.10243$	$0.30607 \pm 0.00423 \pm 0.01108$
1.17	1.25	$0.40422 \pm 0.01642 \pm 0.04811$	$0.43125 \pm 0.01717 \pm 0.26702$
1.25	1.32	$0.27958 \pm 0.00056 \pm 0.05539$	$0.36619 \pm 0.00925 \pm 0.07316$
1.32	1.40	$0.26563 \pm 0.00542 \pm 0.02485$	$0.25312 \pm 0.00349 \pm 0.04927$
1.40	1.48	$0.39802 \pm 0.00497 \pm 0.07770$	$0.34295 \pm 0.00306 \pm 0.03127$
1.48	1.55	$0.43156 \pm 0.00633 \pm 0.17060$	$0.37567 \pm 0.00248 \pm 0.03644$
1.55	1.62	$0.34831 \pm 0.00309 \pm 0.03720$	$0.40246 \pm 0.00546 \pm 0.04605$
1.62	1.70	$0.33043 \pm 0.00280 \pm 0.09227$	$0.40219 \pm 0.00472 \pm 0.05637$
1.70	1.77	$0.33152 \pm 0.00318 \pm 0.11668$	$0.30805 \pm 0.00360 \pm 0.03644$
1.77	1.85	$0.34710 \pm 0.00633 \pm 0.00918$	$0.38565 \pm 0.00439 \pm 0.04295$
1.85	1.92	$0.32448 \pm 0.00404 \pm 0.14670$	$0.30118 \pm 0.00418 \pm 0.10071$
1.92	2.00	$0.31461 \pm 0.00714 \pm 0.01799$	$0.31263 \pm 0.00545 \pm 0.01643$
2.00	2.07	$0.64632 \pm 0.01161 \pm 0.23329$	$0.63252 \pm 0.01040 \pm 0.10507$
2.07	2.15	$0.60582 \pm 0.00565 \pm 0.05569$	$0.67335 \pm 0.01245 \pm 0.05630$
2.15	2.22	$0.45058 \pm 0.00697 \pm 0.45101$	$0.69619 \pm 0.01247 \pm 0.65623$
2.22	2.30	$0.45185 \pm 0.01358 \pm 0.36032$	$0.51436 \pm 0.01288 \pm 0.43781$
2.30	2.38	$0.43890 \pm 0.07336 \pm 0.34632$	$0.61623 \pm 0.06221 \pm 0.62209$
2.38	2.45	$0.00000 \pm 0.25000 \pm 0.00000$	$0.00000 \pm 0.25000 \pm 0.00000$
2.45	2.52	$0.00000 \pm 0.25000 \pm 0.00000$	$0.00000 \pm 0.25000 \pm 0.00000$
2.52	2.60	$0.00000 \pm 0.25000 \pm 0.00000$	$0.00000 \pm 0.25000 \pm 0.00000$

Table 6.3:  $\eta$  dependent trigger efficiencies are calculated for the South arm in 20  $\eta$  bins. Each correction has both systematic and statistical error accounted for.

		<b>North Arm</b>	
$\eta_{min}$	$\eta_{min}$	$\mu^- \pm stat \pm sys$	$\mu^+ \pm stat \pm sys$
1.10	1.17	$0.56285 \pm 0.03834 \pm 0.32882$	$0.52850 \pm 0.01938 \pm 0.36163$
1.17	1.25	$0.67803 \pm 0.02249 \pm 0.13431$	$0.49546 \pm 0.00261 \pm 0.16304$
1.25	1.32	$0.69537 \pm 0.01551 \pm 0.03465$	$0.63287 \pm 0.01285 \pm 0.08350$
1.32	1.40	$0.39864 \pm 0.00724 \pm 0.02330$	$0.38435 \pm 0.00762 \pm 0.11954$
1.40	1.48	$0.52102 \pm 0.00750 \pm 0.05014$	$0.49573 \pm 0.00698 \pm 0.03733$
1.48	1.55	$0.48068 \pm 0.00498 \pm 0.11579$	$0.48874 \pm 0.00357 \pm 0.08063$
1.55	1.62	$0.54113 \pm 0.00860 \pm 0.04895$	$0.50041 \pm 0.00659 \pm 0.05165$
1.62	1.70	$0.45140 \pm 0.00822 \pm 0.05718$	$0.46948 \pm 0.00755 \pm 0.09718$
1.70	1.77	$0.43203 \pm 0.00547 \pm 0.04976$	$0.40722 \pm 0.00546 \pm 0.07957$
1.77	1.85	$0.42141 \pm 0.00815 \pm 0.04366$	$0.44450 \pm 0.00628 \pm 0.04575$
1.85	1.92	$0.37946 \pm 0.00620 \pm 0.01766$	$0.37183 \pm 0.00700 \pm 0.01848$
1.92	2.00	$0.37499 \pm 0.00782 \pm 0.05026$	$0.40156 \pm 0.00678 \pm 0.02291$
2.00	2.07	$0.51268 \pm 0.00547 \pm 0.10416$	$0.60041 \pm 0.00973 \pm 0.21212$
2.07	2.15	$0.56990 \pm 0.00614 \pm 0.14507$	$0.58276 \pm 0.01392 \pm 0.25179$
2.15	2.22	$0.60527 \pm 0.01524 \pm 0.10354$	$0.60766 \pm 0.00425 \pm 0.23618$
2.22	2.30	$0.70200 \pm 0.01678 \pm 0.25233$	$0.45067 \pm 0.01008 \pm 0.24192$
2.30	2.38	$0.48294 \pm 0.00294 \pm 0.12663$	$0.54157 \pm 0.02109 \pm 0.06230$
2.38	2.45	$0.47814 \pm 0.02338 \pm 0.42026$	$0.42606 \pm 0.03092 \pm 0.25031$
2.45	2.52	$0.61788 \pm 0.14438 \pm 0.61788$	$0.29673 \pm 0.06686 \pm 0.04941$
2.52	2.60	$0.00000 \pm 0.25000 \pm 0.00000$	$0.15630 \pm 0.15630 \pm 0.18223$

Table 6.4:  $\eta$  dependent trigger efficiencies are calculated for the North arm in 20  $\eta$  bins. Each correction has both systematic and statistical error accounted for.

South arm.

We can visualize the composition of the simulated data set by stacking the relative distributions of these variables. By looking the cross-sections of these variables as a function of  $p_T$ , for each arm and charge combination, we can get a feeling for how the data set composition varies with  $p_T$  (Figure 6.2).

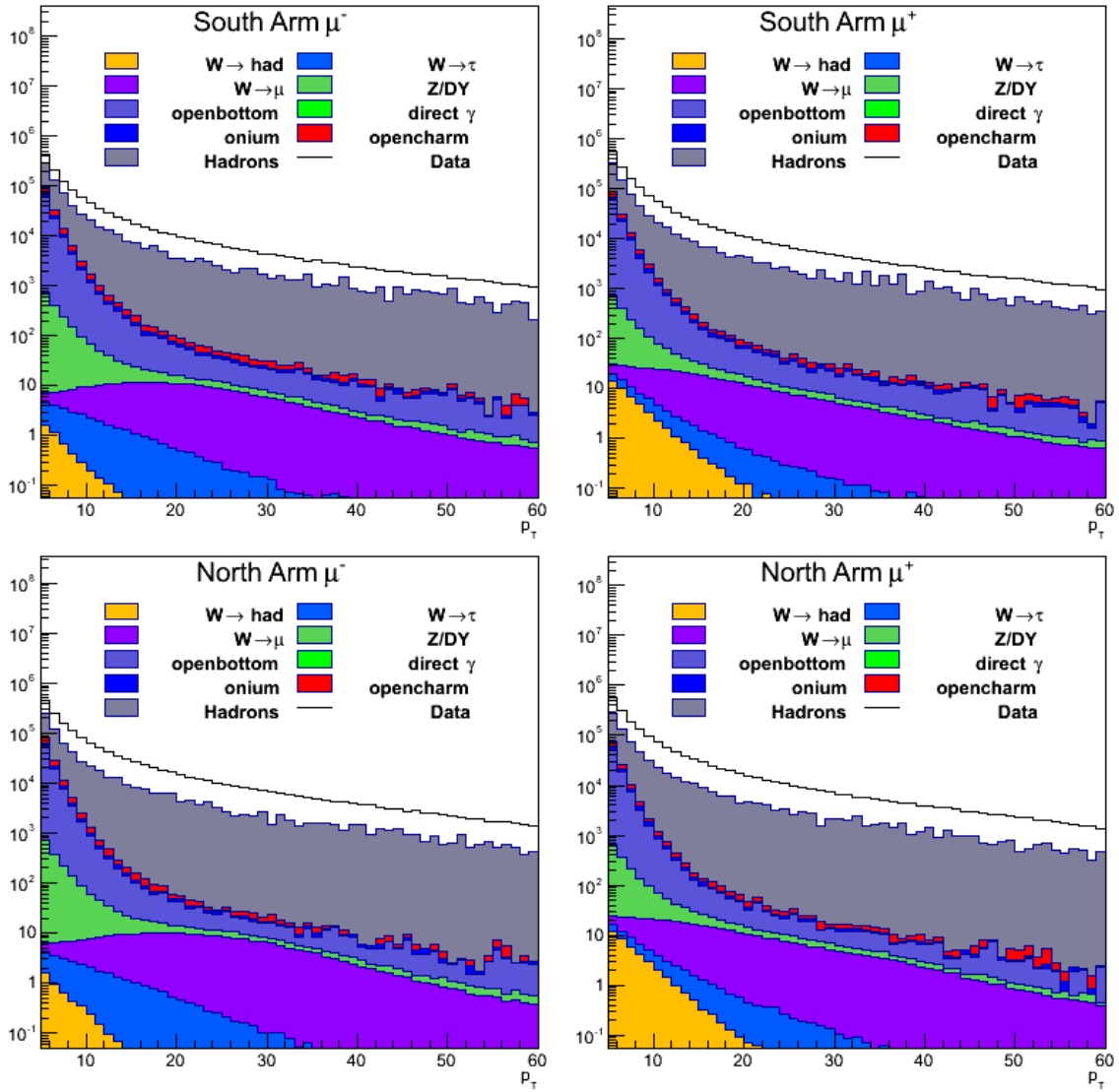


Figure 6.2: Here, we see the stacked cross-sections of all simulated processes as a function of  $p_T$ . All data shown has been created from the PISA+PYTHIA framework. Top Left: South  $\mu^-$ , Top Right: South  $\mu^+$ , Bottom Left: North  $\mu^+$ , Bottom Right: North  $\mu^-$ . Figure reproduced from my analysis note. Dr. Ralf Seidl produced the original [27]

### 6.3 $W_{ness}$ : Likelihood Event Tagging

Recalling that we have already split the dataset into three main contributions: hadronic background, real muon background, and W-Signal, we are now tasked with formulating a means to separate signal from background, using the variables which can indicate the straight-ness of a muon track.

Previous analyses have attempted to separate the muon spectrum into  $p_T$  bins, to estimate the composition, however, because the  $W \rightarrow \mu$  signal is so small in the forward kinematic regime, these methods are not sufficient, as there is no 'visible' cutoff in the spectrum.

However, we may use other methods to split up our spectrum, with the ultimate goal of calculating  $A_L$ , and correcting for background dilution using the signal to background ratio. We must use another method to effectively describe the difference between an event which comes from a signal, vs background event.

We expect that tracks which are straight are more likely to come from a W-Boson decay, because this indicates high momentum. One way of thinking of our data set can in terms of a classification problem. In a classification problem, one can use Bayes Theorem when one has a labeled testing data set to build predictive models which can classify data into two or more classes, provided that care is taken to not over-train the classifier, or attempt to classify data which has been used in the subset of data to train the classifier.

In our case, we have simulations which serve as the training data, guaranteeing that there will be no overlap between the physical data produced, and the data used to train the classifier. Thus, we implement a Naive Bayes Classifier (also known as Likelihood Selection) to label our data with two classes. Rather than labeling data with a binary classification, however, we opt to label the data with its likelihood, a posterior probability which tells us if a value is more or less likely to come from a W-Boson.

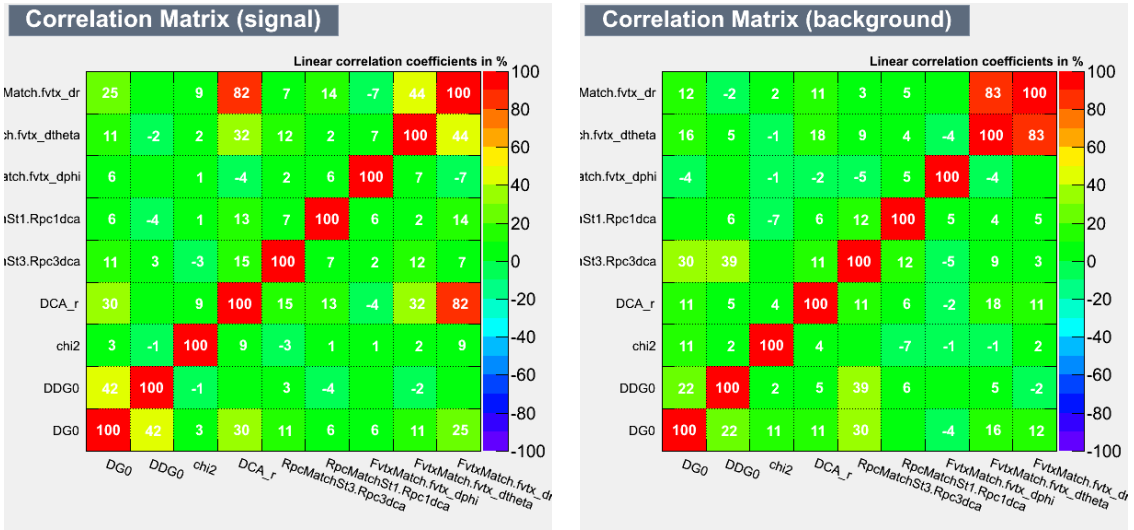
#### 6.3.1 Naive Bayes Classification

There are many techniques available for classifying a collection of variables (a feature set) into categories. Naive Bayes classification is an excellent candidate for classification, in cases where we have two classifications with distributions of feature sets which are uncorrelated. Naive Bayes even works when feature sets are slightly correlated. It is a robust, fast, scalable machine learning technique. Traditionally used for classification of

text documents, Naive Bayes is also able to handle numeric features whose distributions are known [71].

In our analysis, we begin with a Naive Bayes classifier which is trained to classify signal muons or background muons. We combine both Real Muon Background muons and Fake Muons (Hadronic Background Muons) in the label of "Background Muons" at this stage, though, later, we will separate out the muons further.

In order to obtain the best performance from our classifier, without over-training, we need to ensure that the variables (or feature set) used to determine a class are maximally uncorrelated. The variables which match this criteria are:  $DG_0$ ,  $DDG_0$ ,  $\chi^2$ ,  $fvtx$  variables,  $Rpc1DCA$ ,  $Rpc3DCA$ ,  $DCA_r$ , and  $DCA_z$ . The Linear Correlations between these variables are shown for both the data, and the simulated W-Signal in Figure 6.3.



(a) Correlations between kinematic variables, produced from simulated data.

(b) Correlations between kinematic variables, produced from the data, which is composed mostly of hadronic background

Figure 6.3: Low correlations between the signal variable distributions (from simulation), and the background variable distributions make this data set a good candidate for classification using Naive Bayes

As one can see from Figure 6.3,  $DG_0$  and  $DDG_0$  are slightly correlated, as are  $\chi^2$  and  $DCA_r$ . A Naive Bayes classifier may be constructed from the core of the familiar Bayes Theorem from probability and statistics. In our case, we understand Naive Bayes as a

conditional probability. Concretely, we consider a vector of features (i.e. our discriminating kinematic variables):

$$\mathbf{x} = (x_1, \dots, x_n) \quad (6.1)$$

and assume independence between each feature  $x_n$ . We then define the probability of a given classification,  $C_k$  given a set of features  $x_n$ :

$$\mathcal{P}(C_k|x_1, \dots, x_n) \quad (6.2)$$

This conditional probability is defined in terms of Bayes Theorem:

$$\mathcal{P}(C_k|\mathbf{x}) = \frac{\mathcal{P}(C_k) \mathcal{P}(\mathbf{x}|C_k)}{\mathcal{P}(\mathbf{x})} \quad (6.3)$$

The terms here are defined as:

- $\mathcal{P}(C_k) \rightarrow$  prior probability
- $\mathcal{P}(\mathbf{x}|C_k) \rightarrow$  likelihood
- $\mathcal{P}(\mathbf{x}) \rightarrow$  evidence

The probabilities described here are realized through constructing probability density functions from the data and simulations. The constraints of these probability distribution functions is that they are well behaved in the sense that they are finite and convergent in asymptotic limits, such that they can be meaningfully normalized.

In our case, we construct a likelihood ratio, using the posterior probability for each classification, which is defined as  $W_{ness}$ :

$$\begin{aligned} \lambda_{sig} &= \prod_k \mathcal{P}(\mu_{sig}|C_k) \\ \lambda_{bak} &= \prod_k \mathcal{P}(\mu_{bak}|C_k) \end{aligned}$$

Where  $\lambda_{sig}$  and  $\lambda_{bak}$  represent the total likelihoods that a given track is either signal, or background, constructed from the product of likelihoods calculated from each probability density function. The  $\lambda$ 's are combined to calculate the  $W_{ness}$ :

$$W_{ness} = \frac{\lambda_{sig}}{\lambda_{sig} + \lambda_{bak}} \quad (6.4)$$

Thus, we must construct probability density functions representing the likelihood of an event being  $W$ -genic or from the combined hadronic+muon background. Our data set after the basic cut has approximately 1 million events. Based on the cross-section of the  $W \rightarrow \mu$  decay, we expect the final population of  $W$ -Bosons in the data set to be on the order of 1 thousand. Therefore, we can confidently use the data set as is, in order to generate PDFs representing the hadronic+muon background, as any effect from the signal would be only one part in a thousand. Thus, we loop over the data set, and the  $W$ -Simulation set, and filter the data into probability distribution functions. Because some events do not have archived data from all subsystems, we construct a variety of PDFs, selecting the appropriate PDF cocktail based on whether or not the requisite variables were archived for that given track, Figure 6.4.

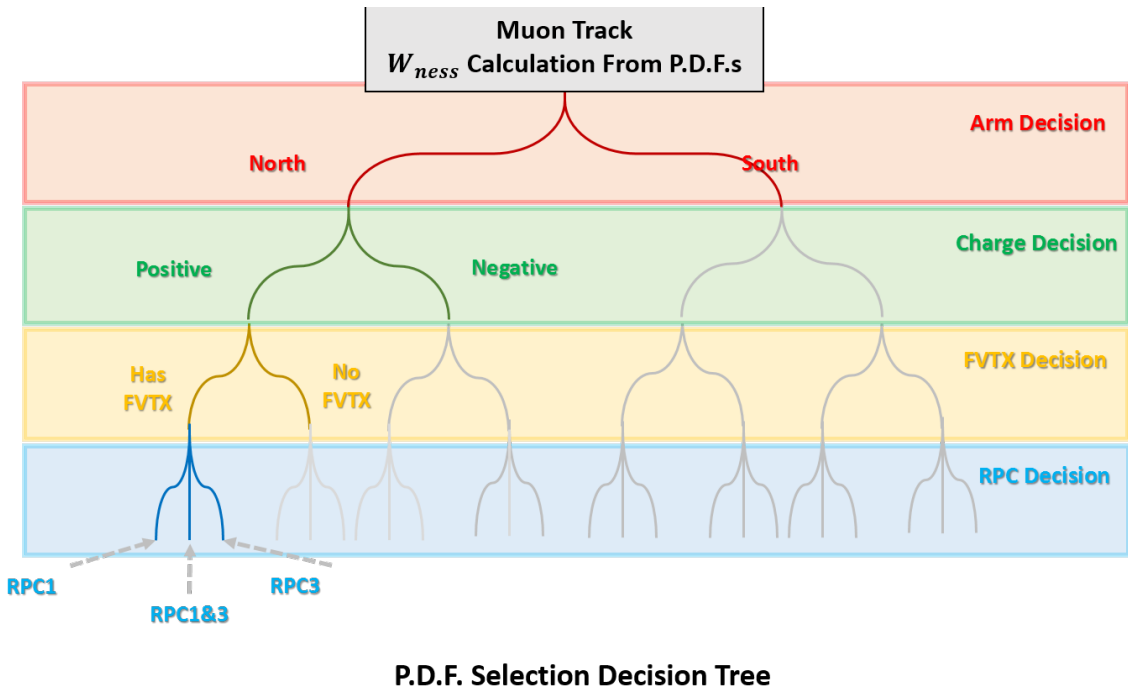
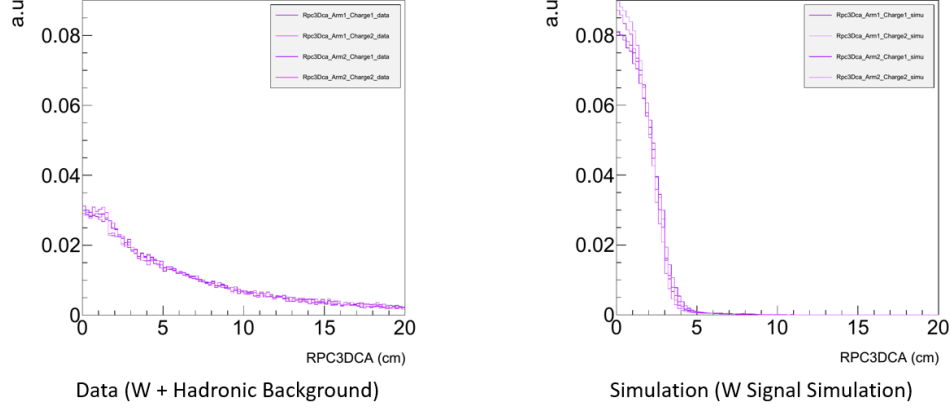


Figure 6.4: A cartoon of the decision tree to determine the PDF cocktail to use for quantifying the  $W_{ness}$  of a given track. The track's properties are used to traverse the tree, and select the cocktail contents.

In figures 6.5-6.10, we can see the various distributions which are used to create probability distribution functions. In the figures, we represent the product of all probability



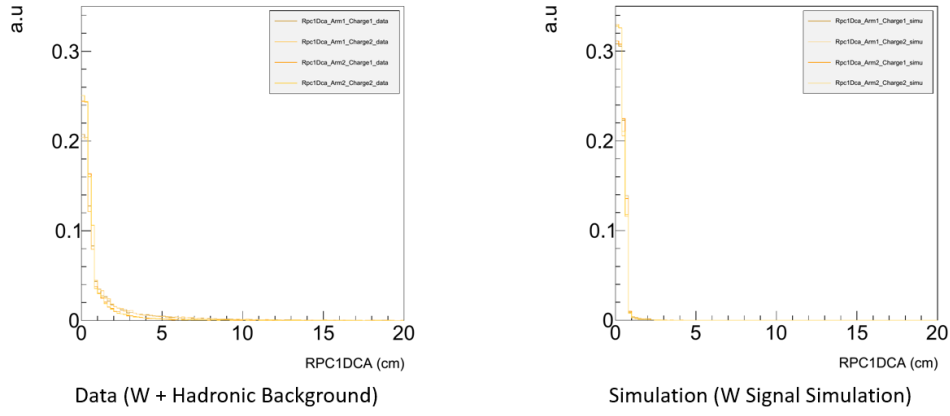
$$\lambda = p(DG0, DDG0)p(\chi^2)p(DCA_r)p(Rpc1/3dca)p(fvtx_{dr})p(fvtx_{d\theta})p(fvtx_{d\phi})$$

Figure 6.5: Left: the distribution of rpc3dca for each arm and charge, produced from the PHENIX data set, after the basic cut. Right: the same distributions from a simulation of the W-Signal.

functions which are used to tag an event as  $\lambda$  such that  $\lambda = \Pi_k \mathcal{P}(\mu|C_k)$ .

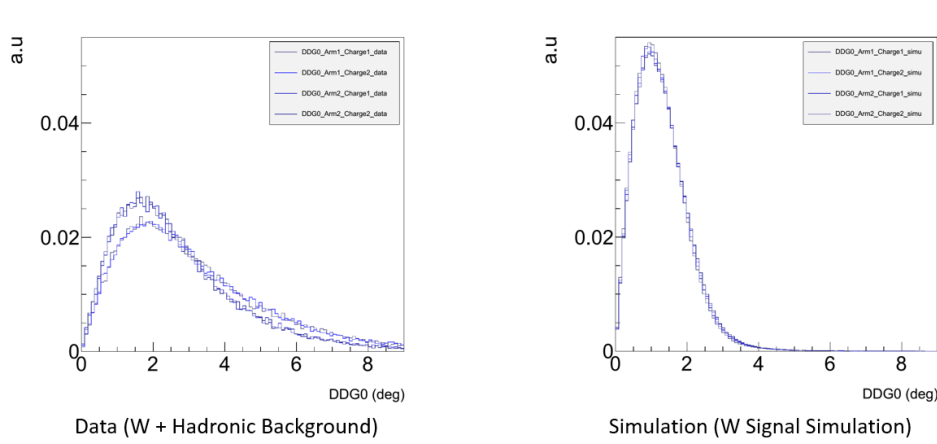
Now that we have a complete set of probability density functions which predict the likelihood that a given track is a W-genic muon or not, we can loop over the real physics data set, and use our likelihood calculation strategy to label every muon track with a  $W_{ness}$ . We may also tag our simulated data set with  $W_{ness}$ . The distributions are shown in Figure 6.11.

As we can see from Figure 6.11, most of the simulated data falls in the high  $W_{ness}$  range while most of the physics data falls in the low  $W_{ness}$  range. The goal of the likelihood analysis is to tag the data with  $W_{ness}$  such that we can apply a cut on the data based on the parameter's value. We wish to apply the cut in a way that minimally removes any signal, and we may calculate the efficiency of this cut, summarized in Figure 6.12.



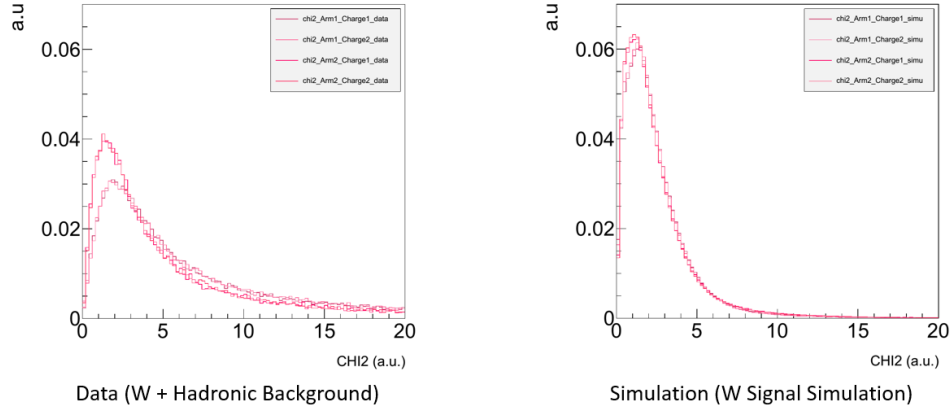
$$\lambda = p(DG0, DDG0)p(\chi^2)p(DCA_r)p(Rpc1/3dca)p(fvtx_{dr})p(fvtx_{d\theta})p(fvtx_{d\phi})$$

Figure 6.6: Left: the distribution of rpc1dca for each arm and charge, produced from the PHENIX data set, after the basic cut. Right: the same distributions from a simulation of the W-Signal.



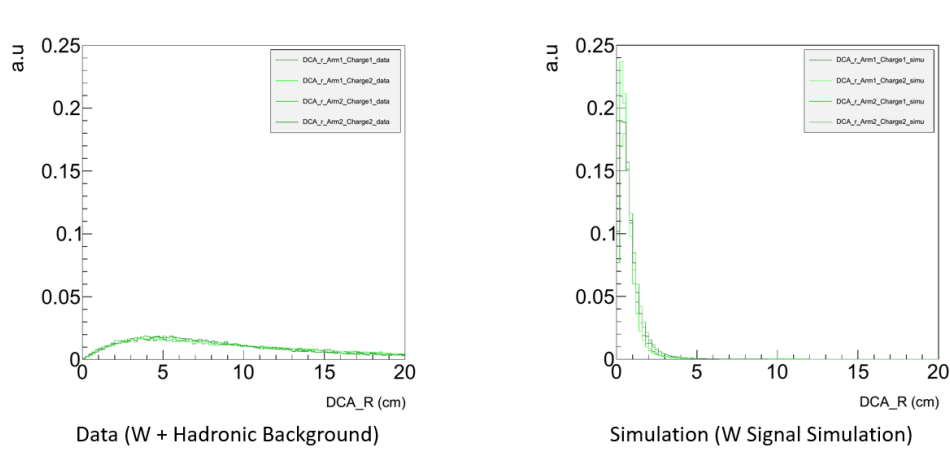
$$\lambda = p(DG0, DDG0)p(\chi^2)p(DCA_r)p(Rpc1/3dca)p(fvtx_{dr})p(fvtx_{d\theta})p(fvtx_{d\phi})$$

Figure 6.7: Left: the distribution of DDG0 for each arm and charge, produced from the PHENIX data set, after the basic cut. Right: the same distributions from a simulation of the W-Signal.



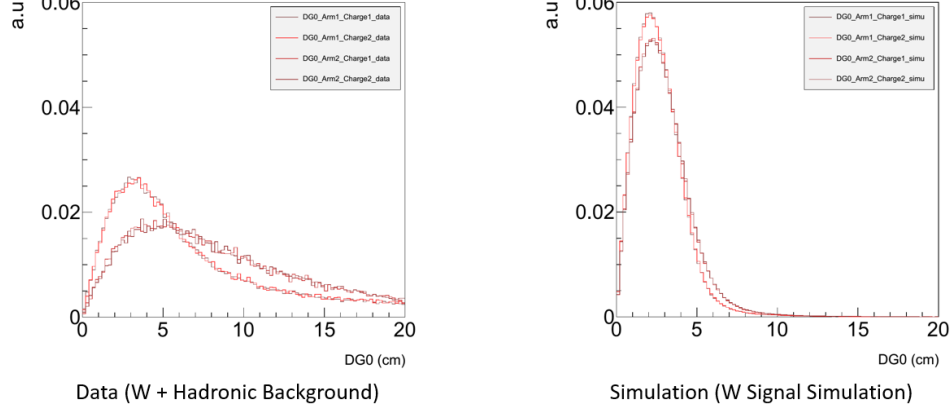
$$\lambda = p(DG0, DDG0)p(\chi^2)p(DCA_r)p(Rpc1/3dca)p(fvtx_{dr})p(fvtx_{d\theta})p(fvtx_{d\phi})$$

Figure 6.8: Left: the distribution of chi2 for each arm and charge, produced from the PHENIX data set, after the basic cut. Right: the same distributions from a simulation of the W-Signal.



$$\lambda = p(DG0, DDG0)p(\chi^2)p(DCA_r)p(Rpc1/3dca)p(fvtx_{dr})p(fvtx_{d\theta})p(fvtx_{d\phi})$$

Figure 6.9: Left: the distribution of dcar for each arm and charge, produced from the PHENIX data set, after the basic cut. Right: the same distributions from a simulation of the W-Signal.



$$\lambda = p(\text{DG0}, \text{DDG0}) p(\chi^2) p(DCA_r) p(Rpc1/3dca) p(fvtx_{dr}) p(fvtx_{d\theta}) p(fvtx_{d\phi})$$

Figure 6.10: Left: the distribution of DG0 for each arm and charge, produced from the PHENIX data set, after the basic cut. Right: the same distributions from a simulation of the W-Signal.

As we make successive cuts in  $W_{ness}$ , we find that the optimum cutoff is at  $W_{ness} < 0.95$ . We can throw out all data below this threshold, and maintain a good portion of our signal data.

Note that now with this reduced data set, we could simply assume that all remaining data is signal, and calculate an asymmetry, however, there is clearly still a lot of background present. Any background that is still present will dilute our main observable,  $A_L$ . Therefore, we employ the unbinned maximum likelihood fit to a three dimensional data set, composed of  $W_{ness}$ ,  $\eta$ , and  $dw_{23}$ .

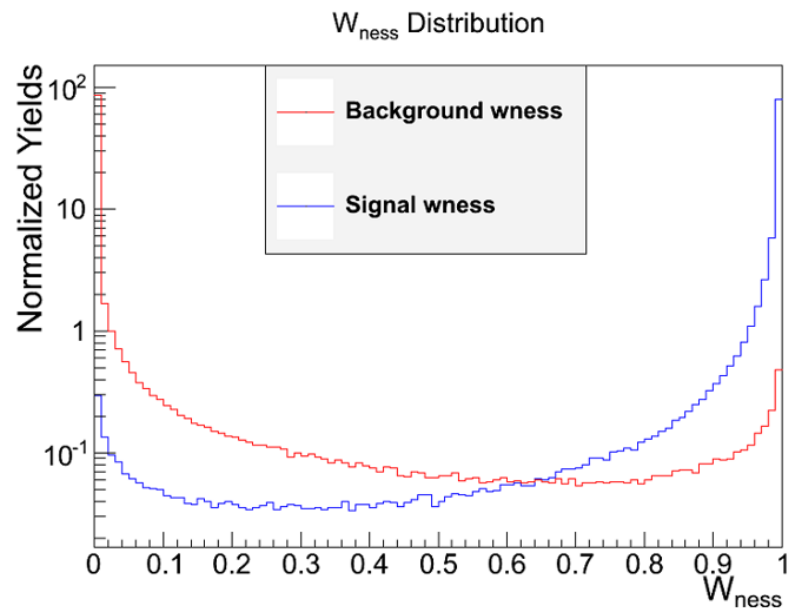


Figure 6.11: After  $W_{ness}$  tagging, we can visualize the classification of signal from background by comparing the distribution of  $W_{ness}$  in [physics data](#), and the [simulated data](#) data. Note that the vertical is plotted on a log scale. The two distributions have been normalized prior to plotting.

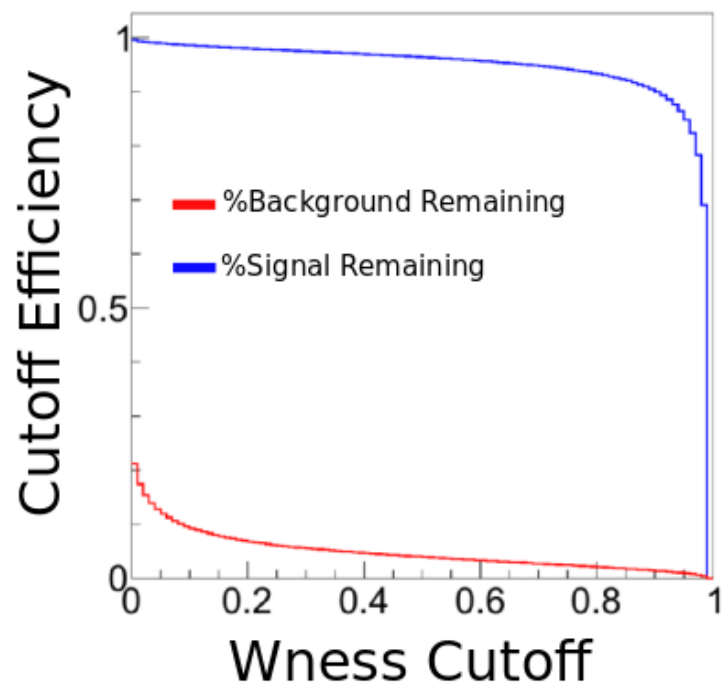


Figure 6.12: We look at the fraction of signal and background remaining in the total data set as we make successively higher cuts in  $W_{ness}$ . At the turning point of the blue distribution (the fraction of remaining signal) is where we choose to cut the data, corresponding to removing data with a  $W_{ness}$  value of less than 0.95.

## 6.4 Extended Unbinned Maximum Likelihood Selection: The Signal to Background Ratio

The goal of the Extended Unbinned Maximum Likelihood Fit (EULMF) is to calculate the signal to background ratio, so that we can calculate  $A_L$  and correct for the dilution from the background. The EULMF is another statistical method which relies on creating Probability Density Functions to represent the likelihood of given track to originate from a known source. However, at this stage in the analysis, we are interested in subdividing the background data set into contributions from the Hadronic Background and the Muon Background. We form our PDFs for the Muon Background by weighting the various individual muon processes and adding them together such that the relative frequencies of each process are comparable to the composition of the real physics data set. In broad strokes, we want to generate PDFs in the dimension of  $\eta$  and  $dw_{23}$  for Hadronic Background, Muon Background, and W-Signal distributions. However, since we will be applying this fit to a data set where we have applied a  $W_{ness}$  cut, we must be very careful to not over or under-fit the hadronic background.

In order to accomplish this, we parameterize the data set as a 2D function in  $dw_{23}$  and  $W_{ness}$ . We then fit this distribution, generated from the physics data, with a parameterization, over the nominal hadronic background dominated region from  $0 < W_{ness} < 0.95$ . We then extrapolate the shape of  $dw_{23}$  into the high  $W_{ness} > 0.95$  region, hereafter referred to as the 'signal region', with  $W_{ness} < 0.95$  referred to as the 'background region'.

Similarly to any analysis which uses probability density functions, the PDFs representing  $\eta$  and  $dw_{23}$  must be uncorrelated so as to not over-fit the data.

The purpose of the EULMF is to essentially scale the PDFs for each arm and charge for  $\eta$  and  $dw_{23}$  so as to obtain yields for W-genic muons, Muon Background muons, and hadronic background fake muons.

To use this method, we must construct the likelihood function (Equation ??) and maximize it. We write down the likelihood function in as a product of the individual likelihoods:

An unbinned maximum likelihood fit can then be performed to extract the number of events for each process:  $n_{sig}$ ,  $n_\mu$ ,  $n_{had}$ . The likelihood function is defined accounting for a Poisson distribution of the events  $x_i$ :

$$\mathcal{L}(\theta|X) \equiv \frac{n^N e^{-n}}{N!} \prod_{x_i \in X}^N \sum_c \frac{n_c}{n} p_c(x_i), ; \text{with } n = \sum_c n_c \quad (6.5)$$

where  $X$  is the sample of  $N$  total events  $x_i = (\eta_i, dw_{23i})$ , and  $\theta$  gives the parameters of the fit  $\theta = (n_{sig}, n_\mu, n_{had})$ . To reduce the number of parameters, we fixed the number of muon background events  $n_\mu$  to the expected yield according to the cross section of muon background processes, and then we extracted the remaining parameters ( $n_{sig}, n_{had}$ ) by minimizing the  $-\log(\mathcal{L}(\theta|X))$ . With Run 13 data we have enough statistics to divide the data sample in three  $\eta$  region:  $1.10 < \eta < 1.40$ ,  $1.40 < \eta < 1.80$  and  $1.80 < \eta < 2.60$ .

#### 6.4.1 Hadronic Background PDFs

The main analysis challenge for the EULMF is obtaining an adequate description of the  $dw_{23}$  and  $\eta$  distributions for the hadronic background. They are shown, along with the  $W_{ness}$  distribution for the data, for the background region, in Figure 6.13, and the simulated W-genic data in Figure 6.14.

Two features to note from Figure 6.13 and Figure 6.14 is that the distribution for  $dw_{23}$  should be expected to be quite narrow for W-genic events, whereas  $\eta$  is more broad. We have good statistic for  $\eta$  over all orders of magnitude, so we can directly construct PDFs for this variable from a binned dataset. However, with  $dw_{23}$  we need to be more careful, as this variable will offer us the analyzing power.

We create a model for  $dw_{23}$ , to fully parameterize the event distribution when viewed as a function of  $dw_{23}$  vs  $W_{ness}$ . We model this by assuming that the  $dw_{23}$  vs  $W_{ness}$  distribution can be separated into two parts:

$$F(W_{ness}, dw_{23}) = f(W_{ness}) \times g(W_{ness}, dw_{23}) \quad (6.6)$$

$f(W_{ness})$  is modeled simply as a fourth-degree polynomial (the third column) of Figures 6.13 and 6.14. The polynomial fit is summarized in Equation 6.7 and Figure 6.15:

$$f(W_{ness}) = P_8 + P_9 W_{ness} + P_{10} {W_{ness}}^2 + P_{11} + {W_{ness}}^3 + P_{12} + {W_{ness}}^4 \quad (6.7)$$

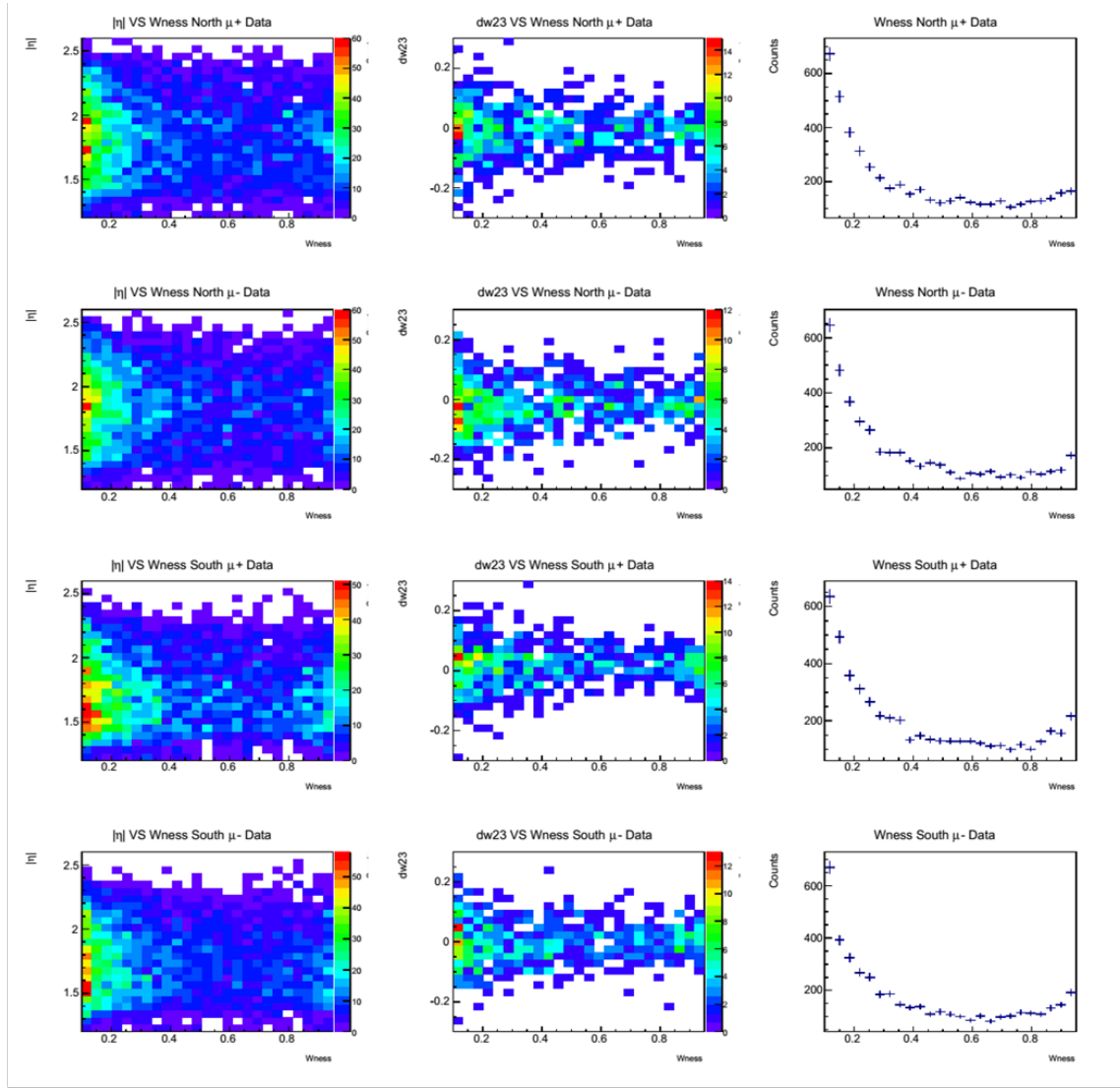


Figure 6.13: The first column of plots is  $\eta$  plotted as a function of  $W_{ness}$  where we see a 2D histogram of the even distribution. The middle column is  $dw_{23}$  as a function of  $W_{ness}$ , and the right column is a simple histogram of  $W_{ness}$ . The rows all correspond to the same arm and charge. From top to bottom: North,  $\mu+$ , North  $\mu-$ , South  $\mu+$ , North  $\mu-$ . Distributions shown here are all from the physics data set.

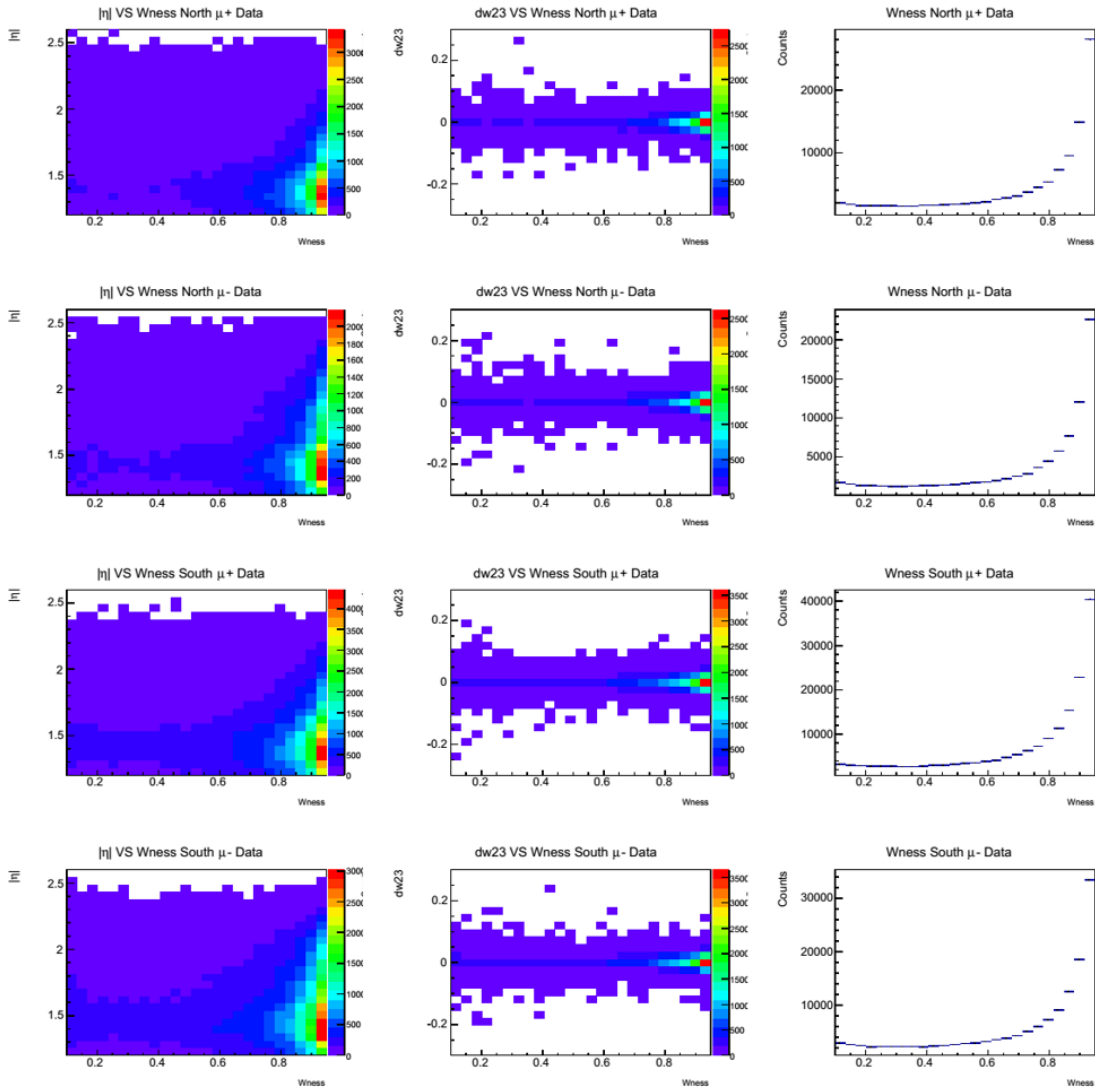


Figure 6.14: The first column of plots is  $\eta$  plotted as a function of  $W_{ness}$  where we see a 2D histogram of the even distribution. The middle column is  $dw_{23}$  as a function of  $W_{ness}$ , and the right column is a simple histogram of  $W_{ness}$ . The rows all correspond to the same arm and charge. From top to bottom: North,  $\mu^+$ , North  $\mu^-$ , South  $\mu^+$ , North  $\mu^-$ . Distributions shown here are all from simulated W-genic data set.

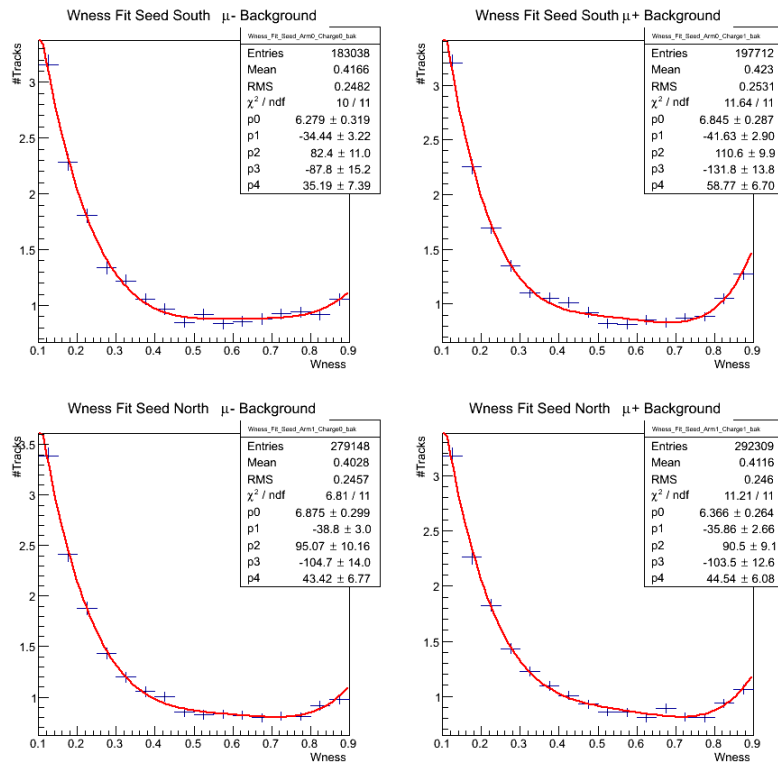


Figure 6.15: A summary of the fourth degree polynomial fit (Equation 6.7) to the  $W_{ness}$  distribution from the physics dataset in the background region.

We then model the other element of the distribution  $g(W_{ness}, dw_{23})$  as a co-axial double Gaussian. We allow the Parameters of the co-axial double Gaussian to vary linearly with  $W_{ness}$ , as seen below:

$$\sigma_1 = P_1 + P_3 \times W_{ness} \quad C_g = P_6 + P_7 \times W_{ness} \quad (6.8)$$

$$\sigma_2 = P_4 + P_5 \times W_{ness} \quad \mu = P_0 + P_1 \times W_{ness} \quad (6.9)$$

$$g(W_{ness}, dw_{23}) = C_w \times \left( \left( \frac{1}{\sqrt{2\pi}\sigma_1 + C_g\sqrt{2\pi}\sigma_2} \right) \times \left( e^{\frac{1}{2}\left(\frac{dw_{23}-\mu}{\sigma_1}\right)^2} + C_g e^{\frac{1}{2}\left(\frac{dw_{23}-\mu}{\sigma_2}\right)^2} \right) \right) \quad (6.10)$$

We seed these linearized parameters by taking slices of  $dw_{23}$  in  $W_{ness}$  and then fitting this slice with a co-axial double Gaussian. The parameters of the results of these fits are then plotted against the value of the  $W_{ness}$  slice, and fit with a line. These parameters are then used to seed the fit of Equation 6.6 to the physics data set. Fits to the individual slices of  $dw_{23}$  are summarized in Figure 6.16. The results of the co-axial double Gaussian parameters as functions of  $W_{ness}$  slice are shown in Figure 6.17.

The results of this fitting procedure are summarized in Figure 6.18.

Finally, the extrapolation of  $dw_{23}$  was reproduced independently by four separate analyzers, Daniel, Abraham, Ralf and Myself, with distributions lining up very closely, Figure 6.20

The PDF for  $\eta$  was obtained by creating a histogram of the variable for events tagged with  $W_{ness} < 0.9$ .

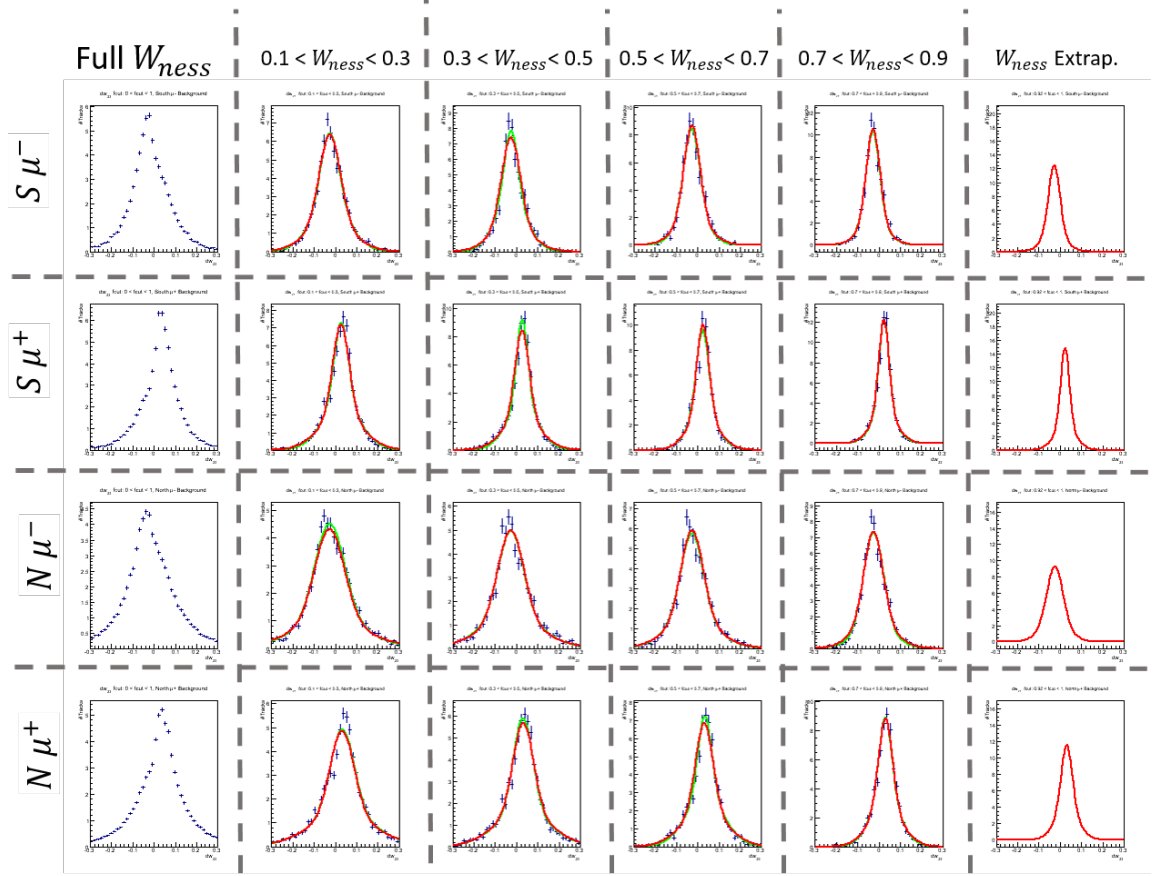


Figure 6.16: From left to right the columns are:  $d\omega_{23}$  for the full  $W_{ness}$  range,  $0.1 < W_{ness} < 0.3$ ,  $0.3 < W_{ness} < 0.5$ ,  $0.5 < W_{ness} < 0.7$ ,  $0.7 < W_{ness} < 0.9$ , and finally the extrapolated shape for  $W_{ness} > 0.95$ . In red, we see the 1D projection of the 2D distribution to the slice. This overlays a green curve, which is a fit done independently to a slice. The rows are labeled with the Arm and charge corresponding to the subdivided dataset. As you can see, the matching is often exact, between green and red curves. As the final column is the extrapolation, there is no slice-fit.

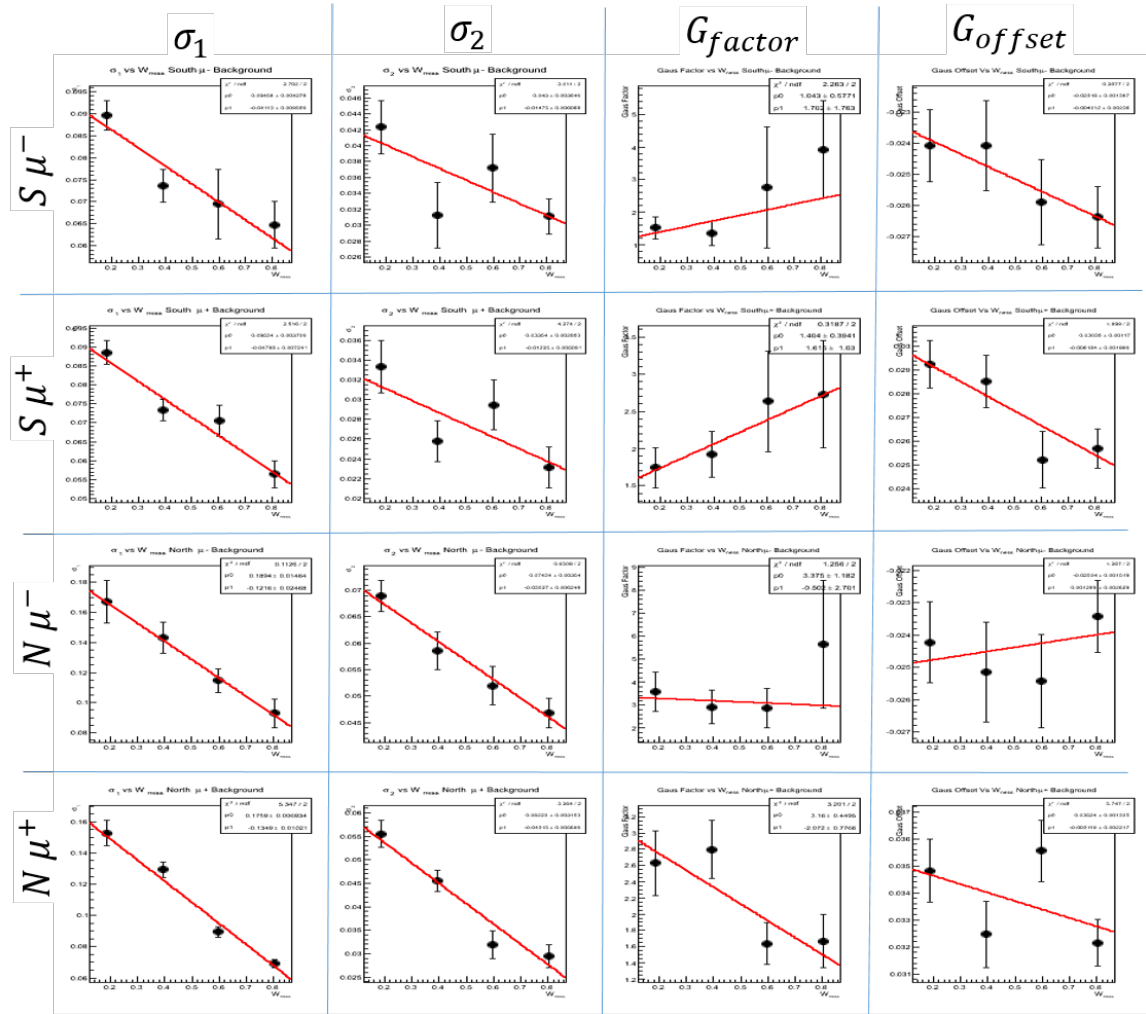


Figure 6.17: The four parameters from the co-axial Gaussian parameterization of  $dw_{23}$  as a function of  $W_{\text{ness}}$ . Though some parameters ( $G_{\text{factor}}, N\mu^-$ ) may appear to be non-linear, note that the uncertainty on some bins is quite large. Rows are arm/charge, labeled on the left, while columns are co-axial Gaussian parameters, summarized in Equation 6.10

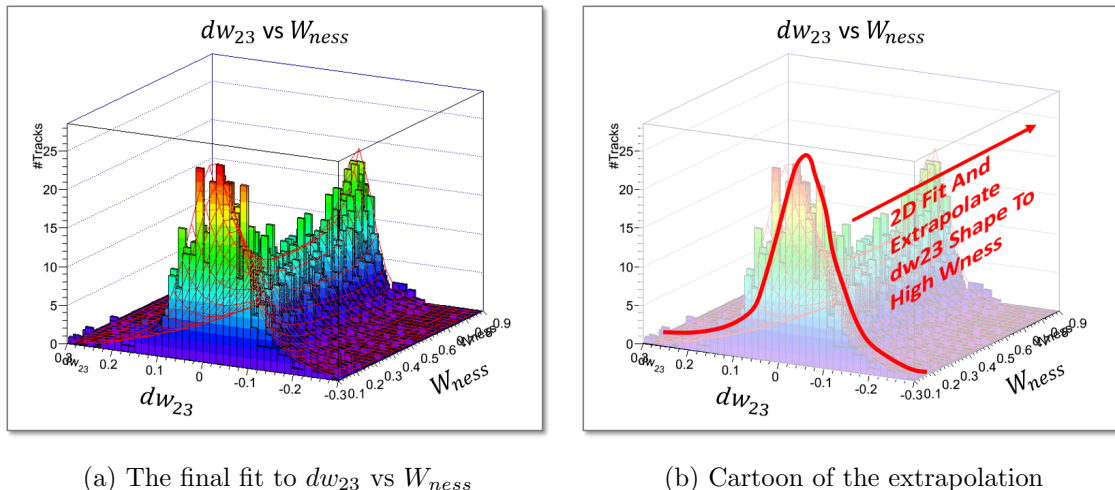


Figure 6.18: The red wire-frame is the resultant fit of to the  $dw_{23}$  vs  $W_{ness}$  distribution. We extrapolate the shape of  $dw_{23}$  to the signal region to obtain the hadronic background PDF for  $dw_{23}$ .

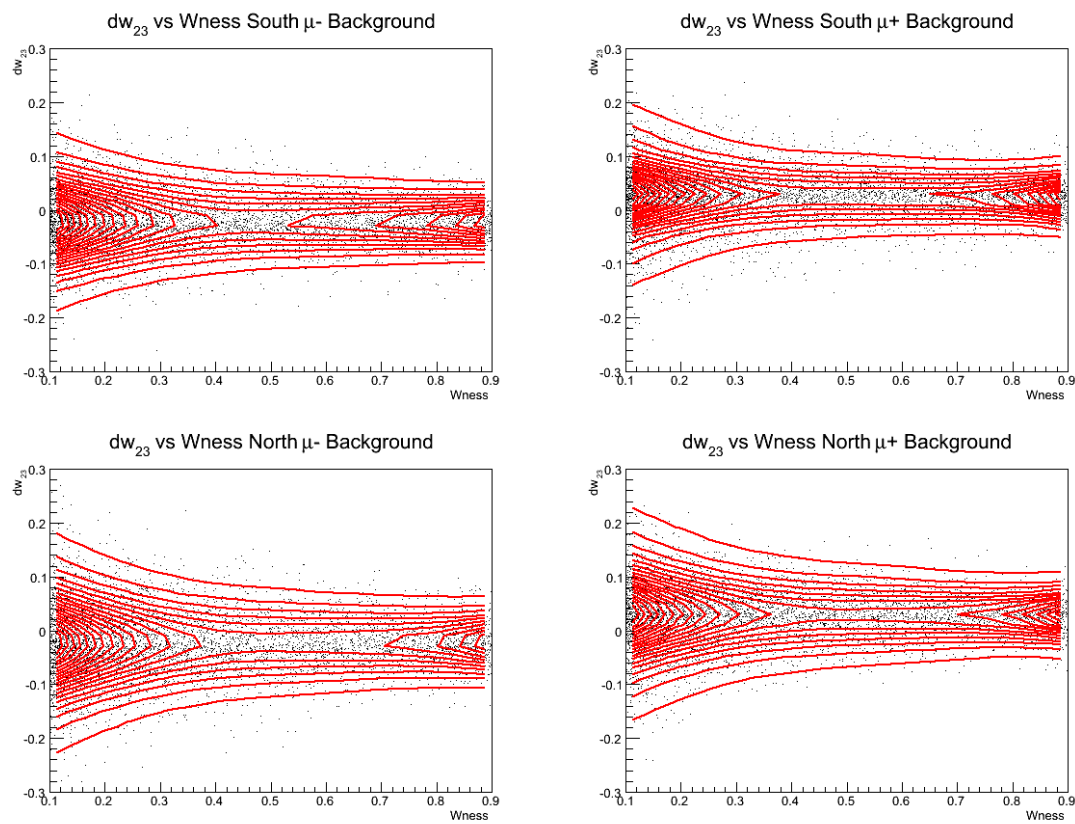


Figure 6.19: An overhead view of the various results of the  $dw_{23}$  vs  $W_{ness}$  fit for each arm and charge combination.

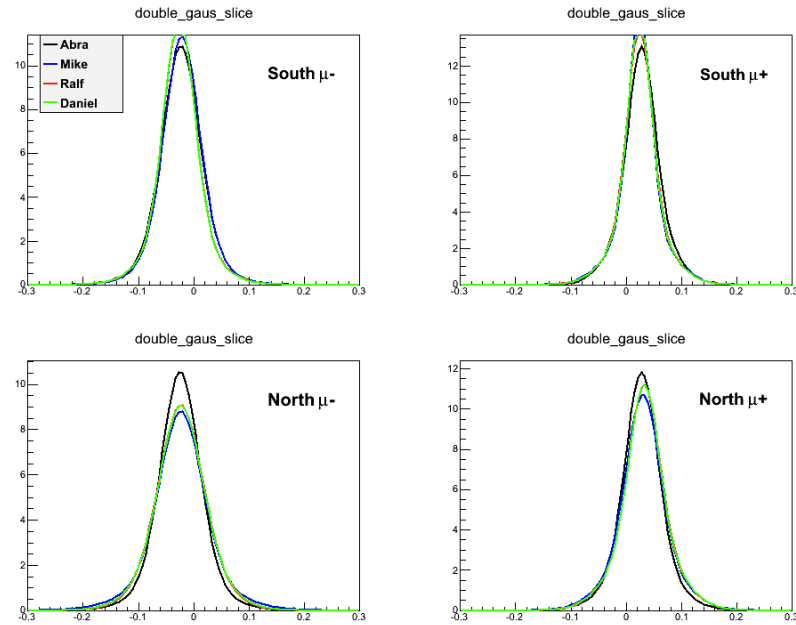


Figure 6.20: Abraham, Mike, Ralf and Daniel all independently parameterized and extrapolated  $dw_{23}$  obtaining consistent results. Figure prepared by Dr. Francesca Giordano [27]

### 6.4.2 Muon Background and W-Signal PDFs

The muon background probability density functions and the W-Signal probability density functions must be carefully summed from simulations so as to match the likely composition of the data set. This is done by using the well known cross-section of each of the processes which are simulated and normalizing with the integrated luminosity delivered to PHENIX during the 2013 run of RHIC. This luminosity was found to be  $277\text{pb}^{-1}$ .

One caveat is that the minimum bias trigger of PHENIX is easily fooled by effects such as pile-up and multiple collisions. Concretely, this occurs when there is more than one collision in a single bunch crossing. This is typically not a problem when PHENIX operates at lower energies and beam luminosities, but for this data set, it was a real factor, that must be corrected for, else all the ingredients in the muon background cocktail will be present in the wrong amounts and we'll get the wrong answer from using them. Pile up refers to the process where some events aren't read out quickly enough, and so one recorded event will contain information for two actual beam crossings. Unaccounted for, pile-up and multiple collisions both have the affect of lowering the measured luminosity.

The  $277\text{pb}^{-1}$  luminosity figure has been corrected for pile-up and multiple collisions. This is a separate analysis, done by my colleagues working on this analysis, so it will not be described in detail in this thesis, however it is described in detail in our analysis note: [27].

Finally, the PDFs used in the EULMF are shown in Figures 6.21-6.24.

With all PDFs prepared, we can perform the extended unbinned maximum likelihood fit, and extract the yields for the number of signal muons, and the number of fake hadronic background muons (recalling that the number of muon background muons are fixed).

The signal to background ratio extraction is summarized by each analyzer in Table ??, for the South Arm  $\mu-$  (the canonical cross check).

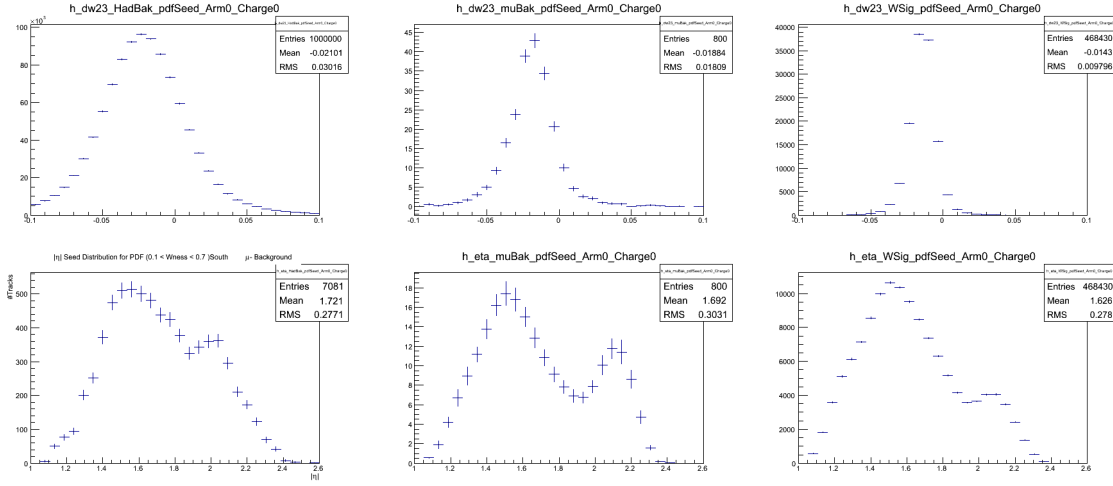


Figure 6.21: Left Column: The hadronic background PDFs, Middle Column: The Summed Muon Background PDFs, Right Column: The W-Signal PDF. For South Arm,  $\mu+$

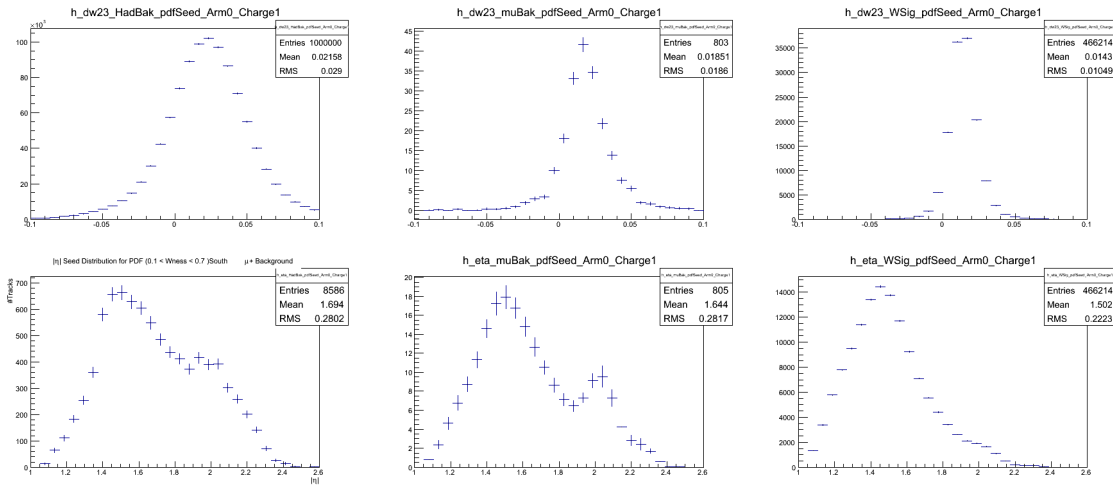


Figure 6.22: Left Column: The hadronic background PDFs, Middle Column: The Summed Muon Background PDFs, Right Column: The W-Signal PDF. For South Arm,  $\mu-$

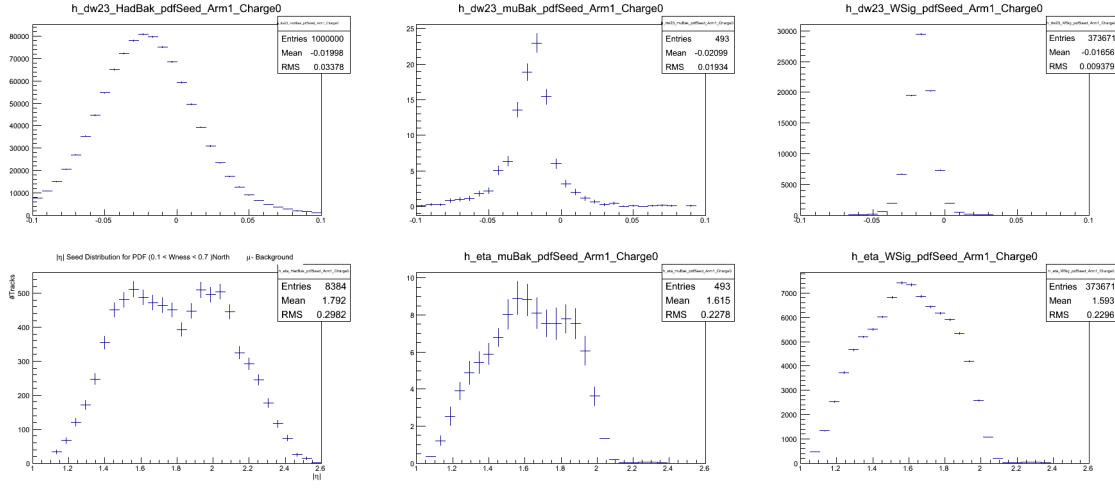


Figure 6.23: Left Column: The hadronic background PDFs, Middle Column: The Summed Muon Background PDFs, Right Column: The W-Signal PDF. For North Arm,  $\mu^-$

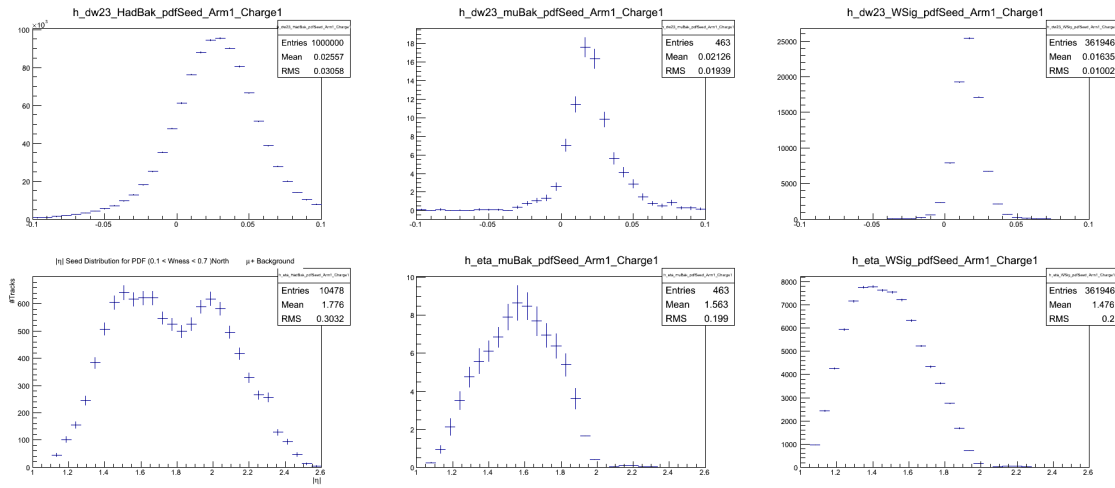


Figure 6.24: Left Column: The hadronic background PDFs, Middle Column: The Summed Muon Background PDFs, Right Column: The W-Signal PDF. For South Arm,  $\mu^+$

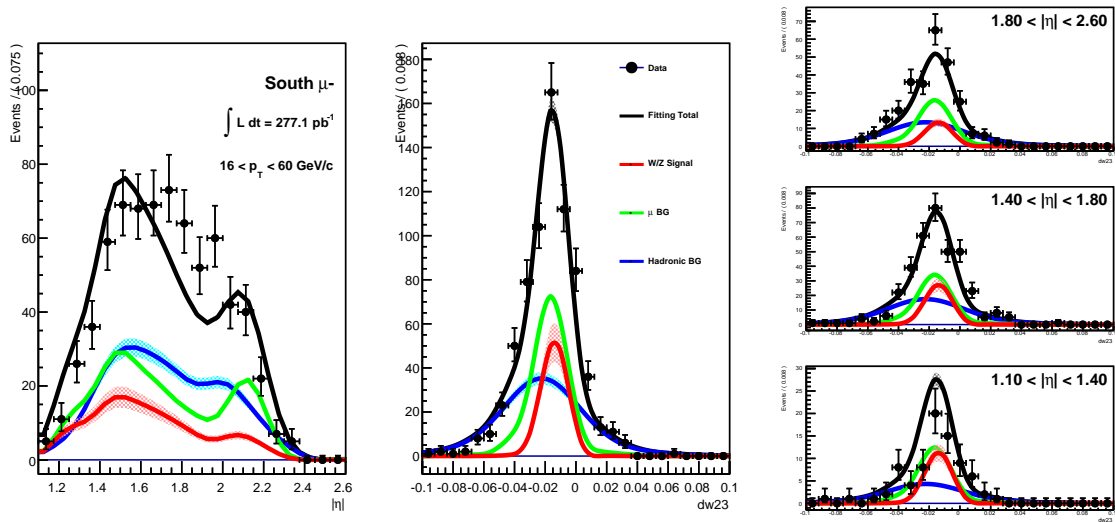


Figure 6.25: Here, we see the preliminary results of the EULMF for the 2013 Run. On the left,  $\eta$  is shown. In the middle,  $dw_{23}$ . On the right,  $dw_{23}$  is subdivided into the three standard  $\eta$  bins. In all cases, we see the unbinned data in black (with error bars), and the sum of the three fits in black. In Blue, we can see the fake-muon hadronic background. In Green, the muon background. In blue, we see the W-Signal result. The area under the curves represents the yield, relative to the total. Figure prepared by Dr. Ralf Seidl [27]. Shown: South Arm,  $\mu-$

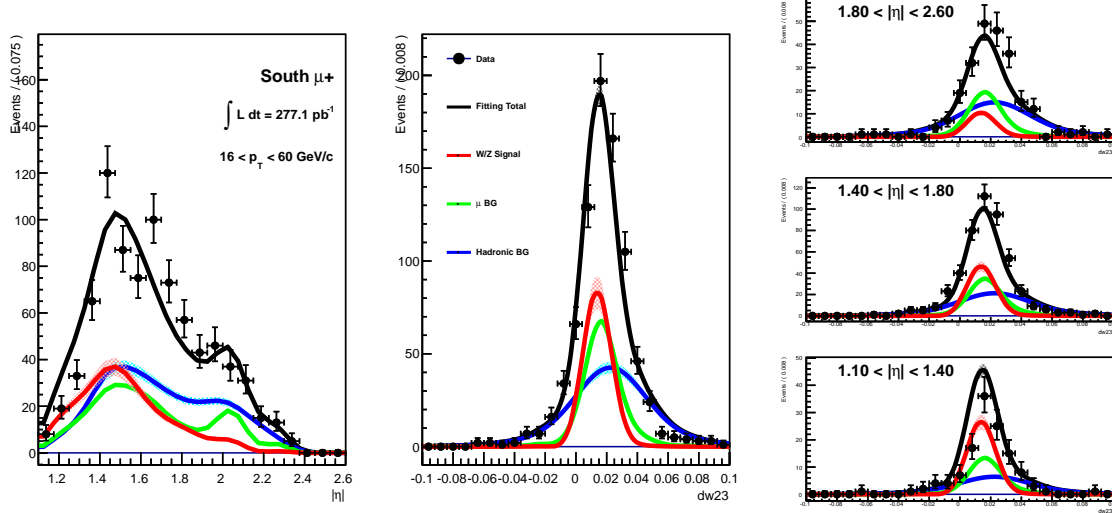


Figure 6.26: Here, we see the preliminary results of the EULMF for the 2013 Run. On the left,  $\eta$  is shown. In the middle,  $dw_{23}$ . On the right,  $dw_{23}$  is subdivided into the three standard  $\eta$  bins. In all cases, we see the unbinned data in black (with error bars), and the sum of the three fits in black. In Blue, we can see the fake-muon hadronic background. In Green, the muon background. In blue, we see the W-Signal result. The area under the curves represents the yield, relative to the total. Figure prepared by Dr. Ralf Seidl [27]. Shown: South Arm,  $\mu^+$

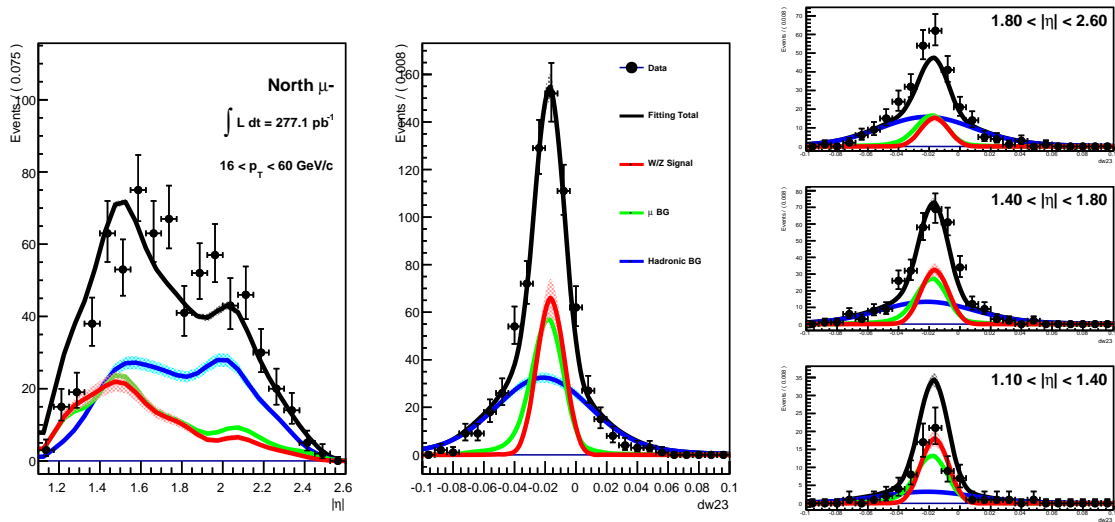


Figure 6.27: Here, we see the preliminary results of the EULMF for the 2013 Run. On the left,  $\eta$  is shown. In the middle,  $dw_{23}$ . On the right,  $dw_{23}$  is subdivided into the three standard  $\eta$  bins. In all cases, we see the unbinned data in black (with error bars), and the sum of the three fits in black. In Blue, we can see the fake-muon hadronic background. In Green, the muon background. In blue, we see the W-Signal result. The area under the curves represents the yield, relative to the total. Figure prepared by Dr. Ralf Seidl ???. Shown: North Arm,  $\mu^-$

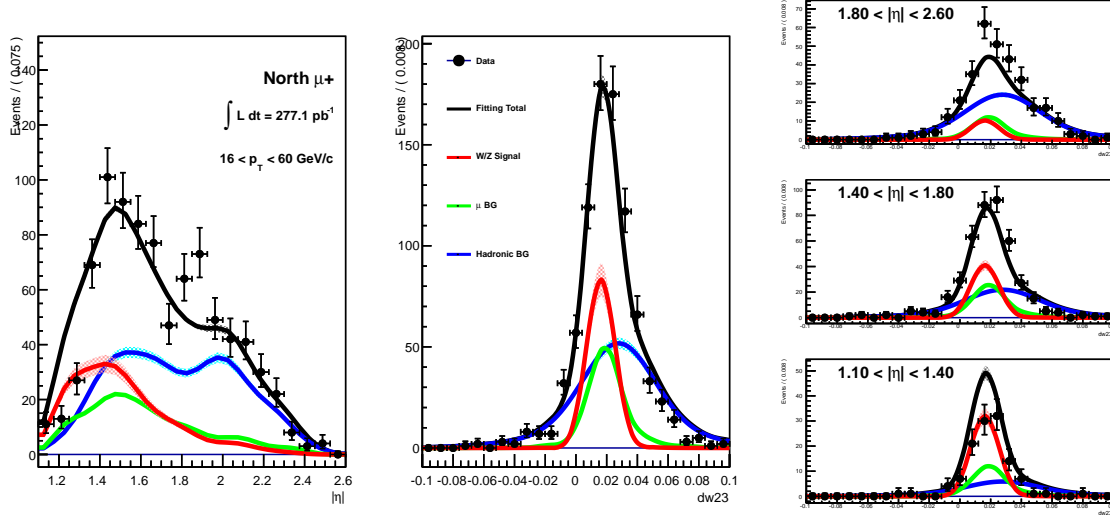


Figure 6.28: Here, we see the preliminary results of the EULMF for the 2013 Run. On the left,  $\eta$  is shown. In the middle,  $dw_{23}$ . On the right,  $dw_{23}$  is subdivided into the three standard  $\eta$  bins. In all cases, we see the unbinned data in black (with error bars), and the sum of the three fits in black. In Blue, we can see the fake-muon hadronic background. In Green, the muon background. In blue, we see the W-Signal result. The area under the curves represents the yield, relative to the total. Figure prepared by Dr. Ralf Seidl ???. Shown: North Arm,  $\mu^+$

Variable	South $\mu^-$			
	Ralf	Daniel	Mike	Abraham
Total events	2032	2034	2022	2039
Signal events	$340^{+42.14}_{-41.42}$	$303^{+42.31}_{-41.59}$	$332^{+42.28}_{-41.58}$	$294^{+41.38}_{-41.38}$
Hadron events	$1424^{+53.57}_{-52.60}$	$1469^{+54.55}_{-53.59}$	$1433^{+53.97}_{-52.99}$	$1485^{+53.85}_{-53.85}$
Muon events	269	262	257	259
Signal/BG	$0.20^{+0.03}_{-0.03}$	$0.18^{+0.00}_{-0.00}$	$0.20^{+0.03}_{-0.03}$	$0.17^{+0.02}_{-0.00}$

Table 6.5: South arm  $W \rightarrow \mu^-$  fit results per analyzer [27]

## 6.5 Systematic Tests

One of the rare advantages of this analysis was that I had the opportunity to undertake it in parallel with others, working as a team to accomplish our goals. That means that we were able perform many systematic tests. These tests are summarized in the appendix, and serve to lend confidence to our extraction of the signal to background ratio.

Arm	Charge	Total Events	Signal Events	Fake Muons	Muon Background	SBR
S	$\mu^-$	2023	$354^{+41.9714}_{-41.2598}$	$1448^{+53.6777}_{-52.7162}$	$2210^{+212103}_{-0263482}$	0.0258992
	$\mu^+$	2468	$498^{+44.0941}_{-43.2297}$	$1767^{+57.046}_{-56.3006}$	$2030^{+0238242}_{-02338242}$	0.0233755
N	$\mu^-$	2029	$370^{+34.4599}_{-33.7046}$	$1555^{+48.5042}_{-47.6586}$	$1040^{+0223026}_{-0219055}$	0.0214353
	$\mu^+$	2633	$505^{+37.9628}_{-37.2192}$	$2043^{+54.5676}_{-53.7571}$	$850^{+237312}_{-0189323}$	0.0185715

Table 6.6: A summary table from the results of the EULMF to the unbinned data set, summed to one  $\eta$  bin per arm and charge.

# Chapter 7

## Spin Analysis

### 7.1 Overview

The overall goal of this analysis is to arrive at a calculation of our observable,  $A_L$ . As discussed in Chapter 3,  $A_L$  is an important probe for the polarized parton distribution functions describing the quarks and anti-quarks of the proton sea-quark population. There is nothing magical about  $A_L$  - it just so happens that when we construct the asymmetry, using the cross-sections for a particular process, those cross-sections can be written in two ways:

1. Write it in terms of the machine luminosity and the number of events of a particular type observed
2. Calculate the scattering amplitude for the process, and then the cross-section of the process. Write down the cross-section in terms of experimental observables.

Thus, our strategy is clear - we have several well established theoretical frameworks with a number of degrees of freedom (i.e. item 2), so as experimentalists, we contribute by measuring the cross-section of the  $W \rightarrow \mu$  process, and calculating the observable via the strategy in item 1, which is then fed back into the models in order to reduce the degrees of freedom and arrive at a more correct model. These models are typically expressed as global QCD fits to world data over a wide kinematic range, and our contribution from PHENIX will help constrain the models, therefore giving a more accurate prediction of how much proton spin we can attribute to coming from the sea-quark polarization.

The Spin Analysis is very much 'turning the crank', we have already done the hard part of the analysis in Chapter 6 and Chapter 5. Lets not neglect too, the monumental task of building a RHIC and a PHENIX. The fact that particle physics can even be done in the first place, is absolutely astounding to me - the amount of infrastructure, technical expertise, collaboration, financial and intellectual capital needed to build such an enormous and precise machine is something that is very difficult to communicate. So, assuming that the other parts of this massive undertaking have been pulled off without a hitch, the actual machinery of the Spin Analysis only relies on three items:

1. What is the total beam polarization?
2. What is the polarization of the blue bunch, and yellow bunch at the time of each beam-beam interaction which generated a W-genic muon?
3. What is the total yield of  $\mu$ 's at forward and backward rapidity, for positive and negative charge?

$A_L$  is then calculated:

$$A_L = \frac{d\sigma^{\Rightarrow} - d\sigma^{\Leftarrow}}{d\sigma^{\Rightarrow} + d\sigma^{\Leftarrow}} \quad (7.1)$$

Where  $d\sigma$  is experimentally calculated as:

$$\sigma = \frac{1}{\mathcal{L}} \dot{N} \quad (7.2)$$

With  $\Rightarrow$  or  $\Leftarrow$  referring to tracks which come from positive( $\Rightarrow$ ) or negative( $\Leftarrow$ ) helicities relative to the initial proton polarization state.  $\mathcal{L}$  refers to the beam luminosity, a property of the colliding beams, and  $\dot{N}$  refers to the production rate of W-genic muons. Naturally, this calculation is done for forward and backward rapidities for positive and negative charges. Since we can measure  $W \rightarrow \mu$  for  $W+$  or  $W-$  at forward or backward rapidities, we treat everything separately, and combine forward and backward rapidity data to get the final answer for  $A_L^{W+}$  and  $A_L^{W-}$  at forward, and backward rapidity.

In practice, we do not calculate cross-sections for  $W \rightarrow \mu$  for the purposes of evaluating  $A_L$ , as we really only need the yields, since in principal  $\mathcal{L}$  will be a common factor in all cross-sections and cancel out. This of course comes with major caveats -  $\mathcal{L}$  only cancels out if the relative luminosity of each polarization condition is the same - spin patterns

are chosen so that in theory, this happens. This of course is checked. Experimentally, we construct raw asymmetries (simple differences/sums) of the relevant muon yields ( $\epsilon_L$ ), and correct the overall raw asymmetry for less than 100% beam polarization and the dilution from the signal-to-background ratio.

## 7.2 Measured Beam Polarization

Formally, we obtain the beam polarization from the p-Carbon scattering experiments done every fill, and spin database QA. The polarization of the beams for each fill are measured at the beginning and end of every fill. This was described in Section 4.3. The results of the polarization study and spin database QA are all stored in a PostgreSQL database, indexed by run number (multiple runs are taken in each fill).

The polarization of the blue and yellow beams over the Run 13 run are summarized in Figure 7.1.

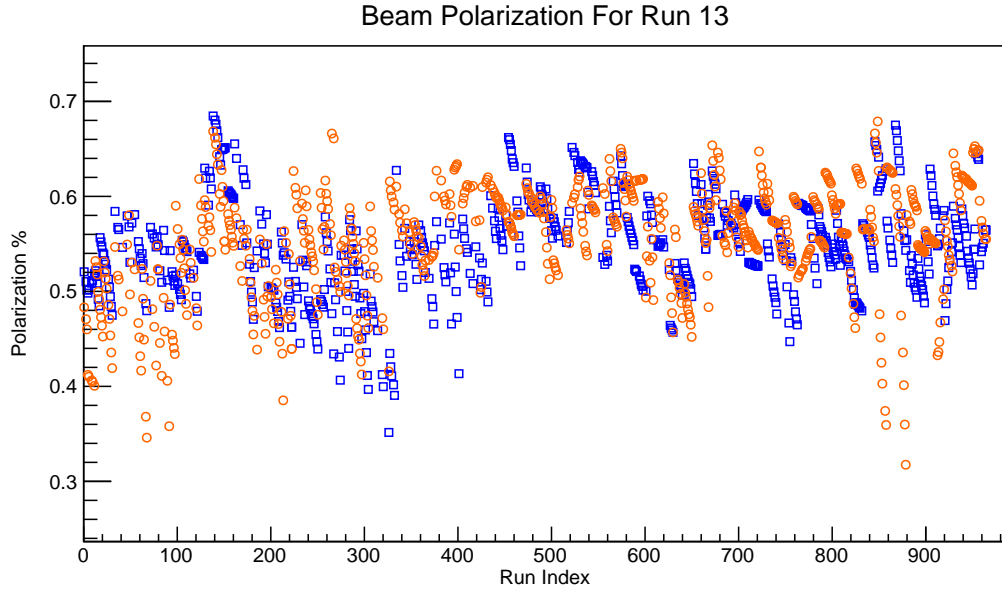


Figure 7.1: Shown: the average beam polarization per run over the course of the 2013 data set. All of the runs in the analysis were indexed from 0 to approximately 1000, and plotted in the order that they were taken. The blue open circles are from the blue beam, the yellow open circles are for the yellow beam.

The polarization over the whole of Run 13 was well over 50% for the majority of the run, with a few poorly polarized runs. This can be accounted for, by calculating an asymmetry for every single run, and weighting that asymmetry with that run's polarization, but it was found that the result was unchanged. This kind of approach would improve things if the polarization was inconsistent, though as evident in Figure 7.1, it was relatively consistent (even improving, generally towards the end of the 2013), distributions of the polarization is summarized in Figure 7.2.

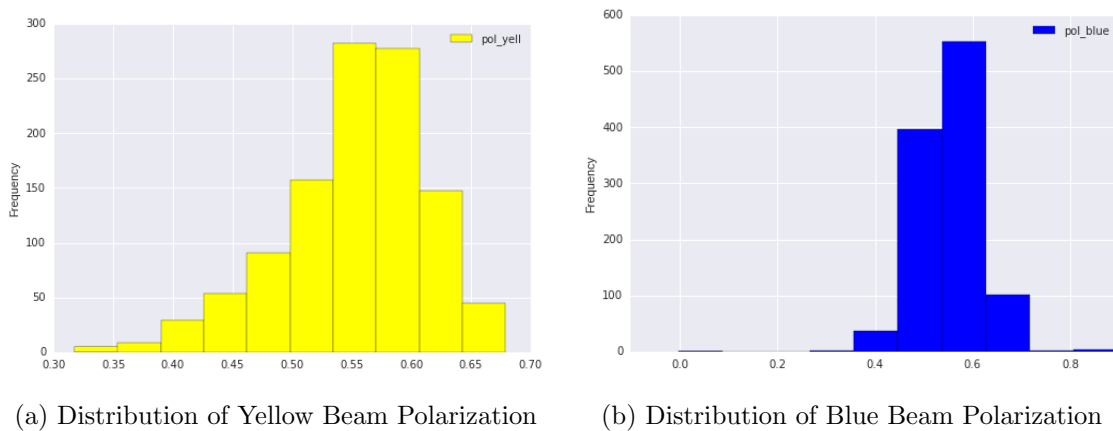


Figure 7.2: The blue beam had a tighter polarization distribution, peaked at just about 50% polarization, whereas the yellow beam's polarization distribution was broader, still peaking at about 55%.

The other major element to the Spin Analysis is determining with what confidence we can assign to our understanding of the polarization pattern filled into the blue and yellow beams.

### 7.3 Spin Patterns

In the 2013 Run Period, I was in charge of the PHENIX spin quality assurance while the detector was actively taking data. As part of this work it was my job to maintain the monitoring software as well as confirm that physics fills were 'polarization-ready'. PHENIX uses a numbering system identify which bunch in the blue beam collides with another bunch from the yellow beam. Blue bunch "0" collides with yellow bunch "0" at the PHENIX interaction point, by definition. There are bunches in the blue, and yellow

beams which are left purposefully empty, which allows us to later reconstruct and confirm which bunch is colliding with which bunch, since if a filled bunch collides with an empty bunch, we will see no collisions for that event. PHENIX has a slight delay in its triggering electronics related to the time delay between the DAQ receiving the 'begin run' event and the first 'data event'. This delay is exactly five bunch-crossings in length, so when data is reconstructed, recorded bunch crossing numbers in the data stream will be off by 5. We can look at the BBC rate as a function of bunch crossing for a data set to identify, and correct this crossing-shift, which is done in the offline spin data QA.

In the 2013 data taking period, RHIC provided sixteen different bunch patterns - the patterns were varied to help avoid any kind of systematic bias towards one bunch polarization over another. For the first half of the 2013 data period, each beam had two consecutive empty bunches, and a 10-bunch long empty 'abort-gap'. The abort gap is canonically set to occur at bunch number 109-119 (indexing from 0). The consecutive empty bunches occurred at position 68 and 69 in the yellow beam, and 28 and 29 in the blue beam.

Bunch patterns P1-P8 were used in the first half of the data taking period, with P21-P28 being used in the second half of the data taking period in Run 2013. Generally, the spin patterns were defined as a sub-pattern, which is then repeated until the last bunch in a given beam is reached.

The patterns are designed to run through as many permutations of bunch-bunch polarization conditions. The beams are transversely polarized '+' is up and '-' is down during the fill, but the polarizations are rotated towards PHENIX (longitudinally) immediately before collision. Crucially, the various collision conditions need to occur with the same relative frequency - so the patterns are designed to fulfill this requirement.

Two ways of visualizing the consistency of spin patterns include Figure 7.3, which shows, for all muon tracks after the basic cut, consistent fills. Additionally, if we count the various permutations of spin patterns, i.e. ++, -+, +-,-, such that the left character is the blue polarization and the right character is the yellow polarization, we would expect to see very similar yields for each polarization combination (we do), Figure 7.4.

Given that we have seen very consistent distributions of arm/charge, we can move forward confident that there is likely no dilution effects that stem from an excess of one-

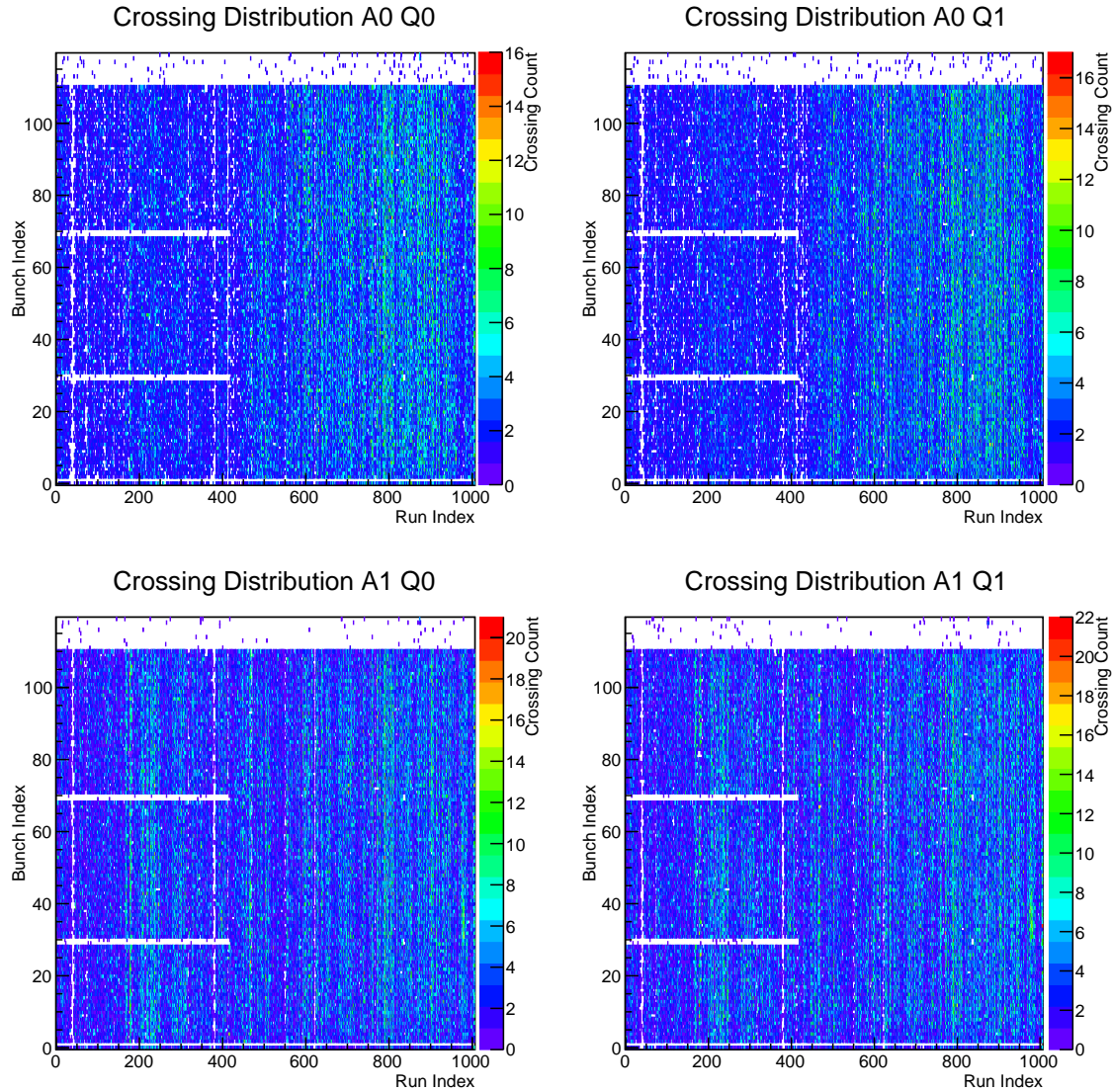


Figure 7.3: Here, we see the crossing distribution for every run taken for the 2013 data set. We use the typical code for arm/charge. The top row is for the South Arm. The bottom row is for the North Arm. The left column is for negative charge, the right column is for positive charge.

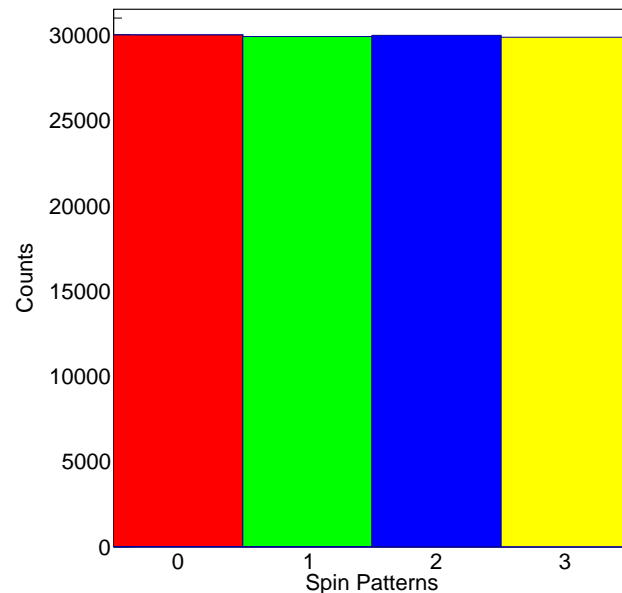


Figure 7.4: Here, we can see the yield for various crossing combinations as taken from the dataset itself, rather than the database. We see a very consistent distribution between the various possible crossing patterns. In this case, the horizontal axis is the crossing pattern code - 0:++, 1:-+, 2:+-, 3:--. Any slight difference between yields for each pattern is well below our experimental precision.

crossing pattern over another. Additionally, this is extensively studied in the yearly spin-database analysis note [70].

Pattern	Blue Pattern	Yellow Pattern
P1	++--	++--
P2	--++	--++
P3	+--+	+--+
P4	-++	-++
P5	+++	+--
P6	+++	++-
P7	--	--
P8	--	--
P21	+-	+-
P22	+-	+-
P23	-+ +	-+ +
P24	-+ +	-+ +
P25	-++	-++
P26	-++	-++
P27	++ -	++ -
P28	++ -	++ -

Table 7.1: Patterns P1-P8 were filled into RHIC for the first portion of the 2013 data taking period, with P21-P28 being filling in the second portion. For each pattern, from left to right, bunch 0 in the blue or yellow beam is filled with the leftmost polarization, with bunch 1 getting the next, and so on. The pattern repeats as soon as the end has been reached, until we get to the last filled bunch, with any empty bunch being ‘polarized’ as if it were not empty.

## 7.4 Muon Yields

To calculate  $A_L$ , we must obtain yields for positive and negative rapidity muons for all arm and charge conditions. Additionally, if we wish to further separate this data into  $\eta$  bins, this separation must be done as well. The number of 'groups' of muons grow combinatorially as expected with further subcategories. We will discuss how these yields are used to calculate raw-asymmetries, and subsequently full asymmetries in the next section.

We obtain yields for muons in the signal region (since this is the region for which we have calculated the signal-to-background ratio) by applying the standard  $W_{ness}$  cut to the physics data set, and then simply sorting the muons. The results of this are summarized in Table 7.4 (standard forward-backward binning), Table 7.2 (south arm, three eta bins), and Table 7.3 (north arm, three eta bins).

<b>South Arm</b>				
Charge	Helicity	$ \eta $	Range	$\mu$ Yield
-1	++	1.1 < $ \eta $ < 1.4		12
-1	++	1.4 < $ \eta $ < 1.8		67
-1	++	1.8 < $ \eta $ < 2.6		63
-1	-+	1.1 < $ \eta $ < 1.4		21
-1	-+	1.4 < $ \eta $ < 1.8		99
-1	-+	1.8 < $ \eta $ < 2.6		49
-1	+-	1.1 < $ \eta $ < 1.4		19
-1	+-	1.4 < $ \eta $ < 1.8		76
-1	+-	1.8 < $ \eta $ < 2.6		58
-1	--	1.1 < $ \eta $ < 1.4		14
-1	--	1.4 < $ \eta $ < 1.8		68
-1	--	1.8 < $ \eta $ < 2.6		57
-1	**	1.1 < $ \eta $ < 1.4		0
-1	**	1.4 < $ \eta $ < 1.8		0
-1	**	1.8 < $ \eta $ < 2.6		0
+1	++	1.1 < $ \eta $ < 1.4		28
+1	++	1.4 < $ \eta $ < 1.8		94
+1	++	1.8 < $ \eta $ < 2.6		50
+1	-+	1.1 < $ \eta $ < 1.4		26
+1	-+	1.4 < $ \eta $ < 1.8		96
+1	-+	1.8 < $ \eta $ < 2.6		41
+1	+-	1.1 < $ \eta $ < 1.4		22
+1	+-	1.4 < $ \eta $ < 1.8		124
+1	+-	1.8 < $ \eta $ < 2.6		47
+1	--	1.1 < $ \eta $ < 1.4		26
+1	--	1.4 < $ \eta $ < 1.8		97
+1	--	1.8 < $ \eta $ < 2.6		66
+1	**	1.1 < $ \eta $ < 1.4		0
+1	**	1.4 < $ \eta $ < 1.8		0
+1	**	1.8 < $ \eta $ < 2.6		0

Table 7.2: Due to much higher integrated luminosity of Run 13, we can actually subdivide the muon yields into rapidity bins for the purposes of trying to cover a wider kinematic range (at the expense of uncertainty). Here, we see the South arm’s yields for each helicity combination of colliding protons, with the polarization of the blue beam and yellow beams color coded in column 2. Recall that of the yields, about 20% are actual signal events.

North Arm				
Charge	Helicity	$ \eta $	Range	$\mu$ Yield
-1	++	1.1 < $ \eta $ < 1.4		18
-1	++	1.4 < $ \eta $ < 1.8		76
-1	++	1.8 < $ \eta $ < 2.6		57
-1	-+	1.1 < $ \eta $ < 1.4		14
-1	-+	1.4 < $ \eta $ < 1.8		63
-1	-+	1.8 < $ \eta $ < 2.6		56
-1	+-	1.1 < $ \eta $ < 1.4		13
-1	+-	1.4 < $ \eta $ < 1.8		74
-1	+-	1.8 < $ \eta $ < 2.6		61
-1	--	1.1 < $ \eta $ < 1.4		19
-1	--	1.4 < $ \eta $ < 1.8		63
-1	--	1.8 < $ \eta $ < 2.6		65
-1	**	1.1 < $ \eta $ < 1.4		0
-1	**	1.4 < $ \eta $ < 1.8		0
-1	**	1.8 < $ \eta $ < 2.6		0
+1	++	1.1 < $ \eta $ < 1.4		24
+1	++	1.4 < $ \eta $ < 1.8		96
+1	++	1.8 < $ \eta $ < 2.6		60
+1	-+	1.1 < $ \eta $ < 1.4		30
+1	-+	1.4 < $ \eta $ < 1.8		95
+1	-+	1.8 < $ \eta $ < 2.6		64
+1	+-	1.1 < $ \eta $ < 1.4		27
+1	+-	1.4 < $ \eta $ < 1.8		68
+1	+-	1.8 < $ \eta $ < 2.6		64
+1	--	1.1 < $ \eta $ < 1.4		33
+1	--	1.4 < $ \eta $ < 1.8		99
+1	--	1.8 < $ \eta $ < 2.6		56
+1	**	1.1 < $ \eta $ < 1.4		0
+1	**	1.4 < $ \eta $ < 1.8		0
+1	**	1.8 < $ \eta $ < 2.6		0

Table 7.3: Due to much higher integrated luminosity of Run 13, we can actually subdivide the muon yields into rapidity bins for the purposes of trying to cover a wider kinematic range (at the expense of uncertainty). Here, we see the North arm’s yields for each helicity combination of colliding protons, with the polarization of the blue beam and yellow beams color coded in column 2. Recall that of the yields, about 20% are actual signal events.

<b>Arm</b>	<b>Charge</b>	<b>Helicity</b>	$\mu$	<b>Yield</b>
S	-1	++	142	
S	-1	-+	169	
S	-1	+-	153	
S	-1	--	139	
S	-1	**	0	
S	+1	++	172	
S	+1	-+	163	
S	+1	+-	193	
S	+1	--	189	
S	+1	**	0	
N	-1	++	151	
N	-1	-+	133	
N	-1	+-	148	
N	-1	--	147	
N	-1	**	0	
N	+1	++	180	
N	+1	-+	189	
N	+1	+-	159	
N	+1	--	188	
N	+1	**	0	

Table 7.4: As a consistency check to previous analysis which only had enough statistics for two  $\eta$  bins, one forward, and one backward for  $A_L^{W+}$ , we have binned the data to match. Here, we see a division of the data by arm, charge, and helicity combination, which is color-coded for the polarization of the blue and yellow beams. Note that of the yields, only  $\sim 20\%$  of the yield comes from a W-Boson decay.

## 7.5 Calculation of $\epsilon_L$ and $A_L$ for $W \rightarrow \mu$

### 7.5.1 Asymmetry Calculation

### 7.5.2 Discussion of Work Done By Analysis Team

## 7.6 Data Validation

Mention Daniel's GPR, Ralf's PEPSI, Abraham's FVTX work, and Francesca's cross-checks.

### 7.6.1 Simulations and The Signal to Background Ratio

### 7.6.2 Gaussian Process Regression

### 7.6.3 Four Way Cross Validation

### 7.6.4 Asymmetry Consistency Check

### 7.6.5 Beam Polarization

### 7.6.6 Beam Luminosity

### 7.6.7 Code Cross Validation

# **Chapter 8**

## **The Vernier Analysis**

**8.1 Overview**

**8.2 Analysis Note Here**

**8.3 W Cross Section**

## **Chapter 9**

## **Discussion and Conclusion**

# Bibliography

- [1] J Ashman, Others, B Badelek, G Baum, I G Bird, A W Edwards, and T Walcher. A Measurement Of The Spin Asymmetry And Determination Of The Structure Function \textit{g1} In Deep Inelastic Muon-Proton Scattering. *Phys. Lett. B*, 206(2):364–370, 1988.
- [2] Herbert S. Long. The Unity of Empedocles' Thought. *The American Journal of Philology*, 70(2):142–158, 1949.
- [3] Craig Freudenrich. Combined Atomic Orbital, 2001.
- [4] Manisearch. scale\_of\_matter, 2010.
- [5] Marco Stratmann. Spin physics at rhic - a theoretical overview. Technical report, 2009.
- [6] Arthur Steward Eve. *Rutherford: Being the Life and Letters of the Rt. Hon. Lord Rutherford, O. M.* The University Press, 1939.
- [7] Kurzon. Diagram Illustratng Geiger-Marsden Experiment, 2014.
- [8] Bruxelles Benjamin Croupie. Participants of the 5th Solvay Congress. Technical report, 1927.
- [9] Wikimedia. Hideki Yukawa. *The Mainichi Graphic*, sep 1952.
- [10] FNAL. Fermi National Lab Bubble Chamber, 2005.
- [11] ENERGY.GOV. Bubble Chamber Tracks, 1973.
- [12] Ddn2. Electron Proton Deep Inelastic Scattering, 2008.
- [13] Latham Boyle. standard\_model\_complete, 2014.
- [14] a. Accardi, J. L. Albacete, M. Anselmino, N. Armesto, E. C. Aschenauer, A. Bacchetta, D. Boer, W. K. Brooks, T. Burton, N. B. Chang, W. T. Deng, A. Deshpande, M. Diehl, A. Dumitru, R. Dupré, R. Ent, S. Fazio, H. Gao, V. Guzey, H. Hakobyan, Y. Hao, D. Hasch, R. Holt, T. Horn, M. Huang, A. Hutton, C. Hyde, J. Jalilian-Marian, S. Klein, B. Kopeliovich, Y. Kovchegov, K. Kumar, K. Kumerički, M. A. C. Lamont, T. Lappi, J. H. Lee, Y. Lee, E. M. Levin, F. L. Lin, V. Litvinenko, T. W.

- Ludlam, C. Marquet, Z. E. Meziani, R. McKeown, A. Metz, R. Milner, V. S. Morozov, A. H. Mueller, B. Müller, D. Müller, P. Nadel-Turonski, A. Prokudin, V. Ptitsyn, X. Qian, J. W. Qiu, M. Ramsey-Musolf, T. Roser, F. Sabatié, R. Sassot, G. Schnell, P. Schweitzer, E. Sichtermann, M. Stratmann, M. Strikman, M. Sullivan, S. Taneja, T. Toll, D. Trbojevic, T. Ullrich, R. Venugopalan, S. Vigdor, W. Vogelsang, C. Weiss, B. W. Xiao, F. Yuan, Y. H. Zhang, L. Zheng, H. Paukkunen, A. Prokudin, V. Ptitsyn, X. Qian, J. W. Qiu, M. Ramsey-Musolf, T. Roser, F. Sabatié, R. Sassot, G. Schnell, P. Schweitzer, E. Sichtermann, M. Stratmann, M. Strikman, M. Sullivan, S. Taneja, T. Toll, D. Trbojevic, T. Ullrich, R. Venugopalan, S. Vigdor, W. Vogelsang, C. Weiss, B. W. Xiao, F. Yuan, Y. H. Zhang, and L. Zheng. Electron Ion Collider: The Next QCD Frontier - Understanding the glue that binds us all. *arXiv preprint*, page 164, 2012.
- [15] Christine Aidala and Et Al. Research Plan for Spin Physics at RHIC. *report to DOE*, 2005.
- [16] Wolfram Fischer. RHIC Run Overview, 2016.
- [17] Karen Walsh and Peter Genzer. BNL Newsroom — Hot Nuclear Matter Featured in Science, 2012.
- [18] Brookhaven National Laboratory and Anatoli Zelenski. Towards 100% polarization in the Optically-Pumped Polarized Ion Source at RHIC. Technical report, Brookhaven National Laboratory, 2007.
- [19] RHIC, I. Alekseev, C. Allgower, M. Bai, and Et Al. Configuration Manual Polarized Proton Collider at RHIC. *Configuration Manual*, (January), 2006.
- [20] John Haggerty, Martin Purschke, Chris Pinkenburg, and Ed Desmond. PHENIX Shift Duties, 2016.
- [21] Tomoaki Nakamura. Introduction to PHENIX Beam Beam Counter ( BBC ) Purpose of PHENIX BBC. Technical report, 2002.
- [22] C. Aidala, L. Anaya, E. Anderssen, A. Bambaugh, A. Barron, J. G. Boissevain, J. Bok, S. Boose, M. L. Brooks, S. Butsyk, M. Cepeda, P. Chacon, S. Chacon, L. Chavez, T. Cote, C. Dagostino, A. Datta, K. Deblasio, L. Delmonte, E. J. Desmond, J. M. Durham, D. Fields, M. Finger, C. Ging, B. Gonzales, J. S. Haggerty, T. Hawke, H. W. Van Hecke, M. Herron, J. Hoff, J. Huang, X. Jiang, T. Johnson, M. Jonas, J. S. Kapustinsky, A. Key, G. J. Kunde, J. Kurtz, J. Labounty, D. M. Lee, K. B. Lee, M. J. Leitch, M. Lenz, W. Lenz, M. X. Liu, D. Lynch, E. Mannel, P. L. McGaughey, A. Meles, B. Meredith, H. Nguyen, E. Obrien, R. Pak, V. Papavassiliou, S. Pate, H. Pereira, G. D N Perera, M. Phillips, R. Pisani, S. Polizzo, R. J. Poncione, J. Popule, M. Prokop, M. L. Purschke, A. K. Purwar, N. Ronzhina, C. L. Silva, M. Slune??ka, R. Smith, W. E. Sondheim, K. Spendier, M. Stoffer, E. Tennant, D. Thomas, M. Tom????ek, A. Veicht, V. Vrba, X. R. Wang, F. Wei, D. Winter, R. Yarema, Z. You, I. Younus, A. Zimmerman, and T. Zimmerman. The PHENIX forward silicon vertex detector. *Nuclear Instruments*

- and Methods in Physics Research, Section A: Accelerators, Spectrometers, Detectors and Associated Equipment*, 755:44–61, 2014.
- [23] Yoshinori Fukao. Forward upgrade for  $\langle i \rangle W \langle /i \rangle$  physics at the RHIC-PHENIX experiment. *Journal of Physics: Conference Series*, 295:012165, 2011.
  - [24] Mike Beaumier. *Probing the Spin Structure of the Proton Using Polarized Proton+Proton Collisions and the Production of W-Bosons*. PhD thesis, University of California, Riverside, 2016.
  - [25] Hideyuki Oide. *Measurement of longitudinal spin asymmetry in production of muons from W / Z boson decays in polarized p + p collisions at s = 500 GeV with the PHENIX detector at RHIC*. PhD thesis, 2012.
  - [26] PHENIX Collaboration. PHENIX Drawings.
  - [27] Ralf Seidl. PHENIX W to mu measurements in polarized proton-proton collisions. In *PoS (DIS2014) 205*, number May, 2014.
  - [28] K. Adcox, S. S. Adler, M. Aizama, N. N. Ajitanand, Y. Akiba, H. Akikawa, J. Alexander, A. Al-Jamel, M. Allen, G. Alley, R. Amirikas, L. Aphcetche, Y. Arai, J. B. Archuleta, J. R. Archuleta, R. Armendariz, V. Armijo, S. H. Aronson, D. Autrey, R. Averbeck, T. C. Awes, B. Azmoun, A. Baldisseri, J. Banning, K. N. Barish, A. B. Barker, P. D. Barnes, J. Barrette, F. Barta, B. Bassalleck, S. Bathe, S. Batsouli, V. V. Baublis, A. Bazilevsky, R. Begay, J. Behrendt, S. Belikov, R. Belkin, F. G. Bellaiche, S. T. Belyaev, M. J. Bennett, Y. Berdnikov, S. Bhagatnata, J. C. Biggs, A. W. Bland, C. Blume, M. Bobrek, J. G. Boissevain, S. Boose, H. Borel, D. Borland, E. Bosze, S. Botelho, J. Bowers, C. Britton, L. Britton, M. L. Brooks, A. W. Brown, D. S. Brown, N. Bruner, W. L. Bryan, D. Bucher, H. Buesching, V. Bumazhnov, G. Bunce, J. Burward-Hoy, S. A. Butsyk, M. M. Cafferty, T. A. Carey, J. S. Chai, P. Chand, J. Chang, W. C. Chang, R. B. Chappell, L. L. Chavez, S. Chernichenko, C. Y. Chi, J. Chiba, M. Chiu, S. Chollet, R. K. Choudhury, T. Christ, T. Chujo, M. S. Chung, P. Chung, V. Cianciolo, D. J. Clark, Y. Cobigo, B. A. Cole, P. Constantin, R. Conway, K. C. Cook, D. W. Crook, H. Cunitz, R. Cunningham, M. Cutshaw, D. G. D'Enterria, C. M. Dabrowski, G. Danby, S. Daniels, A. Danmura, G. David, A. Debraine, H. Delagrange, J. DeMoss, A. Denisov, A. Deshpande, E. J. Desmond, O. Dietzscht, B. V. Dinesh, J. L. Drachenberg, O. Drapier, A. Drees, R. du Rietz, A. Durum, D. Dutta, K. Ebisu, M. A. Echave, Y. V. Efremenko, K. El Chenawi, M. S. Emery, D. Engo, A. Enokizono, K. Enosawa, H. En'yo, N. Ericson, S. Esumi, V. A. Evseev, L. Ewell, O. Fackler, J. Fellenstein, T. Ferdousi, J. Ferrierra, D. E. Fields, F. Fleuret, S. L. Fokin, B. Fox, Z. Fraenkel, S. Frank, A. Franz, J. E. Frantz, A. D. Frawley, J. Fried, J. P. Freidberg, E. Fujisawa, H. Funahashi, S. Y. Fung, S. Gadrat, J. Gannon, S. Garpman, F. Gastaldi, T. F. Gee, R. Gentry, T. K. Ghosh, P. Giannotti, A. Glenn, A. L. Godoi, M. Gonin, G. Gogiberidze, J. Gosset, Y. Goto, R. Granier de Cassagnac, S. V. Greene, V. Griffin, M. Grosse Perdekamp, S. K. Gupta, W. Guryn, H. A. Gustafsson, T. Hachiya, J. S. Haggerty, S. Hahn, J. Halliwell, H. Hamagaki, R. H. Hance, A. G. Hansen, H. Hara, J. Harder, G. W. Hart, E. P. Hartouni, A. Harvey, L. Hawkins, R. S.

Hayano, H. Hayashi, N. Hayashi, X. He, N. Heine, F. Heistermann, S. Held, T. K. Hemmick, J. M. Heuser, M. Hibino, J. S. Hicks, R. Higuchi, J. C. Hill, T. Hirano, D. S. Ho, R. Hoade, W. Holzmann, K. Homma, B. Hong, A. Hoover, T. Honaguchi, C. T. Hunter, D. E. Hurst, R. Hutter, T. Ichihara, V. V. Ikonnikov, K. Imai, M. Inaba, M. S. Ippolitov, L. Davis Isenhower, L. Donald Isenhower, M. Ishihara, M. Issah, V. I. Ivanov, B. V. Jacak, G. Jackson, J. Jackson, D. Jaffe, U. Jagadish, W. Y. Jang, R. Jayakumar, J. Jia, B. M. Johnson, J. Johnson, S. C. Johnson, J. P. Jones, K. Jones, K. S. Joo, D. Jouan, S. Kahn, F. Kajihara, S. Kametani, N. Kamiyashkov, Y. Kamyshkov, A. Kandasamy, J. H. Kang, M. R. Kann, S. S. Kapoor, J. Kapustinsky, K. V. Karadjev, V. Kashikhin, S. Kato, K. Katou, H. J. Kehayias, M. A. Kelley, S. Kelly, M. Kennedy, B. Khachaturov, A. V. Khanzadeev, A. Khomutnikov, J. Kikuchi, D. J. Kim, D. W. Kim, G. B. Kim, H. J. Kim, S. Y. Kim, Y. G. Kim, W. W. Kinnison, E. Kistenev, A. Kiyomichi, C. Klein-Boesing, S. Klinksiek, L. Kluberg, H. Kobayashi, V. Kochetkov, D. Koehler, T. Kohama, B. G. Komkov, M. L. Kopytine, K. Koseki, L. Kotchenda, D. Kotchetkov, Iou A. Koutcheryaev, A. Kozlov, V. S. Kozlov, P. A. Kravtsov, P. J. Kroon, C. H. Kuberg, L. G. Kudin, M. Kurata-Nishimura, V. V. Kuriatkov, K. Kurita, Y. Kuroki, M. J. Kweon, Y. Kwon, G. S. Kyle, J. J. LaBounty, R. Lace, J. G. Lajoie, J. Lauret, A. Lebedev, V. A. Lebedev, V. D. Lebedev, D. M. Lee, S. Lee, M. J. Leitch, M. Lenz, W. Lenz, X. H. Li, Z. Li, B. Libby, M. Libkind, W. Liccardi, D. J. Lim, S. Lin, M. X. Liu, X. Liu, Y. Liu, Z. Liu, E. Lockner, N. Longbotham, J. D. Lopez, R. Machnowski, C. F. Maguire, J. Mahon, Y. I. Makdisi, V. I. Manko, Y. Mao, S. Marino, S. K. Mark, S. Markacs, D. G. Markushin, G. Martinez, X. B. Martinez, M. D. Marx, A. Masaike, F. Matathias, T. Matsumoto, P. L. McGaughey, M. C. McCain, J. Mead, E. Melnikov, Y. Melnikov, W. Z. Meng, M. Merschmeyer, F. Messer, M. Messer, Y. Miake, N. M. Miftakhov, S. Migluolio, J. Milan, T. E. Miller, A. Milov, K. Minuzzo, S. Mioduszewski, R. E. Mischke, G. C. Mishra, J. T. Mitchell, Y. Miyamoto, A. K. Mohanty, B. C. Montoya, A. Moore, T. Moore, D. P. Morrison, G. G. Moscone, J. M. Moss, F. Mühlbacher, M. Muniruzzaman, J. Murata, M. M. Murray, M. Musrock, S. Nagamiya, Y. Nagasaka, J. L. Nagle, Y. Nakada, T. Nakamura, B. K. Nandi, J. Negrin, J. Newby, L. Nikkinen, S. A. Nikolaev, P. Nilsson, S. Nishimura, A. S. Nyanin, J. Nystrand, E. O'Brien, P. O'Conner, F. Obenshain, C. A. Ogilvie, H. Ohnishi, I. D. Ojha, M. Ono, V. Onuchin, A. Oskarsson, L. Österman, I. Otterlund, K. Oyama, L. Paffrath, A. P T Palounek, C. E. Pancake, V. S. Pantuev, V. Papavassiliou, S. F. Pate, T. Peitzmann, R. Petersen, A. N. Petridis, C. H. Pinkenburg, R. P. Pisani, P. Pitukhin, T. Plagge, F. Plasil, M. Pollack, K. Pope, R. Prigl, M. L. Purschke, A. K. Purwar, J. M. Qualls, S. Rankowitz, G. Rao, R. Rao, M. Rau, I. Ravinovich, R. Raynis, K. F. Read, K. Reygers, G. Riabov, V. G. Riabov, Y. G. Riabov, S. H. Robinson, G. Roche, A. Romana, M. Rosati, E. V. Roschin, A. A. Rose, P. Rosnet, R. Roth, R. Ruggiero, S. S. Ryu, N. Saito, A. Sakaguchi, T. Sakaguchi, S. Sakai, H. Sako, T. Sakuma, S. Salomone, V. M. Samsonov, W. F. Sandhoff, L. Sanfratello, T. C. Sangster, R. Santo, H. D. Sato, S. Sato, R. Savino, S. Sawada, B. R. Schlei, R. Schleuter, Y. Schutz, M. Sekimoto, V. Semenov, R. Seto, Y. Severgin, A. Shajii, V. Shangin, M. R. Shaw, T. K. Shea, I. Shein, V. Shelikhov, T. A. Shibata, K. Shigaki, T. Shiina, T. Shimada, Y. H. Shin, I. G. Sibiriak, D. Silvermyr, K. S. Sim,

- J. Simon-Gillo, M. Simpson, C. P. Singh, V. Singh, W. Sippach, M. Sivertz, H. D. Skank, S. Skutnik, G. A. Sleige, D. C. Smith, G. D. Smith, M. Smith, A. Soldatov, G. P. Solodov, R. A. Soltz, W. E. Sondheim, S. Sorensen, I. Sourikova, F. Staley, P. W. Stankus, N. Starinsky, S. Steffens, E. M. Stein, P. Steinberg, E. Stenlund, M. Stepanov, A. Ster, J. Stewering, W. Stokes, S. P. Stoll, M. Sugioka, T. Sugitate, J. P. Sullivan, Y. Sumi, Z. Sun, M. Suzuki-Nara, E. M. Takagui, A. Taketani, M. Tamai, K. H. Tanaka, Y. Tanaka, E. Taniguchi, M. J. Tannenbaum, V. I. Tarakanov, O. P. Tarasenkova, J. D. Tepe, R. Thern, J. H. Thomas, J. L. Thomas, T. L. Thomas, W. D. Thomas, G. W. Thornton, W. Tian, R. Todd, J. Tojo, F. Toldo, H. Torii, R. S. Towell, J. Tradeski, V. A. Trofimov, I. Tserruya, H. Tsuruoka, A. A. Tsvetkov, S. K. Tuli, G. Turner, H. Tydesjö, N. Tyurin, S. Urasawa, A. Usachev, T. Ushiroda, H. W. van Hecke, M. van Lith, A. A. Vasiliev, V. Vasiliev, M. Vassent, C. Velissaris, J. Velkovska, M. Velkovsky, W. Verhoeven, L. Villatte, A. A. Vinogradov, V. I. Vishnevskii, M. A. Volkov, W. von Achen, A. A. Vorobyov, E. A. Vznuzdaev, M. Vznuzdaev, J. W. Walker, Y. Wan, H. Q. Wang, S. Wang, Y. Watanabe, L. C. Watkins, T. Weimer, S. N. White, B. R. Whitus, C. Williams, P. S. Willis, A. L. Wintenberg, C. Witzig, F. K. Wohn, K. Wolniewicz, B. G. Wong-Swanson, L. Wood, C. L. Woody, L. W. Wright, J. Wu, W. Xie, N. Xu, K. Yagi, R. Yamamoto, Y. Yang, S. Yokkaichi, Y. Yokota, S. Yoneyama, G. R. Young, I. E. Yushmanov, W. A. Zajc, C. Zhang, L. Zhang, Z. Zhang, and S. Zhou. PHENIX detector overview. *Nuclear Instruments and Methods in Physics Research, Section A: Accelerators, Spectrometers, Detectors and Associated Equipment*, 499(2-3):469–479, 2003.
- [29] Abraham Meles. *Measurement of longitudinal spin asymmetry in production of muons from W / Z boson decays in polarized p + p collisions at s = 500 GeV with the PHENIX detector at RHIC*. PhD thesis, 2012.
  - [30] M. Breidenbach, J. I. Friedman, H. W. Kendall, E. D. Bloom, D. H. Coward, H. Destaebler, J. Drees, L. W. Mo, and R. E. Taylor. Observed behavior of highly inelastic electron-proton scattering. *Physical Review Letters*, 23(16):935–939, 1969.
  - [31] J. D. Bjorken and E. A. Paschos. Inelastic electron-proton and  $\gamma$ -proton scattering and the structure of the nucleon. *Physical Review*, 185(5):1975–1982, 1969.
  - [32] Bogdan Povh and Thomas Walcher. The end of the nucleon-spin crisis. 2016.
  - [33] Stanley J. Brodsky, John Ellis, and Marek Karliner. Chiral symmetry and the spin of the proton. *Physics Letters B*, 206(2):309–315, 1988.
  - [34] Thomas Stanley. The History of Philosophy, 1655.
  - [35] Hendrick ter Brugghen. Democritus, 1628.
  - [36] Richard W. Baldes. ‘Divisibility’ and ‘Division’ in Democritus. *Apeiron: A Journal for Ancient Philosophy and Science*, 12(1):1–12, 1978.
  - [37] Konstantinos Alexakos and Wladina Antoine. The Golden Age of Islam and Science Teaching: Teachers and students develop a deeper understanding of the foundations

- of modern science by learning about the contributions of Arab-Islamic scientists and scholars. *The Science Teacher*, 72(3):36–39, 2005.
- [38] Fraser Cowley. *A Critique of British Empiricism*. MacMillan, 1968.
  - [39] Ottavio Leoni. Galileo Galilei, Portrait in Crayon by Leoni, 1624.
  - [40] A. Rupert Hall. Galileo and the Science of Motion. *The British Journal for the History of Science*, 2(3):185–199, 1965.
  - [41] Roger H. Stuewer. A Critical Analysis of Newton’s Work on Diffraction. *Isis*, 61(2):188–205, 1970.
  - [42] Gary Patterson. Jean Perrin and the triumph of the atomic doctrine. *Endeavour*, 31(2):50–53, jun 2007.
  - [43] George Thomson. J. J. Thomson, 1956.
  - [44] Kurzon. Diagram of JJ Thomson’s Experiment With Cathod Rays, 2010.
  - [45] Nobel Media. J.J. Thomson - Biographical, 2014.
  - [46] M Planck. On the law of the energy distribution in the normal spectrum. *Ann. Phys*, 4:1–11, 1901.
  - [47] J. Clerk Maxwell. A Dynamical Theory of the Electromagnetic Field [J]. *Philosophical Transactions of the Royal Society of London*, 155(January):459–512, 1865.
  - [48] P. A. M. Dirac. The Quantum Theory of the Electron. *Proceedings of the Royal Society A: Mathematical, Physical and Engineering Sciences*, 117(778):610, 1928.
  - [49] Nobel Foundation. Paul Dirac, 1933.
  - [50] Frank Krauss. History of Particle Physics. Technical report, Institute for Particle physics Phenomenology, University of Durham, Durham, 2015.
  - [51] W Heisenberg. Production of Mesons as a Shock Wave Problem Visual description of a shock wave. pages 1–17, 1952.
  - [52] H. Yukawa, S. Sakata, and M. Taketani. On the interaction of elementary particles. III. *Progress of Theoretical Physics Supplement*, 1(Received):24–45, 1955.
  - [53] Pj Bryant. A brief history and review of accelerators. *Cern European Organization for* ..., 1994.
  - [54] M. Gell-Mann. Isotopic spin and new unstable particles. *Physical Review*, 92(3):833–834, 1953.
  - [55] M. Gell-Mann. The interpretation of the new particles as displaced charge multiplets. *Il Nuovo Cimento Series 10*, 4(1 Supplement):848–866, 1956.

- [56] Michael Riordan. *The Discovery of Quarks*. 1992.
- [57] GW Bennett, B Bousquet, HN Brown, G Bunce, RM Carey, P Cushman, GT Danby, PT Debevec, M Deile, H Deng, SK Dhawan, VP Druzhinin, L Duong, FJM Farley, GV Fedotovich, Fe Gray, D Grigoriev, M Grosse-Perdekamp, A Grossmann, MF Hare, DW Hertzog, X Huang, VW Hughes, M Iwasaki, K Jungmann, D Kawall, Bi Khazin, F Krienen, I Kronkvist, A Lam, R Larsen, YY Lee, I Logashenko, R McNabb, W Meng, JP Miller, WM Morse, D Nikas, CJG Onderwater, Y Orlov, CS Ozben, JM Paley, Q Peng, CC Polly, J Pretz, R Prigl, G zu Putlitz, T Qian, Si Redin, O Rind, BL Roberts, N Ryskulov, YK Semertzidis, P Shagin, YuM Shatunov, Ep Sichtermann, E Solodov, M Sossong, LR Sulak, A Trofimov, P von Walter, and A Yamamoto. Measurement of the Negative Muon Anomalous Magnetic Moment to 0.7 ppm. 2004.
- [58] Sven Kullander. Highlights of the European muon collaboration. *Nuclear Physics, Section A*, 518(1-2):262–296, nov 1990.
- [59] J. Ashman, B. Badelek, G. Baum, J. Beaufays, C. P. Bee, C. Benchouk, I. G. Bird, S. C. Brown, M. C. Caputo, H. W K Cheung, J. S. Chima, J. Ciborowski, R. Clift, G. Coignet, F. Combley, G. Court, G. D'Agostini, J. Drees, M. Düren, N. Dyce, A. W. Edwards, M. Edwards, T. Ernst, M. I. Ferrero, D. Francis, E. Gabathuler, R. Gamet, V. Gibson, J. Gillies, P. Grafström, K. Hamacher, D. V. Harrach, P. J. Hayman, J. R. Holt, V. W. Hughes, A. Jacholkowska, T. Jones, E. M. Kabuss, B. Korzen, U. Krüner, S. Kullander, U. Landgraf, D. Lanske, F. Lettenström, T. Lindqvist, J. Loken, M. Matthews, Y. Mizuno, K. Mönig, F. Montanet, E. Nagy, J. Nassalski, T. Niinikoski, P. R. Norton, F. G. Oakham, R. F. Oppenheim, A. M. Osborne, V. Papavassiliou, N. Pavel, C. Peroni, H. Peschel, R. Piegaia, B. Pietrzyk, U. Pietrzyk, B. Povh, P. Renton, J. M. Rieubland, A. Rijllart, K. Rith, E. Rondio, L. Ropelewski, D. Salmon, A. Sandacz, T. Schröder, K. P. Schüler, K. Schultze, T. A. Shibata, T. Sloan, A. Staiano, H. E. Stier, J. Stock, G. N. Taylor, J. C. Thompson, T. Walcher, J. Toth, L. Urban, W. Wallucks, S. Wheeler, D. A. Williams, W. S C Williams, S. J. Wimpenny, R. Windmolders, W. J. Womersley, and K. Ziemons. An investigation of the spin structure of the proton in deep inelastic scattering of polarised muons on polarised protons. *Nuclear Physics, Section B*, 328(1):1–35, 1989.
- [60] M Gell-Mann. The eightfold way: A theory of strong interaction symmetry. Technical report, California Institution of Technology, Pasadena, 1961.
- [61] B. Adeva, T. Akdogan, E. Arik, B. Badelek, G. Bardin, G. Baum, P. Berglund, L. Betev, R. Birsa, N. de Botton, F. Bradamante, A. Bravar, A. Bressan, S. Bültmann, E. Burtin, C. Cavata, D. Crabb, J. Cranshaw, T. Çuhadai, S. Dalla Torre, R. van Dantzig, B. Derro, A. Deshpande, S. Dhawan, C. Dulya, S. Eichblatt, D. Fasching, F. Feinstein, C. Fernandez, S. Forthmann, B. Frois, A. Gallas, J. A. Garzon, H. Gilly, M. Giorgi, E. von Goeler, S. Goertz, G. Gracia, N. de Groot, M. Grosse Perdekamp, K. Haft, D. von Harrach, T. Hasegawa, P. Hautle, N. Hayashi, C. A. Heusch, N. Horikawa, V. W. Hughes, G. Igo, S. Ishimoto, T. Iwata, E. M. Kabuß, T. Kageya, A. Karev, H. J. Kessler, T. J. Ketel, J. Kiryluk, Yu. Kisselev, D. Krämer, V. Krivokhijine, W. Kröger, V. Kukhtin, K. Kurek, J. Kyynäräinen, M. Lamanna, U. Landgraf,

- J. M. Le Goff, F. Lehar, A. de Lesquen, J. Lichtenstadt, M. Litmaath, A. Magnon, G. K. Mallot, F. Marie, A. Martin, J. Martino, T. Matsuda, B. Mayes, J. S. McCarthy, K. Medved, W. Meyer, G. van Middelkoop, D. Miller, Y. Miyachi, K. Mori, J. Moromisato, J. Nassalski, L. Naumann, T. O. Niinikoski, J. E. J. Oberski, A. Ogawa, C. Ozben, H. Pereira, F. Perrot-Kunne, D. Peshekhonov, R. Piegaia, L. Pinsky, S. Platchkov, M. Plo, D. Pose, H. Postma, J. Pretz, R. Puntaferro, T. Pussieux, G. Rädel, A. Rijllart, G. Reicherz, J. Roberts, M. Rodriguez, E. Rondio, I. Sabo, J. Saborido, A. Sandacz, I. Savin, P. Schiavon, A. Schiller, E. P. Sichtermann, F. Simeoni, G. I. Smirnov, A. Staude, A. Steinmetz, U. Stiegler, H. Stuhrmann, M. Szleper, F. Tessarotto, D. Thers, W. Tlaczala, A. Tripet, G. Unel, M. Velasco, J. Vogt, R. Voss, C. Whitten, R. Windmolders, R. Willumeit, W. Wislicki, A. Witzmann, J. Ylöstalo, A. M. Zanetti, K. Zaremba, and J. Zhao. Spin asymmetries A1 and structure functions g1 of the proton and the deuteron from polarized high energy muon scattering. *Physical Review D*, 58:17, 1998.
- [62] B. Adeva, T. Akdogan, E. Arik, B. Badelek, G. Bardin, G. Baum, P. Berglund, L. Betev, R. Birsa, N. de Botton, F. Bradamante, A. Bravar, A. Bressan, S. Bültmann, E. Burtin, C. Cavata, D. Crabb, J. Cranshaw, T. Çuhadai, S. Dalla Torre, R. van Dantzig, B. Derro, A. Deshpande, S. Dhawan, C. Dulya, S. Eichblatt, D. Fasching, F. Feinstein, C. Fernandez, S. Forthmann, B. Frois, A. Gallas, J. A. Garzon, H. Gilly, M. Giorgi, E. von Goeler, S. Goertz, G. Gracia, N. de Groot, M. Grosse Perdekamp, K. Haft, D. von Harrach, T. Hasegawa, P. Hautle, N. Hayashi, C. A. Heusch, N. Horikawa, V. W. Hughes, G. Igo, S. Ishimoto, T. Iwata, E. M. Kabuß, T. Kageya, A. Karev, H. J. Kessler, T. J. Ketel, J. Kiryluk, Yu. Kisseelev, D. Krämer, V. Krivokhin, W. Kröger, V. Kukhtin, K. Kurek, J. Kyynäräinen, M. Lamanna, U. Landgraf, J. M. Le Goff, F. Lehar, A. de Lesquen, J. Lichtenstadt, M. Litmaath, A. Magnon, G. K. Mallot, F. Marie, A. Martin, J. Martino, T. Matsuda, B. Mayes, J. S. McCarthy, K. Medved, W. Meyer, G. van Middelkoop, D. Miller, Y. Miyachi, K. Mori, J. Moromisato, J. Nassalski, L. Naumann, T. O. Niinikoski, J. E. J. Oberski, A. Ogawa, C. Ozben, H. Pereira, F. Perrot-Kunne, D. Peshekhonov, R. Piegaia, L. Pinsky, S. Platchkov, M. Plo, D. Pose, H. Postma, J. Pretz, R. Puntaferro, T. Pussieux, G. Rädel, A. Rijllart, G. Reicherz, J. Roberts, M. Rodriguez, E. Rondio, I. Sabo, J. Saborido, A. Sandacz, I. Savin, P. Schiavon, A. Schiller, E. P. Sichtermann, F. Simeoni, G. I. Smirnov, A. Staude, A. Steinmetz, U. Stiegler, H. Stuhrmann, M. Szleper, F. Tessarotto, D. Thers, W. Tlaczala, A. Tripet, G. Unel, M. Velasco, J. Vogt, R. Voss, C. Whitten, R. Windmolders, R. Willumeit, W. Wislicki, A. Witzmann, J. Ylöstalo, A. M. Zanetti, K. Zaremba, and J. Zhao. Next-to-leading order QCD analysis of the spin structure function  $\langle \text{math display="block"> \langle mrow \rangle \langle msub \rangle \langle mrow \rangle \langle mi \rangle g \langle /mi \rangle \langle /mrow \rangle \langle mrow \rangle \langle mn \rangle 1 \langle /mn \rangle \langle /mrow \rangle \langle /msub \rangle \langle /mrow \rangle \langle /math \rangle$ . *Physical Review D*, 58(11):112002, 1998.
- [63] Brookhaven National Laboratory. RHIC Complex, 2011.
- [64] RHIC. RHIC — Accelerator Complex, 2016.
- [65] I. Alekseev, C. Allgower, M. Bai, Y. Batygin, L. Bozano, K. Brown, G. Bunce,

- P. Cameron, E. Courant, S. Erin, J. Escallier, W. Fischer, R. Gupta, K. Hatanaka, H. Huang, K. Imai, M. Ishihara, A. Jain, A. Lehrach, V. Kanavets, T. Katayama, T. Kawaguchi, E. Kelly, K. Kurita, S. Y. Lee, A. Luccio, W. W. MacKay, G. Mahler, Y. Makdisi, F. Mariam, W. McGahern, G. Morgan, J. Muratore, M. Okamura, S. Peggs, F. Pilat, V. Ptitsin, L. Ratner, T. Roser, N. Saito, H. Satoh, Y. Shatunov, H. Spinka, M. Syphers, S. Tepikian, T. Tominaka, N. Tsoupas, D. Underwood, A. Vasiliev, P. Wanderer, E. Willen, H. Wu, A. Yokosawa, and A. N. Zelenski. Polarized proton collider at RHIC. *Nuclear Instruments and Methods in Physics Research, Section A: Accelerators, Spectrometers, Detectors and Associated Equipment*, 499(2-3):392–414, 2003.
- [66] Shoji Nagamiya. PHENIX Experiment at RHIC. *Nuclear Physics A*, 566:287c–298 c, 1994.
- [67] PHENIX Collaboration and N. Saito. Spin Physics with the PHENIX Detector System. *Nuclear Physics A*, 638:575–578, 1998.
- [68] A. Adare, S. Afanasiev, C. Aidala, N. N. Ajitanand, Y. Akiba, R. Akiimoto, J. Alexander, H. Al-Taani, K. R. Andrews, A. Angerami, K. Aoki, N. Apadula, E. Appelt, Y. Aramak, R. Armendariz, E. C. Aschenauer, T. C. Awes, B. Azmoun, V. Babintsev, M. Bai, B. Bannier, K. N. Barish, B. Bassalleck, A. T. Basye, S. Bathe, V. Baublis, C. Baumann, A. Bazilevsky, R. Belmont, R. Bennett, A. Berdnikov, Y. Berdnikov, D. S. Blau, J. S. Bok, K. Boyle, M. L. Brooks, H. Buesching, V. Bumazhnov, G. Bunce, S. Butsyk, S. Campbell, A. Caringi, C. H. Chen, C. Y. Chi, M. Chiu, I. J. Choi, J. B. Choi, R. K. Choudhury, P. Christiansen, T. Chujo, O. Chvala, V. Cianciolo, Z. Citron, B. A. Cole, Z. Conesa del Valle, M. Connors, M. Csanad, T. Cs org, S. Dairaku, A. Datta, G. David, M. K. Dayananda, A. Denisov, A. Deshpande, E. J. Desmond, K. V. Dharmawardane, O. Dietzsch, A. Dion, M. Donadelli, L. D Orazio, O. Drapier, A. Drees, K. A. Drees, J. M. Durham, A. Durum, Y. V. Efremenko, T. Engelmore, A. Enokizono, H. En’yo, S. Esumi, B. Fadem, D. E. Fields, M. Finger, Jr., F. Fleuret, S. L. Fokin, J. E. Frantz, A. Franz, A. D. Frawley, Y. Fukao, T. Fusayasu, I. Garishvili, A. Glenn, M. Gonin, Y. Goto, R. Granier de Cassagnac, N. Grau, S. V. Greene, M. Grosse Perdekamp, T. Gunji, L. Guo, H. . Gustafsson, J. S. Haggerty, K. I. Hahn, H. Hamagaki, J. Hamblen, J. Hanks, R. Han, E. Haslum, R. Hayano, T. K. Hemmick, T. Hester, X. He, J. C. Hill, R. S. Hollis, W. Holzmann, K. Homma, B. Hong, T. Horaguchi, Y. Hori, D. Hornback, S. Huang, T. Ichihara, R. Ichimiya, H. Iinuma, Y. Ikeda, K. Imai, M. Inaba, A. Iordanova, D. Isenhower, M. Ishihara, M. Issah, A. Isupov, D. Ivanischev, Y. Iwanaga, B. V. Jacak, PHENIX: J. Jia, X. Jiang, B. M. Johnson, T. Jones, K. S. Joo, D. Jouan, J. Kamin, S. Kaneti, B. H. Kang, J. H. Kang, J. Kapustinsky, K. Karatsu, M. Kasai, D. Kawall, A. V. Kazantsev, T. Kempel, A. Khanzadeev, K. M. Kijima, B. I. Kim, D. J. Kim, E. J. Kim, J. S. Kim, Y. J. Kim, Y. K. Kim, E. Kinney, . Kiss, E. Kistenev, D. Kleinjan, P. Kline, L. Kochenda, B. Komkov, M. Konno, J. Koster, D. Kotov, A. Kral, G. J. Kunde, K. Kurita, M. Kurosawa, Y. Kwon, G. S. Kyle, R. Lacey, Y. S. Lai, J. G. Lajoie, A. Lebedev, D. M. Lee, J. Lee, K. B. Lee, K. S. Lee, S. R. Lee, M. J. Leitch, M. A. L. Leite, P. Lichtenwalner, S. H. Lim, L. A. Linden Levy, A. Litvinenko, H. Liu, M. X. Liu, X. Li, B. Love, D. Lynch, C. F. Maguire, Y. I. Makdisi, A. Malakhov, V. I. Manko, E. Mannel, Y. Mao,

H. Masui, M. McCumber, P. L. McGaughey, D. McGlinchey, C. McKinney, N. Means, M. Mendoza, B. Meredith, Y. Miake, T. Mibe, A. C. Mignerey, K. Miki, A. Milov, J. T. Mitchell, Y. Miyachi, A. K. Mohanty, H. J. Moon, Y. Morino, A. Morreale, D. P. Morrison, T. V. Moukhanova, T. Murakami, J. Murata, S. Nagamiya, J. L. Nagle, M. Naglis, M. I. Nagy, I. Nakagawa, Y. Nakamiya, K. R. Nakamura, T. Nakamura, K. Nakano, J. Newby, M. Nguyen, M. Nihashi, R. Nouicer, A. S. Nyanin, C. Oakley, E. O'Brien, C. A. Ogilvie, K. Okada, M. Oka, A. Oskarsson, M. Ouchida, K. Ozawa, R. Pak, V. Pantuev, V. Papavassiliou, B. H. Park, I. H. Park, S. K. Park, S. F. Pate, H. Pei, J. C. Peng, H. Pereira, V. Peresedov, D. Yu. Peressounko, R. Petti, C. Pinkenburg, R. P. Pisani, M. Proissl, M. L. Purschke, H. Qu, J. Rak, I. Ravinovich, K. F. Read, K. Reygers, V. Riabov, Y. Riabov, E. Richardson, D. Roach, G. Roche, S. D. Rolnick, M. Rosati, S. S. E. Rosendahl, P. Rukoyatkin, B. Sahluemiller, N. Saito, T. Sakaguchi, V. Samsonov, S. Sano, M. Sarsour, T. Sato, M. Savastio, S. Sawada, K. Sedgwick, R. Seidl, R. Seto, D. Sharma, I. Shein, T. A. Shibata, K. Shigaki, H. H. Shim, M. Shimomura, K. Shoji, P. Shukla, A. Sickles, C. L. Silva, D. Silvermyr, C. Silvestre, K. S. Sim, B. K. Singh, C. P. Singh, V. Singh, M. Slunečka, R. A. Soltz, W. E. Sondheim, S. P. Sorensen, I. V. Sourikova, P. W. Stankus, E. Stenlund, S. P. Stoll, T. Sugitate, A. Sukhanov, J. Sun, J. Sziklai, E. M. Takagui, A. Takahara, A. Taketani, R. Tanabe, Y. Tanaka, S. Taneja, K. Tanida, M. J. Tannenbaum, S. Tarafdar, A. Tarannenko, E. Tennant, H. Themann, D. Thomas, M. Togawa, L. Tomášek, M. Tomášek, H. Torii, R. S. Towell, I. Tserruya, Y. Tsuchimoto, K. Utsunomiya, C. Vale, H. W. van Hecke, E. Vazquez-Zambrano, A. Veicht, J. Velkovska, R. Vértesi, M. Virius, A. Vossen, V. Vrba, E. Vznuzdaev, X. R. Wang, D. Watanabe, K. Watanabe, Y. Watanabe, F. Wei, J. Wessels, S. N. White, D. Winter, C. L. Woody, R. M. Wright, M. Wysocki, Y. L. Yamaguchi, R. Yang, A. Yanovich, J. Ying, S. Yokkaichi, J. S. Yoo, G. R. Young, I. Younus, Z. You, I. E. Yushmanov, W. A. Zajc, A. Zelenski, S. Zhou, and L. Zolin. Cross Section and Parity Violating Spin Asymmetries of  $W^{\pm}/-$  Boson Production in Polarized p+p Collisions at  $\sqrt{s}=500$  GeV. page 6, 2010.

- [69] Kensuke Okada. Observation of W decay in 500 GeV p+p collisions at RHIC. page 4, 2010.
- [70] Mike Beaumier, Ciprian Gal, Minjung Kim, Sanghwa Park, R Seidl, and Inseok Yoon. Run 13 Spin Database Quality Assurance. Technical report, 2014.
- [71] Michael Collins. The Naive Bayes Model, Maximum-Likelihood Estimation, and the EM Algorithm. pages 1–21, 2013.

## .1 First Thingie

## .2 Second Thingie